SLOPE STABILITY ANALYSES OF ROCK SLOPES AND A COMPARISON OF LIMIT EQUILIBRIUM AND CONTINUUM NUMERICAL METHODS

By

Clarice Romer

210532994

A dissertation submitted in fulfilment of the academic

requirements for the degree of Master of Science in the

Discipline of Geological Sciences

in the School of Agricultural, Earth and Environmental Sciences,

College of Agriculture, Engineering and Science

University of KwaZulu-Natal

Durban, South Africa

2016

As the candidate's supervisor I have/have not approved this thesis/dissertation for submission.

Signed: _____ Name: _____ Date: _____

Abstract

Open pit mines are amongst the world's largest geotechnical structures accounting for a large proportion of the world's metals and minerals. The pressure of future supply of these resources meeting the demands of a growing population leads the mining industry into precarious environments in attempts to access deeper set resources. Increasing depths associated with surface mining operations directly relate to slope angles where steeper slopes are economically appealing due to a reduction in waste rock removal, but at the expense of an increasing risk of slope failure. Rock slope instability in such environments represents a significant hazard and is the cause of serious injuries and fatalities as well as major financial losses. It is therefore essential to rigorously manage this hazard through regular rock slope stability analyses.

There are numerous types of slope stability methods of analysis, all of which aim to safely uphold natural or anthropogenic structures. The Limit Equilibrium Method is particularly useful in hard rock masses with distinctive discontinuities. It allows for the prediction of stable or unstable conditions by calculating the stresses acting on a block and subsequently comparing them to the shear resistance provided by the discontinuity separating the block from the rock mass. This method however requires the user to define a potential failure surface in advance thus indicating its usefulness to a limited range of failure modes. Open pit mines are however dynamic environments which give rise to more complicated responses by the rock mass. The availability of computers and the continued advancements made in computational power has encouraged the development of sophisticated computer codes which are capable of modelling increasingly complex problems. More complex rock slope movements can be determined by numerical modelling techniques such as the Finite Element Method and Finite Difference Method. These methods can analyse the stability of slopes directly through the use of the Shear Strength Reduction technique where strength properties are reduced until failure takes place.

This study explores the aforementioned techniques applied to three critical profiles (A, B, C) selected based on areas of known concern in an open pit mine. Structurally controlled (i.e. planar, wedge, toppling) and non-structurally controlled (i.e. circular) failure mechanisms were assessed via LEMs and compared with numerical models represented as pseudo-discontinuum media. Pseudo-discontinuum media were based on a range of joint network models incorporating kinematically feasible joints which vary in terms of orientation, length, spacing and persistence. These included the Parallel Deterministic network of infinite length and of finite length, the Ubiquitous Joint network model and the Veneziano Joint network model. The geotechnical model was based on data obtained from four different consultants over a period of 15 years which spans

conceptual to design levels. Materials were modelled based on the Generalized Hoek-Brown and Equivalent Mohr-Coulomb failure criteria and results were reported in terms of safety factors, probability of failure and shear strain.

Rock masses represented as continuum media in non-structurally controlled Limit Equilibrium Methods and numerical methods determined stable conditions with good agreement in safety factors between all methods and both strength criteria as well as shear strain accumulation zones between the numerical models. Structurally controlled Limit Equilibrium Method results revealed that profile AA' is the most critical slope with a significant probability of planar and wedge failure at stack angle level. Safety factors for large scale planar failure of profile BB', although stable, remains below the acceptance criteria for the overall slope angle. Profile CC' produced acceptable safety factors and was deemed stable. These results correlated with that of the Ubiquitous Joint network model in the Finite Difference Method and the Parallel Deterministic network of infinite length in the Finite Element Method. Shear strain accumulation of predicted failure modes is however better modelled by the former. The introduction of rock bridges along discontinuity planes in the Parallel Deterministic network of finite and Veneziano Joint network model significantly contributed to stability, reaching minimum safety factors of 3.77 and depicting approximately circular failure surfaces.

A rockfall analysis showed the significance of fall body shape on rockfall trajectories along topographies experiencing crest loss to varying degrees. The three-dimensional analysis revealed that good slope/cut slope topography performs well in terms of catching falling bodies at upper benches as opposed to the moderate and poor slope/cut slope topography which permits movement to the bottom of the slope. The two-dimensional analysis however overestimated results where a minimum of 80% of falling rocks reached the pit floor. Approximately angular shaped rocks achieved greatest velocities in the three-dimensional analysis as opposed to the circular bodies doing so in the two-dimensional analysis.

Preface

The research contained in this dissertation was completed by the candidate while based in the Discipline of Geological Sciences, School of Agricultural, Earth and Environmental Sciences of the College of Agriculture, Engineering and Science, University of KwaZulu-Natal, Westville, South Africa. The research was financially supported by the Council for Geoscience.

The contents of this work have not been submitted in any form to another university and, except where the work of others is acknowledged in the text, the results reported are due to investigations by the candidate.

Acknowledgements

I would firstly like to thank my supervisor, Dr Maria Ferentinou for the knowledge you have imparted on me, for your support and advice, for the time and effort you have given me and for guiding me towards the right path. Thanks must also go the Civil Engineering Department of the University of KwaZulu-Natal for allowing me to use FLAC ®. I would like to acknowledge the Council for Geoscience for their financial assistance towards this research. Special thanks must go to my incredible family and friends for your continued support and encouragement and unwavering love. I am truly blessed to be surrounded by such an amazing group of people every day.

Plagiarism declaration

I, _____ declare that:

i. the research reported in this dissertation, except where otherwise indicated or acknowledged, is my original work;

ii. this dissertation has not been submitted in full or in part for any degree or examination to any other university;

iii. this dissertation does not contain other persons' data, pictures, graphs or other information, unless specifically acknowledged as being sourced from other persons;

iv. this dissertation does not contain other persons' writing, unless specifically acknowledged as being sourced from other researchers. Where other written sources have been quoted, then:

   a) their words have been re-written but the general information attributed to them has been referenced;

   b) where their exact words have been used, their writing has been placed inside quotation marks, and referenced;

v. where I have used material for which publications followed, I have indicated in detail my role in the work;

vi. this dissertation is primarily a collection of material, prepared by myself, published as journal articles or presented as a poster and oral presentations at conferences. In some cases, additional material has been included;

vii. this dissertation does not contain text, graphics or tables copied and pasted from the Internet, unless specifically acknowledged, and the source being detailed in the dissertation and in the references sections.

_____

Signed: Clarice Romer

Date: 02 December 2016

List of symbols and abbreviations

σ = stress

σ_1 = major principal stress

σ_3 = minor principal stress

σ_1' = major principal effective stress

σ_3' = minor principal effective stress

σ_z = out of plane principal stress

σ_n = normal stress

τ = shear stress

ρ = density

γ = unit weight

g = gravitational acceleration

H = slope height

f = trial safety factor

f_o = empirical correction factor

E_m = Young's modulus/ elastic modulus

ν = Poisson's ratio

ε = strain

ε_1 = axial strain

ε_1 = transverse strain

σ_y = yield point

σ_{ci} = uniaxial compressive strength of intact rock

σ_c = uniaxial compressive strength

σ_t = tensile strength

σ_s = shear strength

c = cohesion of intact rock or rock mass

ϕ = friction angle of intact rock or rock mass

c' = effective cohesion of intact rock or rock mass

ϕ' = effective friction angle of intact rock or rock mass

ϕ_{peak} = peak friction angle

ϕ_{res} = residual friction angle

ϕ_i = instantaneous friction angle

ϕ_{joint} = joint friction angle

c_{joint} = joint cohesion

ϕ_b = basic friction angle

ψ_p = failure plane

ψ_f = slope face

ψ_{int} = line of intersection

α_{int} = plunge of line of intersection

α_f = dip direction of slope face

ψ = dilation angle of intact rock or rock mass

A_i = area of slice (method of slices)

S_i = shear resistance (method of slices)

c_i = cohesion of slice i (method of slices)

ϕ_i = basic friction angle of slice i (method of slices)

ψ_i = base inclination of slice i (method of slices)

E_i = force acting on slice i (method of slices)

h_i = height of slice i (method of slices)

m = material constant in the Hoek-Brown failure criterion

m_b = material constant in the Hoek-Brown failure criterion (= m)

m_i = material constant in the Hoek-Brown failure criterion, for intact rock

s = material constant in the Hoek-Brown failure criterion

a = material constant in the modified Hoek-Brown failure criterion

D = disturbance factor

β = Reliability index

R_n = normal coefficient of restitution

R_t = tangential coefficient of restitution

E = Kinetic energy

h = bounce height

V = velocity

COR = coefficient of restitution (3D rockfall analysis)

FoS = Factor of Safety

PoF = Probability of Failure

JRC = Joint Roughness Coefficient

JCS = Joint wall Compressive Strength

RQD = Rock Quality Designation

RMR = Rock Mass Rating

GSI = Geological Strength Index

GH-B = Generalized Hoek-Brown

EM-C = Equivalent Mohr-Coulomb

FEM = Finite Element Method

FDM = Finite Difference Method

SSR = Shear Strength Reduction

SRF = Strength Reduction Factor

FLAC = Fast Lagrangian Analysis of Continua

Contents Page

Page

Abstract i

Preface iii

Acknowledgements iv

Plagiarism declaration v

List of symbols and abbreviations vi

List of Tables i

List of Figures iii

CHAPTER 1 INTRODUCTION 1

1.1. Problem definition 1

1.2. Research objectives 2

CHAPTER 2 LITERATURE REVIEW 3

2.1. Open pit mining and slope stability 3

2.2. Geomechanical behaviour of rock masses and intact rock 7

2.3. Rock mass classifications 9

2.3.1. Rock Quality Designation (RQD) 9

2.3.2. Rock Mass Rating (RMR) 10

2.3.3. Geological Strength Index (GSI) 10

2.4. Rock mass failure criteria for jointed rock masses 11

2.4.1. Hoek-Brown failure criterion 11

2.4.2. Mohr-Coulomb failure criterion 13

2.5. Discontinuities 15

2.5.1. Discontinuities and slope stability 15

2.5.2. Joint network models 16

2.5.3. Non-structurally controlled failure modes 19

2.5.4. Structurally controlled failure modes 20

2.6. Slope stability analysis 23

2.6.1. Limit Equilibrium Methods 24

2.6.2. Numerical modelling 26

2.7. Rockfall hazard assessment 28

CHAPTER THREE METHODOLOGY 31

3.1. Overview 31

3.2. Rock mass properties 32

3.2.1. Overview of regional geology 32
3.2.2. Strength properties of intact rock 35
3.2.3. Shear strength of discontinuities 40
3.2.4. Joint network models 43
3.3. Kinematic analysis 44
3.4. Limit equilibrium analysis 47
3.4.1. Deterministic analysis 47
3.4.2. Probabilistic analysis 49
3.5. Numerical modelling 50
3.5.1. Finite Element Method 50
3.5.2. Finite Difference Method 51
3.6. Rockfall hazard analysis 53
CHAPTER FOUR RESULTS 57
4.1. Kinematic analysis 57
4.2. Limit equilibrium analysis 58
4.3. Numerical modelling 61
4.3.1. Continuum media 61
4.3.2. Pseudo-discontinuum media 67
4.4. Rockfall hazard assessment 77
CHAPTER 5 DISCUSSION 85
5.1. Continuum media 85
5.1.1. Stress controlled Limit Equilibrium Methods (LEM) 85
5.1.2. Numerical models 87
5.2. Pseudo-Discontinuum media 90
5.3. Rockfall hazard analysis 95
CHAPTER 6 CONCLUSION 97
References 99
APPENDIX A 112
APPENDIX B 116

List of Tables

Table 2.1. Typical FoS and PoF acceptance criteria values (Read and Stacey, 2009).... 5

Table 2.2. Correlation between RQD and rock mass quality (Deere, 1968)..... 10

Table 2.3. Characteristics of equilibrium methods of slope stability analysis (after Duncan and Wright, 1980). 25

Table 2.4. Comparison of numerical and limit equilibrium analysis methods (Wyllie and Mah, 2004) 28

Table 3.1. Typical properties of varying rock mass quality (Hoek & Brown, 1997).... 36

Table 3.2. Rock Mass Rating (RMR) and Geological Strength Index (GSI) values (Consultant B, 2006)..... 37

Table 3.3. Rock mass strength properties..... 39

Table 3.4. Joint network properties employed in Phase2 45

Table 3.5. Discontinuity set measurements for critical sections 46

Table 3.6. Deterministic and probabilistic input parameters..... 49

Table 3.7. Mean discontinuity sets employed in the estimation of block size in rockfall analyses..... 55

Table 3.8. Parameters used in 2D and 3D rockfall simulation codes 56

Table 3.9. 2D and 3D shapes employed in rockfall simulation..... 56

Table 4.1. Deterministic and probabilistic LEM results for Profile A 60

Table 4.2. Deterministic and probabilistic LEM results for Profile B..... 61

Table 4.3. Safety factors determined using Slide with both Generalized Hoek-Brown and equivalent Mohr-Coulomb strength parameters 61

Table 4.4. Results for the FEM and FDM for continuum profiles using the Generalized Hoek-Brown and equivalent Mohr-Coulomb strength criteria..... 67

Table 4.5. Safety factors obtained for pseudo-discontinuum media using the FEM and FDM..... 79

Table 4.6. Total percentage or rocks collected at each bench. 80

Table 4.7. Results of 2D rockfall trajectories along good, moderate and poor slope/cut slope topography..... 80

Table 4.8. Comparison of Trajec3D rockfall trajectories along good, moderate and poor slope/cut slope topography 82

Table 4.9. 3D analysis findings of falling block shapes which passed the first berm ×, and ◊ represents falling blocks which travelled to the bottom of the pit..... 84

Table 5.1. FoS determined using stress controlled Limit Equilibrium Methods..... 86
Table 5.2. Safety factors obtained for continuum media using the FEM and FDM..... 88

List of Figures

Figure 2.1. Pit slope geometry depicting key components of slope design (Wyllie and Mah, 2004) 4

Figure 2.2. Potential economic impact of slope steepening (modified from Read and Stacey, 2009) 5

Figure 2.3. Stress-strain curves depicting a) types of elasticity, b) perfectly plastic, c) elastic-plastic, and d) elastic-plastic with strain hardening, softening and elastic-perfect-plastic behaviour of isotropic materials (modified from Jaeger and Cook, 1979) 9

Figure 2.4. Mohr diagram and failure envelopes (Labuz and Zang, 2012) 14

Figure 2.5. Typical profiles associated with JRC values for 200 mm and 1000 mm sample sizes (Barton, 1987) 16

Figure 2.6. 2D Ubiquitous Joint model (modified from Sjoberg, 1999) 18

Figure 2.7. Parallel Deterministic joint network with a) joints of infinite length and b) non-persistent joints (modified from Rocscience Inc., 2016). ..... **Error! Bookmark not defined.**

Figure 2.8. Generation of the Veneziano joint system model a) 2D Poisson line process, b) marking of polygonal joints, c) 3D Poisson plane process, and d) 2D Veneziano model (Dershowitz and Einstein, 1988) 19

Figure 2.9. Development of curvilinear slips for a) isotropic material, b) anisotropic material, c) major structural feature, d) low cohesion, granular material, and e) inhomogeneous material (modified from Hoek and Bray, 1981) ... **Error! Bookmark not defined.**

Figure 2.10. Circular failure mechanism (modified from Hoek and Bray, 1981) 20

Figure 2.11. Planar failure mechanism a) plane failure in cross section b) release surfaces at ends of plane failure and c) kinematic feasibility (modified from Hoek and Bray, 1981) 21

Figure 2.12. Wedge failure a) geometric conditions, b) line of intersection, c) kinematics of wedge failure along a line of intersection and d) wedge failure along discontinuity plane A (modified from Hoek and Bray, 1981) 22

Figure 2.13. Common types of toppling failures including a) block toppling, b) flexural toppling and c) block-flexure toppling (Goodman and Bray 1976) 23

Figure 2.14. Forces acting on a slice (modified from Hoek and Bray, 1981)…….26

Figure 3.1. Overview of study methodology 33

Figure 3.2. Pit configuration and measurement zones from consultants with critical profiles' locations..... 34

Figure 3.3. Geological map of the Zimbabwe Craton (modified from Tieblemont, 2016) 35

Figure 3.4. Geological Strength Index values characterizing blocky rock masses on the basis of particle interlocking and discontinuity condition (Hoek and Marinos, 2000)..... 38

Figure 3.5. Principal stress and shear-normal failure envelopes for metagabbro, tonalite and dolerite..... 40

Figure 3.6. Micro- and macro-scale roughness of discontinuities..... 41

Figure 3.7. Discontinuity infilling material for profiles A, B and C 42

Figure 3.8. Discontinuity persistence of critical mean discontinuity sets for a) Profile A, b) Profile B and c) Profile C. 42

Figure 3.9. Persistent and most influential discontinuities present throughout the pit. 48

Figure 3.10. Current pit slope configuration. 49

Figure 3.11. Tools and stages employed in creating and running a FLAC model 53

Figure 3.12. Slope profiles depicting a) theoretical design profile, b) realistic profile simulating a good slope/cut slope topography, c) realistic profile simulating a moderate slope/cut slope topography and d) realistic profile simulating a poor slope/cut slope topography. 54

Figure 4.1. Kinematic analysis for thee critical profiles along overall slope angle and stack angle levels 59

Figure 4.2. Profile A FEM results showing a) Maximum shear strain contours with Slide failure surfaces included, and b) Plasticity indicators, and FDM results showing c) maximum shear strain contours and d) Plasticity indicators, using the Generalized Hoek-Brown criterion 63

Figure 4.3. Profile B FEM results showing a) Maximum shear strain contours with Slide failure surfaces included, and b) Plasticity indicators, and FDM results showing c) maximum shear strain contours and d) Plasticity indicators, using the Generalized Hoek-Brown criterion 64

Figure 4.4. Profile C FEM results showing a) Maximum shear strain contours with Slide failure surfaces included, and b) Plasticity indicators, and FDM results showing c) maximum shear strain contours and d) Plasticity indicators, using the Generalized Hoek-Brown criterion 65

Figure 4.5. Profile A FEM results showing a) Maximum shear strain contours with Slide failure surfaces incorporated, and b) Plasticity indicators, and FDM results

showing c) maximum shear strain contours and d) Plasticity indicators, using the equivalent Mohr-Coulomb strength parameters..... 66

Figure 4.6. Profile B FEM results showing a) Maximum shear strain contours which Slide failure surfaces incorporated, and b) Plasticity indicators, and FDM results showing c) maximum shear strain contours and d) Plasticity indicators, using equivalent Mohr-Coulomb strength parameters..... 68

Figure 4.7. Profile C FEM results showing a) Maximum shear strain contours with Slide failure surfaces incorporated, and b) Plasticity indicators, and FDM results showing c) maximum shear strain contours and d) Plasticity indicators, using equivalent Mohr-Coulomb strength parameters 69

Figure 4.8. Results of the FDM with the Ubiquitous Joint network model for profile A with a) an inclination of 57° (J1), and its associated b) plasticity indicators and, c) an inclination of 81° (J3) and its associated d) plasticity indicators 71

Figure 4.9. Results of the FDM with the Ubiquitous Joint network model for profile B with a) an inclination of 56° (J1), and its associated b) plasticity indicators and c) an inclination of 44° (J2) and its associated d) plasticity indicators. 72

Figure 4.10. Results of the FDM with the Ubiquitous Joint network model for profile C with a) an inclination of 53° (J1), and its associated b) plasticity indicators and c) an inclination of 87° (J2) and its associated d) plasticity indicators. 73

Figure 4.11. Maximum shear strain associated with the Parallel Deterministic joint network of infinite length showing a) profile A with joint set 1 b) profile A with joint set 3, c) profile A with combined joint sets 1 and 3, d) profile B with joint set 1 e) profile B with joint set 2, f) profile B with combined joint sets 1 and 2, g) profile C with joint set 1 h) profile C with joint set 2 and i) profile C with combined joint sets 1 and 2. 76

Figure 4.12. Maximum shear strain associated with the Parallel Deterministic joint network of finite length showing a) profile A with joint set 1 b) profile A with joint set 3, c) profile A with combined joint sets 1 and 3, d) profile B with joint set 1 e) profile B with joint set 2, f) profile B with combined joint sets 1 and 2, g) profile C with joint set 1 h) profile C with joint set 2 and i) profile C with combined joint sets 1 and 2. 77

Figure 4.13. Maximum shear strain associated with the Veneziano joint network for a) profile A with joint set 1 b) profile A with joint set 3, c) profile A with combined joint sets 1 and 3, d) profile B with joint set 1 e) profile B with joint set 2, f) profile B with combined joint sets 1 and 2, g) profile C with

joint set 1 h) profile C with joint set 2 and i) profile C with combined joint sets 1 and 2 78

Figure 4.14. 2D rockfall trajectories along slopes simulating a) good slope/cut slope topography, b) moderate slope/cut slope topography and c) poor slope/cut slope topography 79

Figure 4.15. 2D results of poor slope/cut slope topography showing the a) total kinetic energy, b) translational velocity and c) bounce heights 81

Figure 4.16. Rockfall trajectories along slopes depicting a) good slope/cut slope topography, b) moderate slope/cut slope topography and c) poor slope/cut slope topography 82

Figure 4.17. Trajec3D energy results for a) good slope/cut slope topography with path 1, b) moderate slope/cut slope topography with path 6 and c) poor slope/cut slope topography with path 4 83

Figure 4.18. Trajec3D velocity results for a) good slope/cut slope topography with path 1, b) moderate slope/cut slope topography with path 6 and c) poor slope/cut slope topography with path 4 83

Figure 5.1. Stress controlled LEM sliding planes for profiles a) A, b) B, and c) C 87

Figure 5.2. FEM and FDM FoS variation from LEM for continuum media 89

Figure 5.3. Safety factors produced for pseudo-discontinuum media using various joint networks ..... **Error! Bookmark not defined.**

CHAPTER 1
INTRODUCTION

1.1. Problem definition

Vast quantities of metals and minerals are mined from surface excavations. The increasing demand for these resources has recently led to the expansion from surface to underground mining operations in attempt to access deeper set resources (Eberhardt and Woo, 2015). With mining operations, slope angles are governed by the close relationship between waste rock removal and slope stability, where steeper slopes are economically appealing due to a reduction in waste rock removal but at the expense of an increased risk of slope failure (Sjöberg, 1999). Due to efficient surface production techniques with mining machinery development and improvement, open pit mines worldwide would merely expand in depth and surface area. Consequently, it is essential to rigorously manage the hazard associated with rock slope stability to prevent serious injuries or fatalities to personnel and damage to infrastructure and machinery and to ultimately ensure the furtherance of the mine.

According to Read and Stacey (2009) potential failure mechanisms are contingent on rock mass strength where structure is likely to be the primary control in stronger rocks and strength, in weaker rocks. A rock mass can therefore fail in three different ways, the first being a structurally controlled failure in which failure is steered by prevailing discontinuities. Failure can also occur with limited structural control which takes place through the rock mass and is associated with highly fractured or weak rock masses. Lastly, an intermediate situation can arise in which failure can be partially controlled by existing structures where failure occurs both through the rock mass and along discontinuities.

The various slope stability analysis methods have their advantages and limitations and their understanding is important in selecting appropriate methods. Limit Equilibrium Methods require assumptions to be made, but if made with understanding and judgement, they can be very accurate (Duncan, 1996). Continuum numerical modelling methods such as the Finite Element Method and Finite Difference Method in conjunction with the Shear Strength Reduction technique, can compute stresses and displacements and can simulate complex conditions, but requires greater time, effort and finance (Duncan, 1996).

Rockfall hazards represent another form of slope instability and are an additional threat in surface mines which can occur more frequently. While rockfalls are sometimes considered a minor problem in comparison to large scale slope instabilities involving benches or sometimes even overall pit slopes, costs rise when maintenance and remedial measures are required. In recent

years, rockfall has been widely studied in the context of surface mining. Rockfall simulators can be employed to assess the danger of an exclusively detached rock by analysing its trajectory based on changes in velocity (Stead et al., 2001).

1.2. Research objectives

The objectives of this study are:

- To construct a geotechnical model based on four data sources devised from conceptual, preliminary feasibility and feasibility studies.
- To assess the effectiveness of using equivalent Mohr-Coulomb parameters based on a range of minor principal stress values.
- To determine key failure mechanisms via numerical modelling Shear Strength Reduction techniques and compare results to stress controlled and structurally controlled Limit Equilibrium Methods.
- To investigate the effect of rock bridges on rock slope stability through the incorporation of non-persistent joint networks in numerical models.
- To conduct rockfall analyses in two and three dimensions and compare results.

CHAPTER 2
LITERATURE REVIEW

2.1. Open pit mining and slope stability

Open pit mining is the process whereby ore is extracted from the surface of the ground and continues downwards thereby creating pit slopes (Sjöberg, 1996). During this process, a progressively deeper pit is cut until operations end (Hochbaum and Chen, 2015). These structures account for a large portion of the world's mineral production (Wyllie and Mah, 2004). With the widening scope of mineral applications, their demand is driven by an ever-growing population (Lusty and Gunn, 2015). The United Nations (2015) projected a global population increase of more than 1 billion within the next 15 years, an increase from approximately 7.3 billion in the year 2015 to 8.5 billion. The imminent future thus carries the mineral industry into even more precarious environments in order to accommodate this demand (Lusty and Gunn, 2015). The world's deepest operating open pit mines, in descending order, include the Bingham Canyon mine in the United States and the Chuquicamata and Escondida mines in Chile which today reach depths of 1.2 km, 850 m, 645 m respectively (Goudie and Viles, 2016). With increasing depth comes increasing risk of slope failure and it is therefore essential to rigorously manage the hazard associated with rock slope stability. Fortunately, the advancement and increased utilization of computational tools now allow mine personnel to make improved informed decisions (Hochbaum and Chen, 2015). With increasing depths and associated stresses, Stacey et al. (2003) have emphasized the importance of numerical stress analysis methods and Hoek et al. (1999) promotes the undertaking of numerical modelling, particularly for more complex slopes where limit equilibrium analyses are often too simplistic.

The fundamental aim of slope stability analyses is to contribute to the safe and economic design of slopes (Abramson et al., 2002). Such analyses can be carried out by firstly examining the stability conditions via limiting equilibrium conditions or the downslope movement of rock mass or secondly, through motion equations in which the path and energy of an unstable falling body are determined (Giani, 1992). Slope stability analyses, particularly in open pit mines, was a popular research theme in the 1960's and 1970's, most of which focussed on limit equilibrium methods. This period however also marked to onset of the early development of numerical methods of analyses (Stacey et al., 2003). Probabilistic slope stability analysis is another essential component as it can be employed in the quantification of uncertainty (El-Ramly et al., 2002).

Slope design is one the most crucial and challenging tasks in open pit mining. The design is based on optimal slope configuration in terms of both safety and financial gain (Read and Stacey, 2009). Pit slope design comprise of three key components including the overall, inter-ramp and bench angles (Wyllie and Mah, 2004). The overall slope refers to the inclination produced from the crest of the uppermost bench to the toe of the lowermost bench (Figure 2.1). The inter-ramp angle however represents the slope forming a set of benches whereas the bench face angle is the angle of an individual bench (Figure 2.1). Hoek et al. (2001) differentiate between structurally and non-structurally controlled slope designs where the former deals with kinematically possible failures which can be analysed via limit equilibrium methods and are typically associated with bench or inter-ramp slopes. The non-structurally controlled failure category, however, can be employed to assess the stability of overall slope angles where failure surfaces pass through a rock mass which has been weakened through the existence of discontinuities.

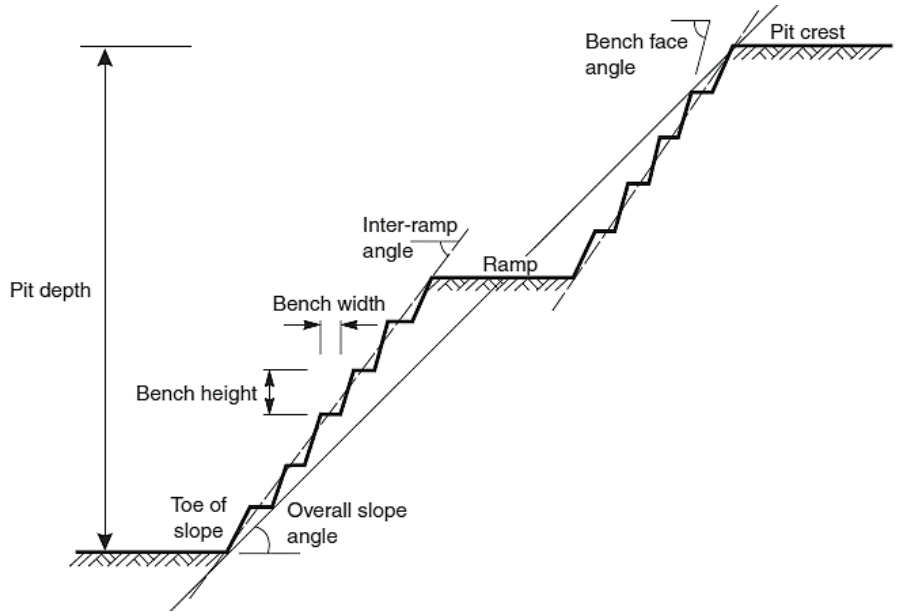

Figure 2.1. Pit slope geometry depicting key components of slope design (Wyllie and Mah, 2004).

Slope failures in mining environments must be manageable from bench to overall pit slope scales in order to safeguard personnel, equipment and the continued mining operation. Together with ensuring safety, Read and Stacey (2009) also highlight the need for slopes to be steep enough to warrant maximum ore recovery with minimum waste stripping (Figure 2.2).

Mines are required to develop acceptability criteria to be used as a standard value in quantifying the performance of slopes (Hoek et al., 2001). The performance can be described in terms of the factor of safety (FoS) or probability of failure (PoF). The FoS refers to the ratio of the ultimate shear strength and the mobilized shear stress at incipient failure (Cheng and Lau, 2008) whereas

the PoF pertains to the probability of the FoS being one or less (Read and Stacey, 2009). The importance of the slope in question gives an indication of the level of acceptance where critical slopes with vital facilities such as ramps, are designed based on a higher FoS and lower PoF (Read and Stacey, 2009). Typical acceptance criteria according to various slope elements are shown in Table 2.1.

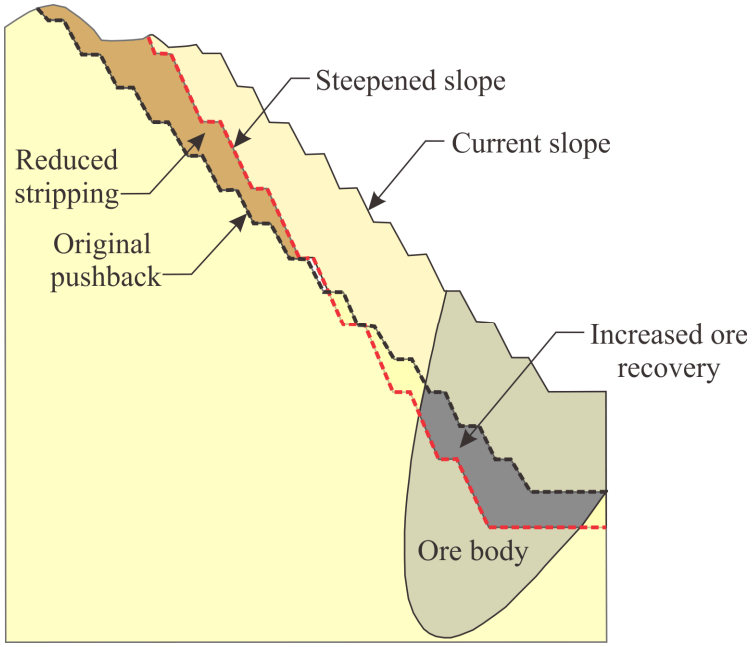

Figure 2.2. Potential economic impact of slope steepening (modified from Read and Stacey, 2009).

Table 2.1. Typical FoS and PoF acceptance criteria values (Read and Stacey, 2009).

		Acceptance criteria[a]		
Slope scale	Consequences of failure	FoS (min) (static)	FoS (min) (dynamic)	PoF (max) P[FoS ≤ 1]
Bench	Low - high[b]	1.1	NA	25 – 50 %
Inter-ramp	Low	1.15 - 1.2	1.0	25 %
	Moderate	1.2	1.0	20 %
	High	1.2 - 1.3	1.1	10 %
Overall	Low	1.2 - 1.3	1.0	15 – 20 %
	Moderate	1.3	1.05	10 %
	High	1.3 - 1.5	1.1	5 %

a: Needs to meet all acceptance criteria;
b: Semi-quantitatively evaluated; b: Semi-qualitatively evaluated

The consequences of slope failure could be social, economic or environmental in nature (Read and Stacey, 2009). Social factors refer to injury or loss of life, income and confidence of

personnel. Economic factors however relate to the loss of money due to the discontinuance of mining operations, loss of ore and equipment, increased stripping as well as costs associated with the removal of unwanted material. Environmental factors apply to the environmental impact associated with slope failure along with the need of improved regulations or ultimately, mine closure considerations (Read and Stacey, 2009).

Slope designs are based on the geotechnical model which is constructed from geological, structural, rock mass and hydrogeological models (Read and Stacey, 2009). The importance of a comprehensive geological model is stressed by Hoek et al. (2001) who warns that without it, questionable designs may arise due to generalized and simplistic analyses. The development of this model requires an excellent understanding of the geological processes which formed the site (Fookes, 1997). The structural model incorporates major structures such as faults and shear zones and second-order structures such as joints and rock fabric (Hoek et al., 2001). According to Read and Stacey (2009), major structures are generally more continuous and are thus expected to have a major impact on inter-ramp or overall slope scales as opposed to the continuity of second-order structures which are more restricted yet closely spaced and thus must be considered in smaller scale design elements such as individual benches or bench stacks. Hoek et al. (2001) make mention of the difficulty in data collection of second-order structures in high rock slopes, in terms of how much data should be collected and how it will be employed in slope designs, which thus declares the convenience of computerised codes in the interpretation of large quantities of data. The rock mass model refers to the properties associated with the material types which are to be excavated. According to Read and Stacey (2009) these properties give a good indication of the likely behaviour of the material with mining operations where slope design is controlled by structure in strong rock of medium height, but by rock mass strength in weaker materials of very high slopes. The hydrogeological model relates to the surface and subsurface water regimes where a build-up of water pressure in discontinuities cause a reduction in effective stresses and a subsequent reduction in shear strength, thus affecting the stability of slopes (Hudson and Harrison, 1997).

The reliability of data associated with the geotechnical model is essential and should be defined. Hoek (1999) stated that data collected pertaining to this model, regardless of the amount, is unreliable to some degree due to the uncertainty related to the methods of allocating numbers to geology and that these numbers are merely usable estimates. Read and Stacey (2009) also mentioned a reduction in reliability due to the limited availability of data during initial stages of a project. Hacking (1975) differentiated between two types of uncertainties, these being aleatory and epistemic uncertainty. Aleatory uncertainty refers to the natural variability in the environment

due to random processes occurring across space and time. A parameter linked to the rock mass is an example of aleatory uncertainty. In contrast, epistemic uncertainty pertains to the lack of data, or having a limited understanding of events and processes. Additional data associated with the latter could mean a decrease in this this form of uncertainty and thus an improved understanding of aleatory uncertainties of data (Fillion and Hadjigeorgiou, 2015). Read and Stacey (2009) separate uncertainties into geological, parameter and model uncertainty. Geological uncertainty includes aspects regarding the unpredictability inherent in the identification of, geometry of, and relationships between, the different lithologies and structures making up the geological model. Examples of such uncertainties include erroneously defining lithological boundaries and faults. Parameter uncertainty however refers to the unpredictability of the parameters employed in the geotechnical model, including values associated with the description of the rock mass. One component of this description includes the use of rock mass classification systems in rock slope engineering which remains a current practice, but could increase uncertainty if used incorrectly. The development of most such systems was based on confined underground conditions thus implying potentially questionable outcomes if not adjusted to suit surface conditions (Hoek et al., 2001). Lastly, model uncertainty relates to the unpredictability associated with the choice of the analysis in preparing the slope design and estimating the reliability of pit walls, and includes methods such as limit equilibrium and numerical analyses (Read and Stacey, 2009).

2.2. Geomechanical behaviour of rock masses and intact rock

Stability concerns may stem from the behaviour of intact rock alone or from the presence of one or more discontinuities. Jointed rock mass strength hinges on the properties of its intact fragments and their capacity to shift under imposed stresses, which is in turn controlled by their shape and interface conditions (Brady and Brown, 2005). In order to analyse the response of a rock mass to applied stresses, appropriate estimates of post-failure rock mass characteristics are required (Hoek, 2007). These estimates are obtained through various empirical criteria. Their response to load is described by the material's constitutive behaviour which could be in terms of elasticity, plasticity, viscosity or combinations thereof (Brady and Brown, 2005).

Materials can behave in two general ways in response to applied stresses, namely by elastic or plastic deformation. Deformation is ordinarily assessed via stress-strain curves such as those shown in Figure 2.3a-d. Elastic materials can behave in a linearly-elastic manner where strain increases with an increase in stress, the curve of which (Figure 2.3a, red curve) can be represented by the following equation (Jaeger and Cook, 1979) (Figure 2.3a):

$$\sigma = E\varepsilon \quad (1)$$

where σ is stress, E is Young's Modulus or the elastic modulus, and ε is strain. Young's modulus gives an indication of the work required to deform a rock, where low values indicate less resistance to deformation, thus making it a mechanically weak material (Fossen, 2016). A perfectly elastic material is described by a stress-strain curve being identical during both loading and unloading cycles (Figure 2.3a, blue curve). The slope of this relationship can be described by the following equation (Jaeger and Cook, 1979):

$$E = \sigma/\varepsilon \quad (2)$$

When such stress-strain curves differ during a cycle of loading and unloading, such as that seen in Figure 2.3a (green curve), the rock can be said to be hysteretic (Jaeger and Cook, 1979). The negative ratio of the transverse (ε_2) to axial (ε_1) strain is termed Poisson's Ratio (v) as seen below.

$$v = -\varepsilon_2 / \varepsilon_1 \quad (3)$$

According to Jaeger and Cook (1979), Poisson's ratio is independent of stress for linearly elastic materials and typically range from 0 to 0.5. Fossen (2016) suggests v-values of 0.2 to 0.33 since rock volumes can extend or shorten to a very limited amount due to their confinement in the earth's crust.

Materials which are inelastic undergo plastic deformation which is irreversible (Figure 2.3b-d) (Jaeger and Cook, 1979). Such rocks can maintain a constant volume and stress once the yield point (σ_y), marking the onset of plastic deformation, is achieved, at which point a permanent change in shape takes place (Brady and Brown, 2005). This behaviour is known as perfect plastic deformation (Figure 2.3b). When a component of elastic deformation is incorporated, the material is said to behave as an elastic perfect-plastic material where the stress remains at σ_y while strain continues (Figure 2.3c) (Jaeger and Cook, 1979). Subsequently, the material can behave in a perfectly plastic, strain-hardening or strain-softening manner (Figure 2.3d). Strain hardening occurs when the stress needed for deformation must be increased for strain to build up since the rock becomes stronger and more difficult to deform. In contrast, strain softening is when less stress is needed for deformation to persist (Fossen, 2016).

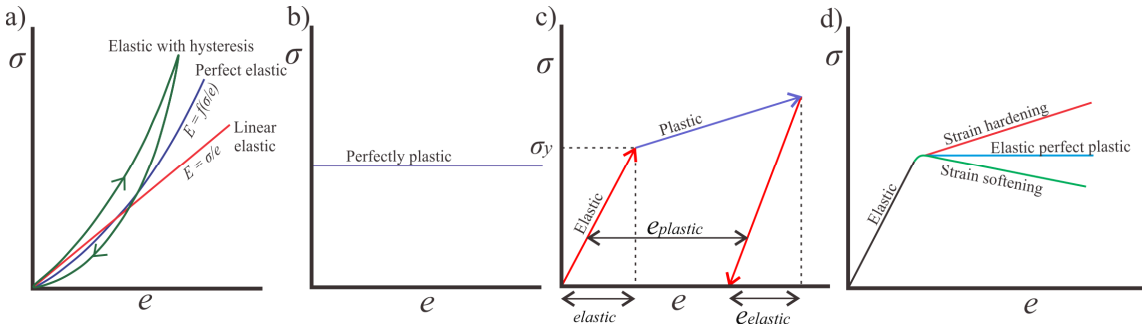

Figure 2.3. Stress-strain curves depicting a) types of elasticity, b) perfectly plastic, c) elastic-plastic, and d) elastic-plastic with strain hardening, softening and elastic perfectly plastic behaviour of isotropic materials (modified from Jaeger and Cook, 1979).

2.3. Rock mass classifications

A rock mass can be defined as a collection of blocks of intact rock material which are separated by a variety of discontinuities, thus implying the need to consider the properties of both the intact rock as well as the entire rock mass, in the classification of rock masses (Bieniawski, 1989). Rock mass classification schemes provide guidance on the selection of these properties (Hoek, 2007). Their development is based on specific case histories, thus implying that considerable caution must be practised in their application to cases deviating from those they were originally developed for (Hoek et al., 1995). It involves the allocation of numerical values to key properties or features of the rock mass in terms of its behaviour.

According to Abbas and Konietzky (2015), rock mass classification systems can be divided into qualitative and quantitative systems, which describe rock mass characteristics descriptively and numerically respectively. Several such systems have been established over the years, some of which include the Deere's Rock Quality Designation (RQD) (Deere, 1964), the Rock Mass Rating (RMR) system (Bieniawski, 1973, 1976, 1989), and the Geological Strength Index (GSI) system (Hoek and Brown, 1997).

2.3.1. Rock Quality Designation (RQD)

The Rock Quality Designation (RQD) index was founded by Deere (1964) as a quantitative estimate of rock mass quality, which is based on the integrity of borehole cores. It can be defined as the percentage of the total length of intact core pieces exceeding 100 mm, to the length of the core run (Hoek, 2007). A low RQD value is suggestive of a densely fractured rock as opposed to a high value indicating sparse jointing. Table 2.2 shows the relationship between RQD values and the quality of a rock mass as proposed by Deere (1968). Hoek (2007) makes mention of the

sensitivity of this parameter to borehole orientation thereby creating grounds upon which data reliability may become compromised. Bieniawski (1989) highlighted the fact that the sole use of this system does not provide a sufficient description of the rock mass as it does not consider several essential joint properties including orientation, tightness and infilling materials.

Table 2.2. Correlation between RQD and rock mass quality (Deere, 1968).

RQD (%)	**Rock mass quality**
< 25	Very poor
25 – 50	Poor
50 – 75	Fair
75 – 90	Good
90 – 100	Excellent

2.3.2. Rock Mass Rating (RMR)

The Geomechanics Classification, better known as the Rock Mass Rating System (RMR) was developed by Bieniawski (1973) and has since undergone several changes, the 1989 (Bieniawski, 1989) version of which will be discussed. This system requires the prior separation of the rock mass into several structural regions based on specific structural features or a change in lithology (Hoek, 2007). Six parameters are subsequently determined for each region and include the uniaxial compressive strength (UCS), RQD, spacing of discontinuities, condition of discontinuities, ground water conditions and the orientation of discontinuities (Appendix A, Table 1). The ratings corresponding to the particular range of values are summed to give the overall RMR, where larger values are indicative of a rock mass of higher quality.

2.3.3. Geological Strength Index (GSI)

The Geological Strength Index (GSI) was developed by Hoek (1994) and was based on field observations of a rock mass which included an assessment of lithology, structure and the condition of fracture surfaces (Marinos and Hoek, 2000) (Appendix A, Figure 1 and 2). With its increasing application to practical rock engineering problems, the index was modified and expanded through a series of papers such as Hoek et al. (1998), Hoek and Marinos (2000) and Marinos and Hoek (2000, 2001) for its use in heterogeneous rock masses (Appendix A, Figure 2) (Hoek, 2007). Six qualitative rock mass structure divisions are considered and include intact/massive, blocky, very blocky, blocky/disturbed/seamy, disintegrated and laminated/sheared rock masses. A further five

discontinuity surface conditions divisions exist and include very good, good, fair, poor and very poor conditions (Appendix A, Figure 1). Based on these classifications, a GSI value can be determined directly from the chart. When this value is used in conjunction with intact rock properties, the reduction in rock mass strength for various geological conditions can be estimated (Hoek, 2007).

According to Hoek and Brown (1997), the GSI value can be estimated from various RMR values for reasonable quality rock masses (i.e. GSI > 25). Using the 1976 RMR version (Bieniawski, 1976), this can be done directly when assuming the rock mass is completely dry (rating of 10) and the discontinuity orientation is very favourable (rating of 0). When using the 1989 RMR version (Bieniawski, 1989) however, the GSI can be calculated using the following equation:

$$GSI = RMR'_{89} - 5 \quad (4)$$

For this simple calculation, the rock mass is assumed to be completely dry (rating of 15) and the adjustment for discontinuity orientation is favourable (rating of 0) (Hoek and Brown, 1997).

2.4. Rock mass failure criteria for jointed rock masses

The strength of a rock mass is a crucial property needed in the assessment of large rock slopes. However, determining the strength of a rock mass is challenging since laboratory tests will not be representative of the rock mass. Moreover, *in situ* tests will not be a practical option with the need to perform many expensive tests (Sjoberg, 1999). These obstacles may be overcome to some degree through empirical approaches known as failure criteria. They can be defined as the stress condition by which the ultimate strength is obtained (Haimson and Bobet, 2014). Several empirical strength criteria exist today, two of which are the Hoek-Brown and Mohr-Coulomb strength criteria. The selection of an appropriate rock failure criterion for a particular situation is not a simple task (Ulusay and Hudson, 2014).

2.4.1. Hoek-Brown failure criterion

Reliable estimates of the strength of jointed rock masses can be acquired using the Hoek-Brown failure criterion (Hoek and Brown, 1980a, b). According to Sheorey (1997), this criterion was originally designed for Panguna andesite rock masses located on Boungainville Island east of Papua New Guinea, but was also fitted to several intact rock data. With extensive application experience since then, this criterion has been modified. It is based on the Griffith theory of brittle fractures (Sjoberg, 1999) where the interlocking of rock blocks and their interface conditions are

also considered (Hoek, 2007). This criterion describes the non-linear strength increase of an isotropic rock with an increasing confining stress (Eberhardt, 2014). It also incorporates additional procedures developed to give estimates of rock mass strength based on laboratory tests and field observations (Eberhardt, 2014). The original Hoek-Brown failure criterion (Hoek, 1983) was presented as:

$$\sigma_1 = \sigma_3 + \sqrt{m\sigma_{ci}\sigma_3 + s\sigma_{ci}^2} \tag{5}$$

Where σ_1 and σ_3 are the major and minor principal stresses at failure respectively, σ_{ci} is the uniaxial compressive strength of the intact rock and m and s are constants. The m constant is comparable to the friction angle (ϕ) for the Mohr-Coulomb failure criterion whereas the s parameter is related to the rock mass cohesion (c) for the Mohr-Coulomb failure criterion and is a measure of the level of fracturing. According to Hoek (1983), higher m values are associated with strong brittle rocks where Mohr envelopes are steep and high friction angles are obtained at low effective normal stresses. In contrast, lower m values are associated with more ductile materials where lower friction angles are observed. The s value ranges from 0 to 1 where 0 represents a more heavily fractured rock with a tensile strength reduced to zero (Eberhardt, 2014).

In the application of this criterion estimating rock mass strength properties, it is assumed that the rock mass responds as an isotropic and equivalent continuum with no preferred failure direction (Eberhardt, 2014). The Hoek-Brown criterion has undergone several updates to improve the estimation of rock mass strength, one being the Generalized Hoek-Brown failure criterion (Hoek et al., 1995):

$$\sigma_1' = \sigma_3' + \sigma_{ci}\left(m_b\frac{\sigma_3'}{\sigma_{ci}} + s\right)^a \tag{6}$$

Where σ_1' and σ_3' are the major and minor effective principal stresses at failure, m_b is the reduced value of the material constant m_i, and is introduced for fractured rock. The m_i constant is a function of the internal properties of the material, including mineralogy and grain size (Hoek et al., 1992) and is given by (Hoek et al., 2002):

$$m_b = m_i\, exp\left(\frac{GSI-100}{28-14D}\right) \tag{7}$$

where GSI is the Geological Strength Index and D is the disturbance factor. The D value relates to the degree to which the rock mass has been disturbed on account of blast damage and stress relaxation. A D value of 1 suggests a very disturbed rock mass as opposed to a value of zero

which represents an undisturbed rock mass. The *a* exponent was introduced in order to lessen the bias concerning hard rock and to account for weaker rock masses (Hoek et al., 1992). The constants *s* and *a* are given by the following two equations (Hoek et al., 2002).

$$s = exp\left(\frac{GSI-100}{9-3D}\right) \tag{8}$$

$$a = \frac{1}{2} + \frac{1}{6}\left(e^{-\frac{GSI}{15}} - e^{-\frac{20}{3}}\right) \tag{9}$$

The uniaxial compressive strength (σ_c) and tensile strength (σ_t) of the rock mass can also be calculated as follows (Hoek et al., 2002):

$$\sigma_c = \sigma_{ci}.s^a \tag{10}$$

$$\sigma_t = -\frac{s\sigma_{ci}}{m_b} \tag{11}$$

According to Hoek (2007), since the Mohr-Coulomb failure criterion was previously written for most geotechnical design calculations, equivalent Mohr-Coulomb parameters, ϕ and c, can be calculated from the Hoek-Brown parameters by fitting an average linear relationship to the Hoek-Brown envelope, for a range of minor principal stresses (σ_3) defined by $\sigma_t < \sigma_3 < \sigma_3{}'_{max}$ (Hoek et al., 2002).

2.4.2. Mohr-Coulomb failure criterion

The Mohr-Coulomb failure criterion remains the simplest and most widely used criterion. It was the outcome of the combined contributions of Charles-Augustin de Coulomb and Christian Otto Mohr (Nadai, 1950). Its establishment stemmed from Coulomb's assumption that failure in rock or soil occurs along a plane which was attributable to the shear stress acting along that plane (Jaeger and Cook, 1979). This criterion comprises of linear equations which define conditions under which an isotropic material will fail (Labuz and Zang, 2012). According to Jaeger and Cook (1979), the criterion can be written as a function of either minor and major principal stresses (σ_3 and σ_1), or as normal stress (σ_n) and shear stress (τ) on a failure plane. The original relationship proposed by Coulomb was based on a study of retaining walls (Heyman, 1972) and was written as:

$$\tau = c + \sigma tan\phi \tag{12}$$

where c is the cohesion, otherwise known as the inherent shear strength, and ϕ is the internal friction angle. This equation forms a straight line on a Mohr diagram from which a tangent to a

circle can be produced. Subsequently, an equation can be written in terms of principal stresses (Labuz and Zang, 2012):

$$(\sigma_1 - \sigma_3) = (\sigma_1 + \sigma_3)\, sin\phi + 2.c.cos\phi \tag{13}$$

$$\tau_m = f(\sigma_m) \tag{14}$$

Where $\tau_m = (\sigma_1-\sigma_3)/2$ and $\sigma_m = (\sigma_1+\sigma_3)/2$. Using these relationships, a Mohr envelope can be drawn on the σ, τ plane (Figure 2.4), and failure is then said to have taken place when the stress at failure, which is the circle of diameter (σ_1-σ_3), is tangent to the failure envelope, τ = g (σ) (Labuz and Zang, 2012).

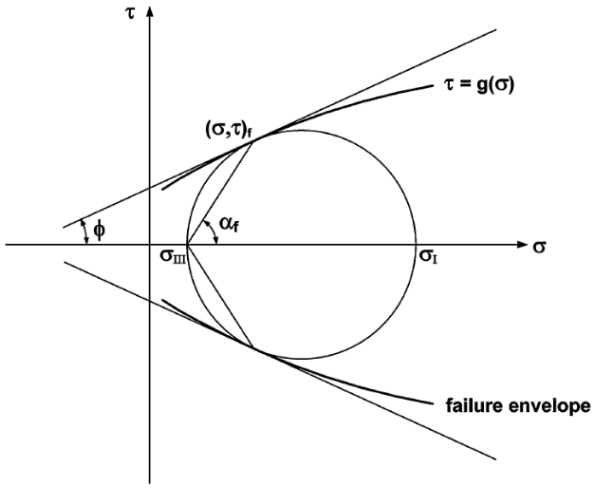

Figure 2.4. Mohr diagram and failure envelopes (Labuz and Zang, 2012).

Equivalent Mohr-Coulomb parameters can be determined by fitting an average linear relationship to the curve produced by the Generalized Hoek-Brown strength criterion (Hoek et al., 1995) for a range of minor principal stress values defined by $\sigma_t < \sigma_3 < \sigma_3{}'_{max}$ (Hoek et al., 2002). Equivalent cohesive strengths (c') and friction angles (ϕ') are achieved by balancing zones above and below the Mohr-Coulomb plot (Hoek et al., 2002).

$$\phi' = Sin^{-1}\left[\frac{6am_b(s+m_b\sigma'_{3n})^{a-1}}{2(1+a)(2+a)+6am_b(s+m_b\sigma'_{3n})^{a-1}}\right] \tag{15}$$

$$c' = \frac{\sigma_{ci}[(1+2a)s+(1-a)m_b\sigma'_{3n}](s+m_b\sigma'_{3n})^{a-1}}{(1+a)(2+a)\sqrt{1+(6am_b(s+m_b\sigma'_{3n})^{a-1})\div((1+a)(2+a))}} \tag{16}$$

Where $\sigma_{3n} = \frac{\sigma'_{3max}}{\sigma_{ci}}$

2.5. Discontinuities

2.5.1. Discontinuities and slope stability

According to Muller (1979), Joseph Stini was one of the early engineers to highlight the significance of discontinuities controlling the behaviour of rock masses. The main geological factor effecting slope stability is discontinuity orientation, but other physical properties of joints such as persistence, roughness and spacing, also play an important role (Hoek and Bray, 1981).

Discontinuity orientation refers to both its dip and dip direction and determines the shape of blocks forming the rock mass (Giani, 1992). Persistence can be defined as the continuous length of a discontinuity within a single plane and it delineates the block size as well as the length of potential failure surfaces (Hoek and Bray, 1981). According to Einstein et al. (1983), discontinuities with a persistence that allows for small rock bridges can substantially increase rock mass strength. Rock bridges refer to the gaps of intact material between disrupted joint planes (Terzaghi, 1962). Hudson and Harrison (1997) define discontinuity roughness as the deviation from planarity. The shear strength of discontinuities, and the factors controlling it, are important in the analysis of discontinuity-dominated rock slopes. This is due to that fact that discontinuity surface roughness increases its shear strength and could play a part in stabilizing rock slopes (Hoek, 2007). Barton (1973, 1976), proposed the following equation to estimate the shear strength of rough discontinuities (τ):

$$\tau = \sigma_n tan\left(\phi_b + JRC log_{10}\left(\frac{JCS}{\sigma_n}\right)\right) \quad (17)$$

where ϕ_b is the basic friction angle of the discontinuity surface, JRC the Joint Roughness Coefficient and JCS the Joint wall Compressive Strength. Joint roughness can be defined qualitatively using descriptive terms, or quantitatively using the JRC, which relies upon visual comparison with predefined standard joint profiles (Figure 2.5) (Giani, 1992). The JCS refers to the compressive strength of the rock on the discontinuity surface and can be estimated in the field using the Schmidt hammer as proposed by Deere and Miller (1966), or from a table presented by the ISRM (1981) which provide a range of values corresponding to a rock mass description regarding rock mass strength. Infilling can be defined as the material existing along a discontinuity which separates two adjacent blocks in a rock mass (Giani, 1992). The detailed description of infilling material is necessary for the prediction of discontinuity behaviour (Hoek and Bray, 1981).

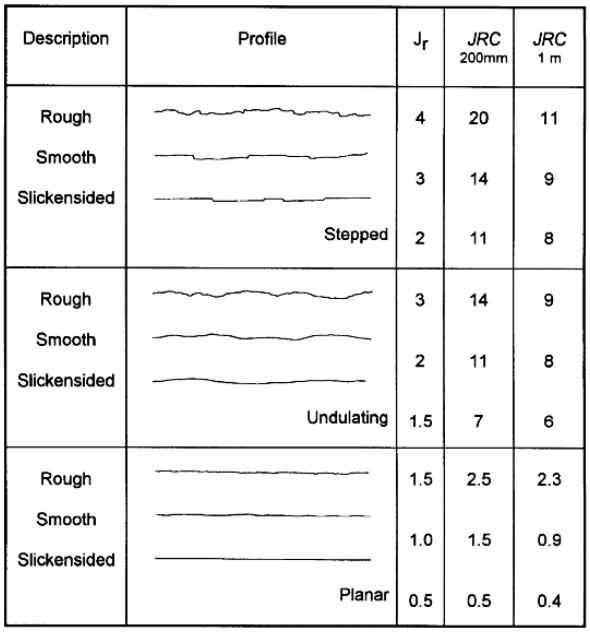

Figure 2.5. Typical profiles associated with JRC values for 200 mm and 1000 mm sample sizes (Barton, 1987).

According to Hoek (2007), the shear strength of discontinuities can reduce significantly if a weaker infilling material occurs along surfaces. Spacing refers to the perpendicular distance between adjacent discontinuities (Giani, 1992). According to Hoek and Bray (1981), the spacing of discontinuities is important as it defines the dimensions of blocks and thus the size of a potentially unstable block. Their dimensions are calculated using spacing, the number of discontinuity sets as well as the persistence, whereas their shapes are determined using only the number of sets and their orientations (Zhang, 2016). Rock mass strength can also be assessed through discontinuity intensity, where highly fractured media tend to form a continuous weak zone due to the merging of multiple closely spaced discontinuities (Hoek and Bray, 1981).

2.5.2. Joint network models

Rock mass jointing is often required to be defined as an assemblage of joints of shared properties, rather than individual joints with distinct properties. This may be due to difficulties involved in describing their exact geometric and mechanical properties such as having partial visibility of an entire joint plane and areas for direct observation being inaccessible (Dershowitz and Einstein, 1988). Numerous methods have been developed to deal with uncertainty related to the geometrical properties of joint networks (Jimenez-Rodriguez et al., 2006). Dershowitz and Einstein (1988) describe several stochastic joint models, where collection of joints are described through an approach known as aggregate characterization. Some of the models that can be employed to simulate rock mass geometry and quantify the spatial variability of joint geometry, include the

Ubiquitous, Parallel Deterministic and Veneziano joint network models. These joint networks are employed in order to observe the behaviour of rock masses with the application of critical joint sets.

2.5.2.1. Ubiquitous joint model

The ubiquitous joint model introduce joints into originally isotropic intact rock to form a jointed rock mass where anisotropy of joint strength and deformability is presented in order for the rock mass to remain isotropic (Wang and Huang, 2009). Directional variation of rock properties, or anisotropy, is typically associated with distinct fabric elements in the form of bedding, foliation in metamorphic rocks or intense jointing (Amadei et al., 1987). According to Jakubec et al. (2001), the ubiquitous joint model can be used for failure simulations and is defined as an anisotropic plasticity model that exhibits strength anisotropy in a series of weak planes with predefined joint parameters. The associated parameters to be specified include the joint direction and shear strength properties, whereas other physical properties not defined, include joint spacing and location (Valdivia and Lorig, 2001). The geomechanical properties of the material and joints determine whether failure takes place through the solid material itself, along a weak plane, or both (Singh et al., 1994; Soren et al., 2014). According to Amadei et al. (1987), during mining operations, principal stress aligns with the direction of dip of ubiquitous joints (Figure 2.6). This stress adjustment encourages movement along these joints and may lengthen them (Cicchini et al., 2001) thereby increasing potential slip surfaces and ultimately, the magnitude of slope failures. The ubiquitous joint model has been used by several authors to account for the presence of weak planes, some of which include Sjöberg (2001); Jakubec et al. (2001); Valdivia and Lorig (2001) and Gang et al. (2003).

2.5.2.2. Parallel deterministic joint model

The parallel deterministic joint network model simulates a network of several parallel joints having a constant orientation, spacing and persistence yet allowing for randomization of the location of joints (Wen et al., 2014; Moradi and Hosseinitoudeshki, 2015). This network can be applied to a rock mass with joints of infinite length as well as non-persistent joints (Figure 2.7a, b). In a finite element analysis comparative study between parallel deterministic, parallel statistical, cross jointed, Baecher, Veneziano and Voronoi joint networks, all having an identical orientation, spacing and density, it was found that the parallel deterministic joint network produced the largest strength reduction factor since the shear strength of rock masses is increased due to the lack of connection in the parallel joints (Moradi and Hosseinitoudeshki, 2015).

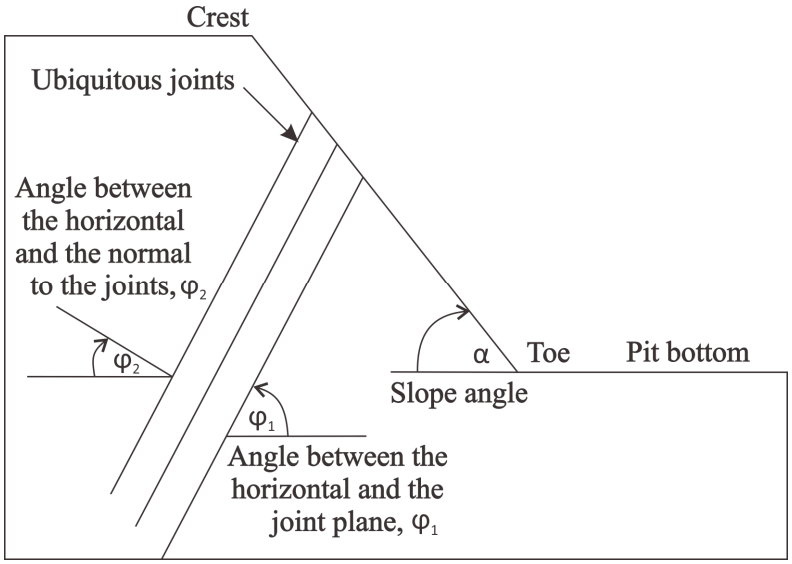

Figure 2.7. Parallel deterministic joint network with a) joints of infinite length and b) non-persistent joints (modified from Rocscience Inc., 2016).

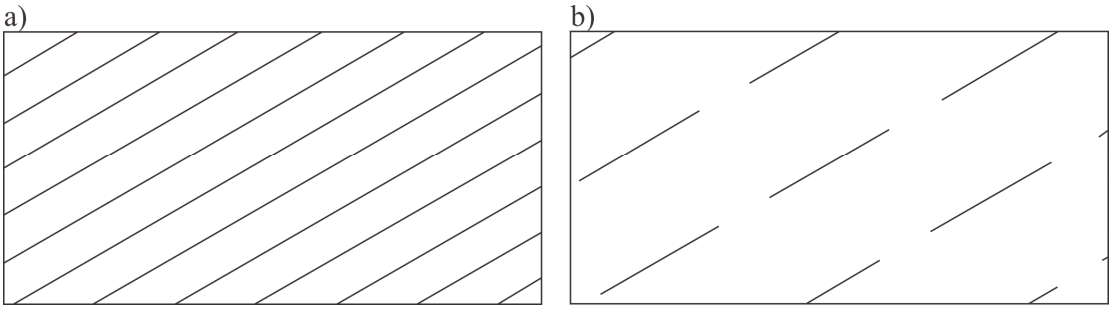

Figure 2.6. Two-dimensional ubiquitous joint model (modified from Sjoberg, 1999).

2.5.2.3. Veneziano joint model

The Veneziano joint model was first developed by Veneziano (1978) to represent trace planes in two or three dimensions. This model is based on the Poisson plane and Poisson line processes (Dershowitz and Einstein, 1988). A system of joints represented by Poisson lines has been found to resemble joint networks in numerous geologies (Dershowitz and Einstein, 1988). The Poisson line process assumes the infinite extent of joints thus introducing problems in simulating unbounded joints, which is why Veneziano (1978) adapted this concept to be employed in the modelling of bounded joints. The improved model is created through three random processes the first being the generation of joint planes as Poisson planes with a specified distribution of orientation (Figure 2.8a). The Poisson line process on each joint plane subsequently divides joint planes into numerous polygons which represent joint shapes (Figure 2.8b). The third and final step involves the random selection of a portion of these polygons, based on persistence, to be

defined as being jointed and the remaining portion as intact rock (Figure 2.8c). This model defines joint size according to the intensity of both the Poisson line process and the amount of 'joint' polygons (Dershowitz and Einstein, 1988). The use of joint planes tends towards coplanar jointing and, in two-dimensional trace planes, these are represented by coplanar segments or fibres (Figure 2.8d).

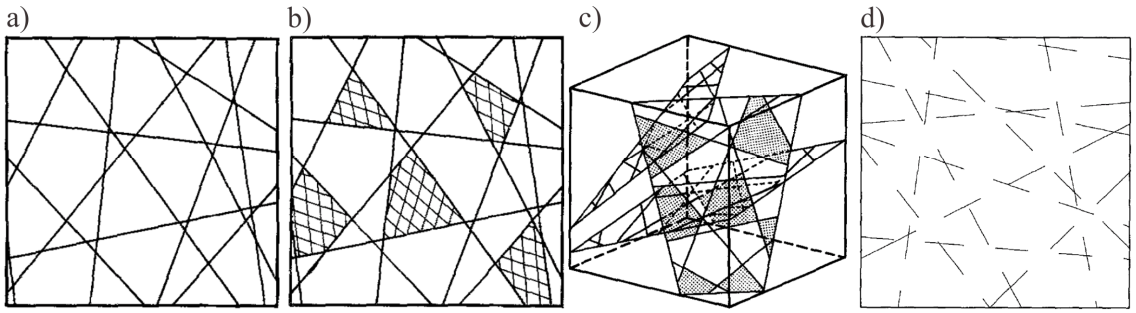

Figure 2.8. Generation of the Veneziano joint system model a) 2D Poisson line process, b) marking of polygonal joints, c) 3-D Poisson plane process, and d) 2D Veneziano model where joints are represented as coplanar segments (Dershowitz and Einstein, 1988).

2.5.3. Non-structurally controlled failure modes

Hudson and Harrison (1997) distinguished between two general failure mechanisms including behaviour as an equivalent continuum, where the failure surface is created through a rock mass, and as a discontinuum, where the failure surface is controlled by pre-existing discontinuities. This section will discuss the non-structurally controlled failure mode of circular failure. Circular failure is the downward movement of material along an approximately circular failure surface which is free to find the line of least resistance through the slope (Hoek and Bray, 1981). (Figure 2.9a). In order to assess a slope for circular failure, a limit equilibrium method of slices is employed where the zone formed by an assumed failure surface is divided into several slices, each slice of which is analysed based on normal and shear forces (Figure 2.9b, c) (Hudson and Harrison, 1997). This will be discussed in detail in Section 2.6.

According to Hudson and Harrison (1997), the position and shape of the failure surface is a function of the strength of the rock, which also depends on the structural characteristics of a rock mass. Figure 2.10 a-e shows such relationships. A near-circular failure surface is associated with an isotropic material which is highly fractured, whereas an elongated surface develops in the direction parallel to anisotropy in anisotropic materials. A failure surface can also follow a major structural feature if present, as opposed to a nearly planar surface developing in granular materials

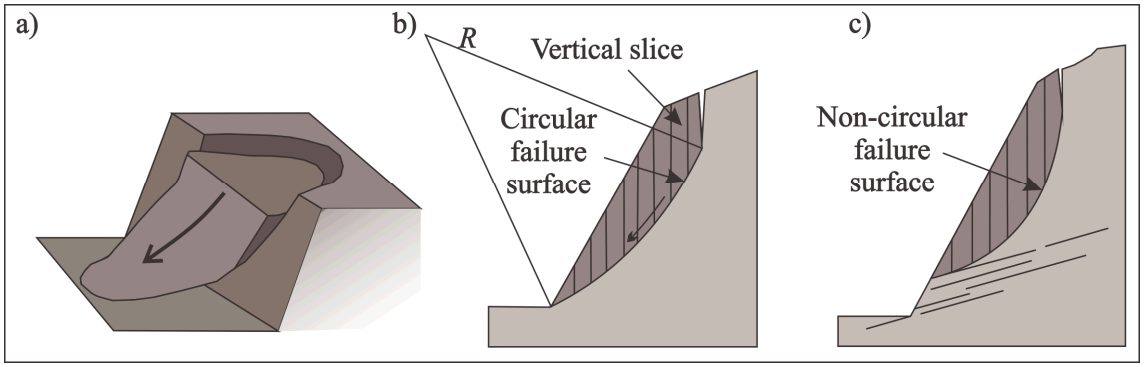

Figure 2.9. Development of curvilinear slips for a) isotropic material, b) anisotropic material, c) major structural feature, d) low cohesion, granular material, and e) inhomogeneous material (modified from Hoek and Bray, 1981).

of low cohesion. The extent of a failure surface can be curtailed with an abrupt change of material strength such as in the case of an igneous intrusion.

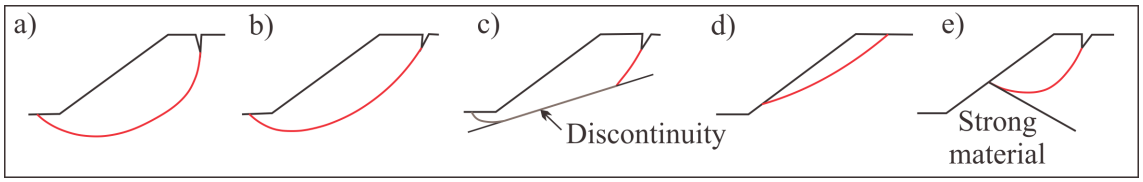

Figure 2.10. Circular failure mechanism (modified from Hoek and Bray, 1981).

2.5.4. Structurally controlled failure modes

Slope failure of hard rock is possible under the influence of gravity alone, if pre-existing discontinuities exist to allow movement of discrete blocks (Goodman, 1989). Such failures include three basic modes being plane, wedge and toppling. An initial approach that can be used to establish the possibility of such instabilities is by a method of kinematic analysis, which considers the movement of blocks without taking into account the forces that produce them (Hudson and Harrison, 1997). Kinematic analysis, developed by Markland (1972), can be defined as a form of slope stability analysis which determines the potential mode of failure based on geometric properties of the rock mass, including discontinuities' orientations and slope face angles (Kliche, 1999). This is performed using a stereographic representation.

2.5.4.1. Plane failure

Plane failure is the downward movement of a rigid block along a single discontinuity plane (Hoek and Bray, 1981). The occurrence of plane failure requires 4 geometrical conditions to be met.

Firstly, the failure plane (ψ_p) should daylight, or be shallower than, the slope face (ψ_f) (Figure 2.11a). Secondly, the sliding plane must strike within approximately 20° of the slope face. These limits, together with slope face, defines the daylight envelope which gives an immediate indication of potentially unstable blocks (Figure 2.11c). Thirdly, the dip of the failure plane must exceed its friction angle (ϕ_j) (Figure 2.11a) and finally, release surfaces must exist in order to define the lateral boundaries of the sliding block (Figure 2.11b). Tension cracks should be considered as an indication of possible imminent slope instability (Hoek and Bray, 1981). Barton (1971) mentions that it must be assumed that when a tension crack develops and is visible at a slope surface, shear failure has commenced within the rock mass.

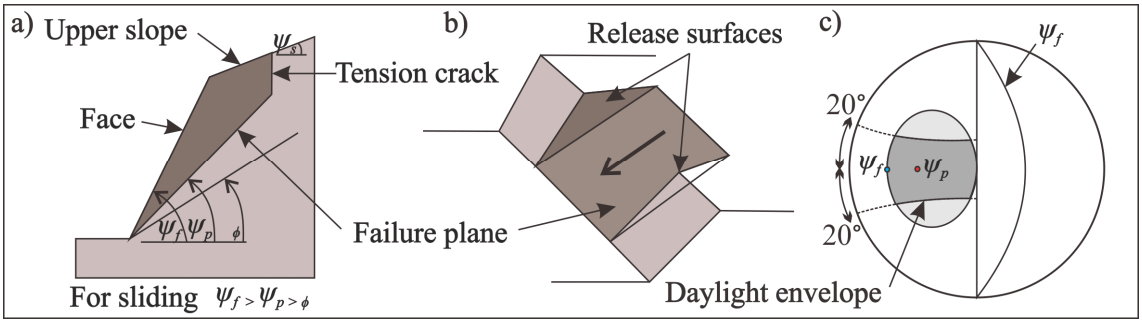

Figure 2.11 Plane failure mechanism a) plane failure in cross-section b) release surfaces at ends of plane failure and c) kinematic feasibility (modified from Hoek and Bray, 1981).

2.5.4.2. Wedge failure

Wedge failure refers to the downward movement of a tetrahedral block which is formed by the intersection of two discontinuities (Goodman, 1989). There are several slope geometry conditions that should be satisfied for wedge failure to take place. Firstly, two planes must intersect one another to form a line of intersection (ψ_{int}) (Figure 2.12a, b). Secondly, the plunge of this line (α_{int}) must be shallower that the dip direction of the slope face (ψ_f) and steeper than the average friction angle (ϕ_j) of the two planes forming the intersection (Figure 2.12c, d). Finally, the line of intersection must dip out of the slope face (Figure 2.12).

A kinematic analysis can also help establish if sliding will occur along a single plane, along both planes or along their line of intersection. According to Hoek and Bray (1981), if the dip direction of the two planes of weakness lies outside the angle between α_{int} and α_f, the wedge will slide along both planes, if however the dip direction of one of the planes (α_A or α_B) falls between this angle, the wedge will slide along that plane alone (Figure 2.11c, d). Wedge instability should be

analysed via a three-dimensional model as opposed to plane and toppling failure modes which could be analysed in two dimensions (Kliche, 1999).

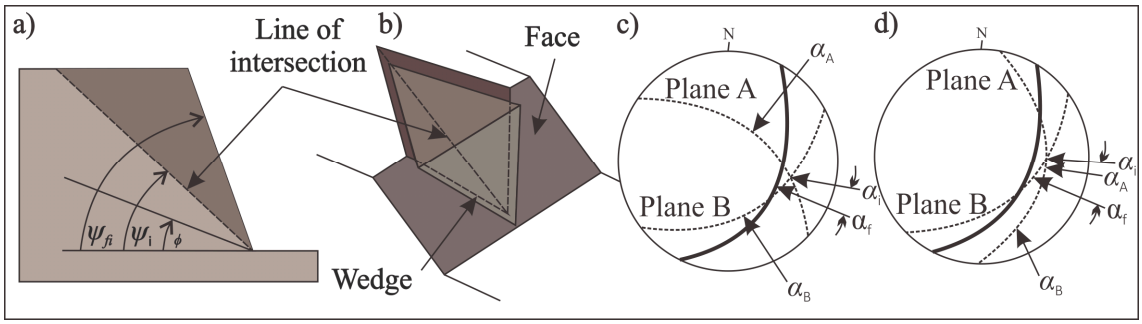

Figure 2.12. Wedge failure a) geometric conditions, b) line of intersection, c) kinematics of wedge failure along a line of intersection and d) wedge failure along discontinuity plane A (modified from Hoek and Bray, 1981).

2.5.4.3. Toppling failure

Goodman and Bray (1976) define the process of toppling failure as the overturning of columns of rock, and differentiate between three basic types of toppling failures including block, flexure and block-flexure toppling, each of which requiring a slightly different stability analysis.

Block toppling takes place when the rock columns are separated by widely spaced discontinuities and involves overlying larger columns transferring a load to the underlying shorter columns at the toe of the slope thereby thrusting them forward and allowing for further toppling to occur (Goodman and Bray, 1976) (Figure 2.13a). According to Hoek and Bray (1981), this failure mode is associated with strong rock masses with natural discontinuities, such as bedded sandstone and columnar basalt, in which columns are formed by a steep discontinuity set dipping into the face and another set of widely spaced orthogonal discontinuities defining the height of the column. For this failure mode to be kinematically feasible, an intersection between two discontinuities must dip into the slope face and another discontinuity set must exist to form a release plane (Hudson and Harrison, 1997). The former should occur between a zone enclosed by straight line lateral limits and an outer curved limit defined by the slope face angle. If they occur outside the straight line lateral limits, but within the friction cone of the base planes, oblique toppling may take place. Poles associated with potential base planes represent release planes if they plot within the lateral limits and friction cone, and both release and sliding planes if they plot within the lateral limits, but outside the friction cone.

Flexural toppling occurs in rock slopes with a single preferred discontinuity network of fairly continuous length, where the columns break as they bend forward under the influence of gravity (Figure 2.13b). Provided that the toe of the slope may move, flexural cracks will develop in the overlaying layers which will allow for the release of a large mass of material (Goodman, 1989). According to Wyllie and Mah (2004) this failure mode is associated with rock masses with poorly developed orthogonal joints such as thinly bedded shale and slate. To make this failure mode kinematically feasible, discontinuities should occur outside of the slip limit plane and within the lateral limits. The slip limit dip denotes the difference between the slope and friction angles, whereas its dip direction is identical to that of the slope face. Block-flexure toppling, in contrast, is more complex and is characterised by pseudo-continuous bending along columns separated by several joints, and is caused by accumulated displacements on the cross-joints (Goodman and Bray, 1976) (Figure 2.13c).

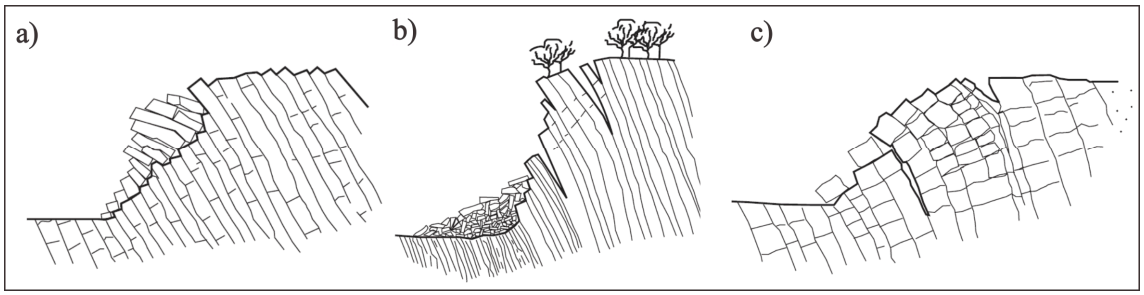

Figure 2.13. Common types of toppling failures: a) block toppling, b) flexural toppling and c) block-flexure toppling (Goodman and Bray 1976).

2.6. Slope stability analysis

Rock slope instability represents a significant safety hazard in mining environments around the world. It is the cause of serious injuries and fatalities, as well as major financial losses when production is temporarily terminated for safety measures, or infrastructure and machinery have been damaged. Since open pit mines are dynamic environments where there is a continuous modification of pit geometry with mining operations, it is important to assess slopes for potentially adverse conditions that may give rise to failures. Common methods of slope stability analyses include the Limit Equilibrium Method (LEM), Finite Element Method (FEM) and the Finite Difference Method, all involving the use of computer software (Cheng and Lau, 2008).

2.6.1. Limit Equilibrium Methods

Limit equilibrium methods (LEM) of slices can be employed to calculate the factor of safety (FoS) for circular, composite or fully specified failure surfaces (Stead et al., 2006). The approach has undergone several developments from the original method proposed by Fellenius (1927). There are numerous methods of slices which vary in terms of the statics used in deriving the safety factor as well as the assumptions employed to render the problem statistically determinate (Fredlund, 1975). The general procedure in calculating the safety factor involves the summation of forces in two directions as well as moments. However, to make the problem determinate, additional information regarding normal and interslice force distributions in the form of assumptions, are required, thus, creating different methods of limit equilibrium analysis (Fredlund and Krahn, 1977).

Some of the limit equilibrium methods can be seen in Table 2.3. All share the same definition of the safety factor, which is the ratio of shear strength to shear stress. According to Whitman and Bailey (1967), all methods can be classified, based on force and moment equilibrium conditions, into in either simplified or rigorous methods. Simplified methods can only satisfy one of the conditions, but not both simultaneously. In rigorous methods where, both can be satisfied together, but at the expense of a simple analysis. Figure 2.14 shows a cross-section of an individual slice, where the base of the slice is inclined at angle ψ_b and has an area of A. The forces acting on the base include the shear resistance (S), which incorporates the shear strength properties cohesion (c_i) and friction angle (ϕ_i), as well as forces E_i ,which include the dip angle (ψ_i) and height (h_i) above the base and which act on the sides of the slice (Hoek and Bray, 1981).

Based on methods best suited for a specific failure surface shape, two limit equilibrium methods will be discussed, namely the Bishop Simplified and Janbu Corrected methods. The Bishop Simplified method, proposed by Bishop (1955), satisfies moment equilibrium and vertical force equilibrium, but neglects horizontal force equilibrium. The safety factor calculation is identical to that of the Ordinary Method, but a variation in normal force definition exists (Fredlund and Krahn, 1977). This method applies to circular failure surfaces and is not recommended for non-circular surfaces, due to unbalanced horizontal forces (Cheng and Lau, 2008). Janbu's Corrected Method, proposed by Janbu et al. (1956), satisfies both horizontal and vertical force equilibrium and neglects moment equilibrium. It makes use of an empirical correction factor (f_o) to account for the effect of interslice shear forces, which are assumed to be zero, and then multiplying this factor by the computed factor of safety (Fredlund et al., 1981). The correction factor is a function of cohesion and the internal friction angle, as well as the failure surface (Fredlund and Krahn, 1977). This method may be employed for non-circular failure surfaces (Cheng and Lau, 2008).

Table 2.3. Characteristics of limit equilibrium methods of slope stability analysis (after Duncan and Wright, 1980).

Method	Characteristic
Slope Stability Charts (Taylor, 1937; Janbu, 1968; Hoek and Bray, 1981)	Accurate enough for many purposes Faster than detailed computer analyses
Ordinary Methods of Slices (Fellenius, 1927)	Only for circular slip surfaces Satisfies moment equilibrium Does not satisfy horizontal and vertical force equilibrium
Bishop's Modified Method (Bishop, 1955)	Only for circular slip surfaces Satisfies moment equilibrium Satisfies vertical force equilibrium Does not satisfy horizontal force equilibrium
Force Equilibrium Methods (e.g. Lowe and Karafiath, 1960; U.S. Army Corps of Engineers, 1970)	Any shape of slip surfaces Do not satisfy moment equilibrium Satisfies both vertical and horizontal force equilibrium
Janbu's Generalized Procedure of Slices (Janbu, 1968)	Any shape of slip surfaces Satisfies all conditions of equilibrium Permits side force locations to be varied More frequent numerical problems than some other methods
Morgenstern and Price's Method (Morgenstern and Price, 1965)	Any shape of slip surfaces Satisfies all conditions of equilibrium Permits side force orientations to be varied
Spencer's Method (Spencer, 1967)	Any shape of slip surfaces Satisfies all conditions of equilibrium Side force are assumed to be parallel

According to Duncan (1996), the assumptions made for methods that satisfy all conditions of equilibrium do not have a significant effect on the safety factor, but methods that satisfy force equilibrium alone calculate safety factors which are strongly influenced by the assumed inclinations of the side forces existing between the slices.

Aside from the assumptions the methods are based on, a major limitation of the LEM is the notion that the stress-strain behaviour of the material is ductile since no information regarding strain levels and strain variation along the failure surface is provided. This thus suggests uncertainty of peak strength being mobilized all together and across the entire failure surface, and the potential of progressive failure (Duncan, 1996).

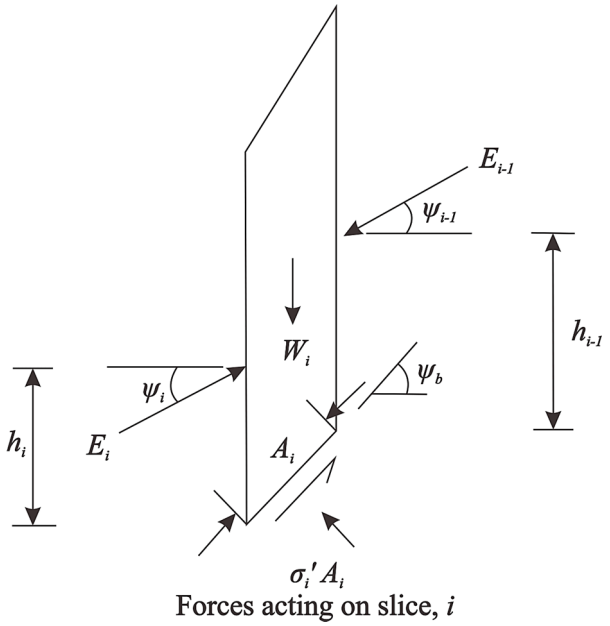

Figure 2.14. Forces acting on a slice (modified from Hoek and Bray, 1981).

2.6.2. Numerical modelling

Ore bodies are often linked to intrusions and faults, thus resulting in typically non-uniform material properties (Hoek et al., 1991). For this reason, the LEM can be inappropriate in analysing more complex conditions surrounding pit excavations thereby presenting the need for numerical methods. Numerical methods of slope stability analysis compute approximate solutions to problems, incorporating strain during failure (Stead et al., 2006). Numerical models refer to computer codes that portray the behaviour of a rock mass which has been exposed to several initial conditions, which could include *in situ* stresses and water pressure, boundary conditions, and induced modifications to the surroundings (Lorig and Varona, 2001). The availability of powerful computers has resulted in such stability studies being done more efficiently and accurately than in the past (Duncan, 1996).

The FoS in numerical methods can be calculated by an approach known as the Shear Strength Reduction (SSR) technique, which dates back four decades when it was first used by Zienkiewicz et al. (1975). This technique works by reducing shear strength properties, cohesive strength (c) and angle of friction (ϕ), until failure takes place (Matsui and San, 1992). It enables the computation of the sliding plane, since the failure mechanism is directly related to the development of shear strain, and a reduction in shear strength will thus lead to an increase in shear strain and the development of a potential failure zone (Matsui and San, 1992). Simulations are

run for a series of increasing trial safety factors (f) each corresponding to a reduction of strength properties (ϕ_{trial} and c_{trial}) as seen below (Hoek and Bray, 1981):

$$c_{trial} = \left(\frac{1}{f}\right) c \tag{18}$$

$$\phi_{trial} = arctan\left(\frac{1}{f}\right) tan\phi \tag{19}$$

With a gradual increase of f or the Strength Reduction Factor (SRF) and a corresponding reduction in shear strength, a critical SRF or FoS is calculated from local safety factors along the failure surface (Matsui and San, 1992). Cheng et al. (2007) pointed out that the advantages of using the SSR technique are threefold. Firstly, the critical failure surface is determined automatically by use of gravity as a load and the gradual reduction of the shear strength properties. Secondly, it does not require assumptions to be made on the distribution of the interslice shear force. Lastly, it can be applied to complex conditions and provide useful information such as stress and displacement.

Lorig and Varona (2001) discussed the general procedure of numerical modelling, which operates by dividing a rock mass into a series of elements or zones, which may be connected (continuum models) or separated by discontinuities (discontinuum models), and then allocating a material constitutive model and properties to each. The outcome of the simulations could be that of equilibrium or collapse of the rock mass, where the latter displays the mode of failure. For the purpose of this study, continuum methods of slope stability analysis will be discussed.

Continuum methods are good alternatives to the conventional LEM since they are accurate, versatile and require minimal assumptions to be made (Griffiths and Lane, 1999). According to Stead et al. (2001), continuum methods are best applied to slopes comprised of massive, intact rock, weak rock or heavily fractured rock masses. Hoek et al. (1991) suggest their suitability for conditions relating to heterogeneous and non-linear properties due to the fact that each element explicitly models the behaviour of its allocated material. Continuum codes typically employed in the analysis of rock slopes include the Finite Element Method (FEM) and Finite Difference Method (FRM). In practice, these methods are typically indistinguishable (Hoek et al., 1991). They solve an identical set of algebraic calculations, but vary in terms of means in deriving these equations. Implicit techniques, such as the FEM code Phase2 (Rocscience Inc., 2015), solve systems of linear equations in matrix form. In contrast, explicit techniques, such as the FDM code FLAC (Itasca, 2011), uses a time-marching procedure called dynamic relaxation (Dawson et al., 1999). The implicit technique is appropriate where simple constitutive laws are employed. Although the non-linear behaviour of materials can be resolved through the modification of stiffness coefficients and/or stress and strain variables, increasing non-linearity requires more

solution steps, thereby lowering efficiency (Hoek et al., 1991). For this reason, the explicit technique can be more effectively applied where more complex constitutive relations occur. Both models require several critical input parameters including a representative slope geometry, a constitutive criterion, groundwater characteristics, shear strength properties and *in situ* stresses (Coggan et al., 1998).

These methods have the advantages of allowing for material deformation and failure, being able to model complex failure mechanisms and assessing the effects of groundwater and parameter variation with reasonable computing run times (Coggan et al., 1998). Coggan et al. (1998) lists the following limitations. Firstly, there is a need for an excellent understanding of the code in use. A great deal of data is also required, some of which typically have limited availability since not all necessary parameters are measured routinely. Difficulties also arise when modelling highly jointed slopes. Lastly, sensitivity analyses are difficult due to increased run times.

From the above discussion, it is clear that numerical models could be more beneficial over conventional limit equilibrium methods. Wyllie and Mah (2004) compared the two methods in terms of their capabilities (Table 2.4) which highlights the proficiencies of numerical modelling methods.

Table 2.4. Comparison of numerical and limit equilibrium analysis methods (Wyllie and Mah, 2004)

Analysis result	Numerical solution	Limit equilibrium
Equilibrium	Satisfied everywhere	Satisfied only for specific objects such as slices
Stresses	Computed everywhere using field equations	Computed approximately on certain surfaces
Deformation Failure	Part of solution Yield condition satisfied everywhere; slide surfaces develop "automatically" as conditions dictate	Not considered Failure allowed only on certain pre-defined surfaces; no check on yield condition elsewhere
Kinematic	The "mechanisms" that develop satisfy kinematic constraints	A single kinematic condition is specified according to the particular geologic conditions

2.7. Rockfall hazard assessment

Rockfall represent another form of slope instability, and is an additional threat in surface mines which can occur frequently. While rockfalls are sometimes considered a minor problem in comparison to large scale slope instabilities involving benches or sometimes even overall pit

slopes, costs rise when maintenance and remedial measures are required. In recent years rockfall has been widely studied in the context of surface mining. Rockfalls are characterised by high energy and mobility, thus making them a major cause of injury and fatality (Agliardi and Crosta, 2003). Rockfall simulators can be employed to assess the danger of an exclusively detached rock by analysing its trajectory based on changes in velocity (Stead et al., 2001).

According to Giacomini et al. (2012), rockfall events are typically linked to geological features, fractures developed by blasting, as well as machinery operating directly above crests and alongside roads at the bottom of highwalls. In addition, the effect of blasting vibration on rock slopes generally lead to backbreak at the crest and underbreak at the toe of the bench, resulting in a geometry which varies from the original theoretical optimum design. Peckover and Kerr (1977) identified several factors that contribute to the detachment of rock fragments from a rock mass. These include discontinuity orientation, spacing and strength; water pressure and frost-wedging; earthquake or blasting-induced vibrations as well as weathering, precipitation, temperature variations and vegetation prying. Detached rocks may move by free falling, bouncing, rolling or sliding (Giani, 1992).

In order to identify the nature of a rockfall hazard, high risk areas should be delineated based on potential risk. A rating system such as the Rockfall Hazard Rating System developed by Pierson et al. (1990) for the Oregon State Highway Division, is useful in identifying areas of greatest risk to rockfalls. The process of the RHRS in terms of slope stability analysis includes the development of a slope inventory, assigning a preliminary rating to previously determined problem zones, and then assigning a detailed rating by prioritizing the most hazardous zones. Once high risk areas have been defined, more detailed and site specific analyses can be performed.

Over the past few decades, the prediction of rockfall behaviour has made many advancements through the development of numerous sophisticated computer programs designed to simulate the path of a rock moving down a slope face (Pfeiffer and Bowen, 1989; Guzetti et al., 2002). This process involves the analysis of trajectories, bounce height, velocity and energy (Alejano et al., 2007). The issue of rockfall in open pit mining has been analysed by a number of authors who have proposed simple estimate approaches, or more sophisticated reliability based models, but which are always aimed at maximizing profits. Improved safety, however, is a major concern for the mining industry, since hazardous operations are both potentially life threatening and significantly raise costs. The prediction of rockfall behaviour is critical in the selection and design of effective protection measures (Hoek and Bray, 1981), thus improving safety in the mining environment. Resulting protective measures can either prevent rock fall events from occurring or can control their consequences. Preventative measures, also known as active systems, include

features such as wire anchors and rock bolts, whereas controlling measures, also known as passive systems, include benches, catch ditches, catch fences and attenuator systems (Giacomini et al., 2012).

Hungr and Evans (1988) classified rockfall simulation models as lumped-mass or rigorous models where the former represent falling bodies as point masses and do not consider the shape and size of the falling rock. According to Basson (2012), rotational movements are not simulated with this method since only the mass component of the moving body is utilized in the calculation of energies. Rigorous models in contrast include a range of approaches that take rock shape, volume and all rock movements into account (Giani, 1992). Difficulties arise however, in obtaining realistic input data for such parameters thus resulting in their limited use (Alejano et al., 2007).

Rockfall simulation codes can follow two-dimensional (2D) or three-dimensional (3D) approaches. A 2D approach is favoured from an operational and computational point of view, however the interpretation of the results and their extension to neighbouring areas are subjective (Crosta and Locatelli, 1999). Their simulation is performed along user-specified predefined slope profiles and assume that rockfall occurs along a linear plane and that the trajectory is unaffected by the plane of the slope or fall body (out of plane bouncing is not considered). Since the 3D effect of slope geometry plays a major role in controlling the dynamics of a falling block, this poses a severe limitation of 2D models, particularly in areas where even minor changes in topography can significantly influence a rockfall (e.g. along steep channels where the topography is concave or convex or at the apex of a fan) (Crosta and Locatelli, 1999). In the case of open pit mines, the altered topographic surface, due to overbreak and underbreak resulting from blasting operations, could lead to a more critical profile. A 3D rockfall simulation model is superior to a 2D model as it takes into account the 3D effect of topography on rockfalls. The most important effect is the "lateral dispersion" of rockfall trajectories (Crosta and Agliardi, 2004), i.e. the ratio of the lateral distance separating the extreme fall paths to the slope length (Azzoni et al., 1995). The occurrence of lateral dispersion thus makes it difficult to choose a priori the right rockfall path when a 2D approach is adopted (Agliardi and Crosta, 2003).

To summarize, 2D rockfall simulations are performed along a slope profile which is defined by the program user and as a result, neglect the highly influential 3D effects of topography. On the contrary, 3D simulation models are more sophisticated in that rockfall trajectories are modelled based on a 3D topography (Charalambous and Sakellariou, 2007; Basson, 2012).

CHAPTER THREE
METHODOLOGY

3.1. Overview

Slope stability analyses were based on three representative critical profiles which were selected from areas of known concern in terms of problematic design domains and pertaining to reports by Consultant D (2011) (Figure 3.1). The geotechnical model, comprising the geological, structural and rock mass models of these profiles, were found to vary in terms of the number of materials each profile possesses, where profile B consists of a single material as opposed to profiles A and C having multiple materials (Figure 3.2). An overview of the regional geology is given in Section 3.2.1. Kinematic analyses for structurally controlled failure modes (i.e. planar, wedge, and toppling failure) were performed using Dips (Rocscience Inc., 2015). The most precarious discontinuity sets identified were further analysed using the Limit Equilibrium Method (LEM) via RocPlane, Swedge and RocTopple programs (Rocscience Inc., 2015) (Figure 3.1). At this stage, major discontinuity set orientations were identified and introduced as predefined failure planes in order to determine safety factors and probabilities of failure. Safety factors were also obtained for non-structurally controlled failure mechanisms via the LEM of slices using Slide (Rocscience Inc., 2015), which assumes a stress controlled circular failure mode. The Bishop simplified (Bishop, 1955) and Janbu corrected (Janbu, 1954; Janbu, 1968) methods of analysis were employed to estimate these safety factors.

The next stage of this study involved the numerical modelling of profiles using a Finite Element Method (FEM) and Finite Difference Method (FDM) of analysis via two-dimensional continuum codes, Phase2 (Rocscience Inc., 2015) and FLAC (Itasca, 2011) and in conjunction with the Shear Strength Reduction (SSR) technique (Figure 3.1). Two types of geotechnical models were explored, a continuum and pseudo-discontinuum approach. For the pseudo-discontinuum approach, mean joint sets responsible for potential planar and wedge failure, determined using the LEM, were incorporated into profiles as two-dimensional joint networks in order to test the identified structurally controlled failure modes. Simplifying the structural data, joints were incorporated into finite element models as Parallel Deterministic and Veneziano joint network models (Veneziano, 1978). The former was applied as joints of infinite length, and subsequently of finite length with rock bridges introduced along discontinuity planes (Figure 3.1). Results were compared to those produced in FLAC (Itasca, 2011) using the Ubiquitous joint network model due to similarity in joint spacing, length and density. In order to introduce stochastic and thus more realistic joint conditions, the Veneziano joint network (Veneziano, 1978) was employed.

This model was selected to represent potentially unstable joints since Dershowitz and Einstein (1988) found that the Poisson line process, on which it is based, corresponded well with observed rock joint systems in a number of geologies.

The rock mass in the continuum approach was modelled as a linear-elastic-perfectly plastic materials through the application of both the Generalized Hoek-Brown strength criterion (Hoek et al., 2002) and equivalent Mohr-Coulomb parameters, determined from a range of minor principal stress values defined by $\sigma_t < \sigma_3 < \sigma_3{}'_{max}$ (Hoek et al., 2002). In contrast, materials were modelled solely with equivalent Mohr-Coulomb parameters for pseudo-discontinuum approaches since the Ubiquitous joint network model restricts the use to this constitutive model. The orientation of ubiquitous joints also corresponded to the potentially unstable conditions determined by major joint sets responsible for plane and wedge failure using the LEM. The strength properties of the rock mass associated with these criteria were estimated in RocLab (Rocscience Inc., 2015) by utilizing the combined data from consultants A (1996), B (2006) C (2009) and D (2011).

Rockfall hazards were identified from reports by Consultant D (2011) and were thus analysed in the current study. The rockfall hazard assessment was conducted using the two-dimensional RocFall (Rocscience, 2015) and three-dimensional Trajec3D (BasRock, 2016) codes (Figure 3.1). Three profiles representing good slope/cut slope topography to poor slope/cut slope topography were employed to consider the effect of backbreak at the crests and underbreak at the toes of berms. Input parameters were based on data from Consultant D (2011). Both codes are based on rigid body dynamics where the shape and volume of falling rocks are considered in both programs, and results and were compared.

3.2. Rock mass properties

3.2.1. Overview of regional geology

The open pit mine of interest is located on the Zimbabwe Craton in southern Africa (Figure 3.3). The Archaean Zimbabwe Craton is bordered by the Limpopo Belt to the south, the Magondi Supergroup to the northwest, the Zambezi Belt to the north and the Mozambique belt to the east (Schlüter, 2006). It comprises predominantly Paleoarchaean granitic gneisses, Neoarchaean granitoids and schists as well as greenstone belts, and is overlain by Proterozoic and Phanerozoic sedimentary basins in the northwest, north and east (Schlüter, 2006). According to Consultant D (2011) the metallic ore body is hosted in NNW-SSE trending metagabbro which is intruded into tonalite gneiss forming the wall rock. Numerous subvertical dolerite dykes and brittle shear zones

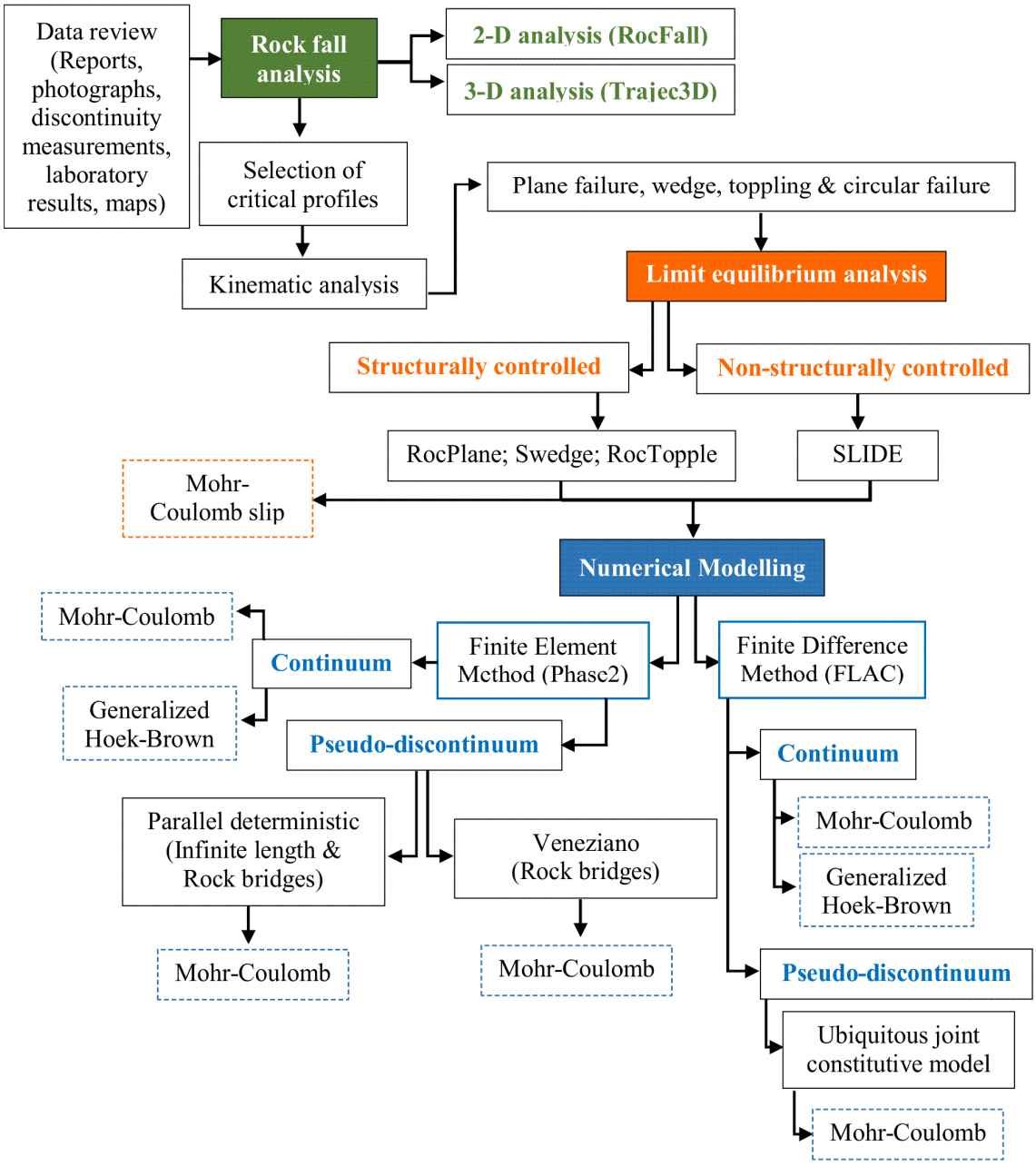

Figure 3.1. Overview of study methodology.

occur throughout the pit. Metagabbro and tonalite forms part of the Archaean greenstone belts which were emplaced 3.5 and 2.5 Ga (Blenkinsop et al., 1997). The younger WNW-ESE striking dolerite intrusions form part of the Okavango Dyke Swarm which spans 1 500 km from Namibia to Zimbabwe and through Botswana and reaches widths of approximately 100 km (Gall et al., 2005). Ages of 178.4 ± 1.1 and 179.3 ± 1.2 Ma have been identified by Elburg and Goldberg (2000) and Gall et al. (2002). Consultant D (2011) also mentions widespread brittle-ductile shear

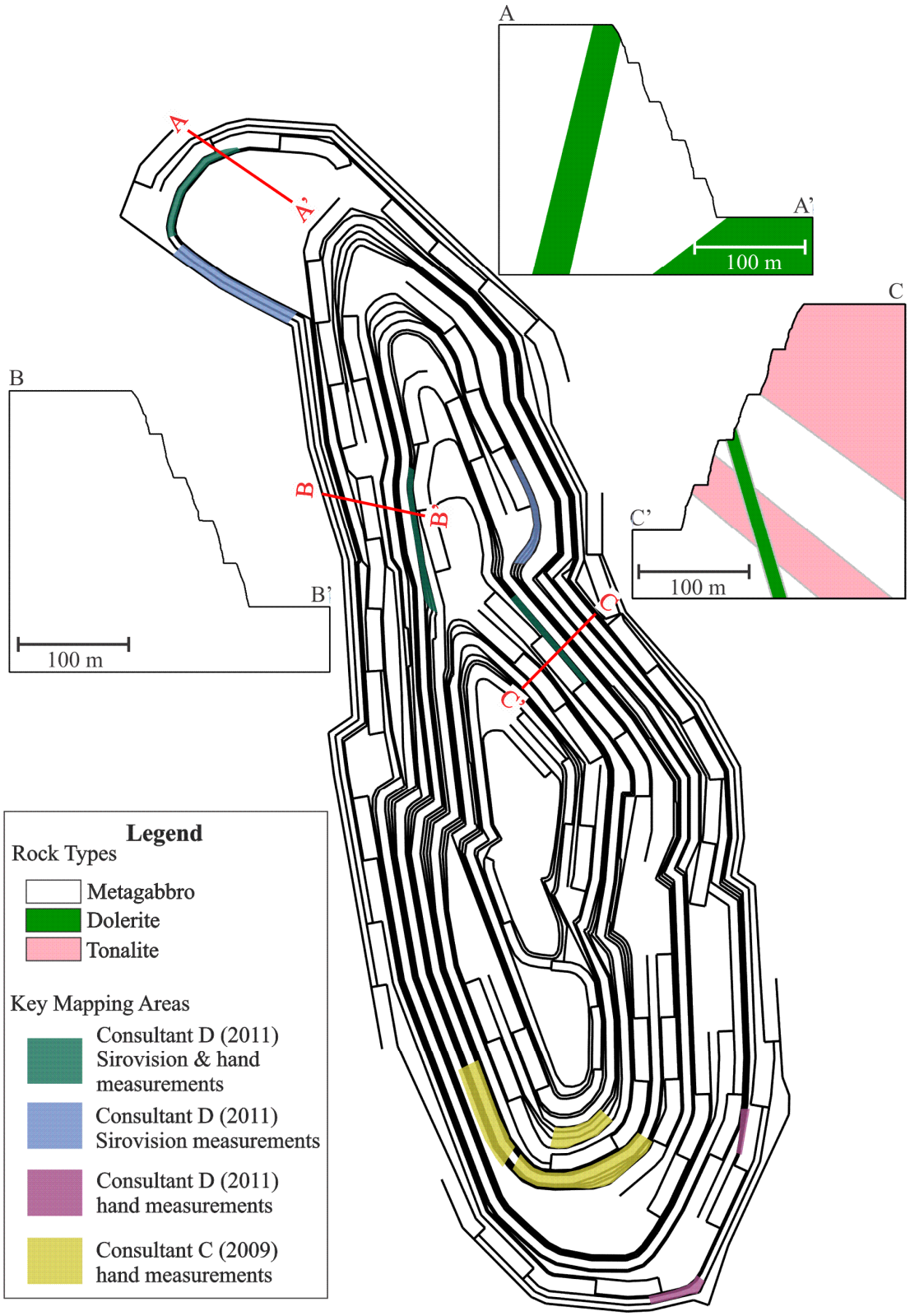

Figure 3.2. Pit configuration and measurement zones from consultants with critical profiles' locations.

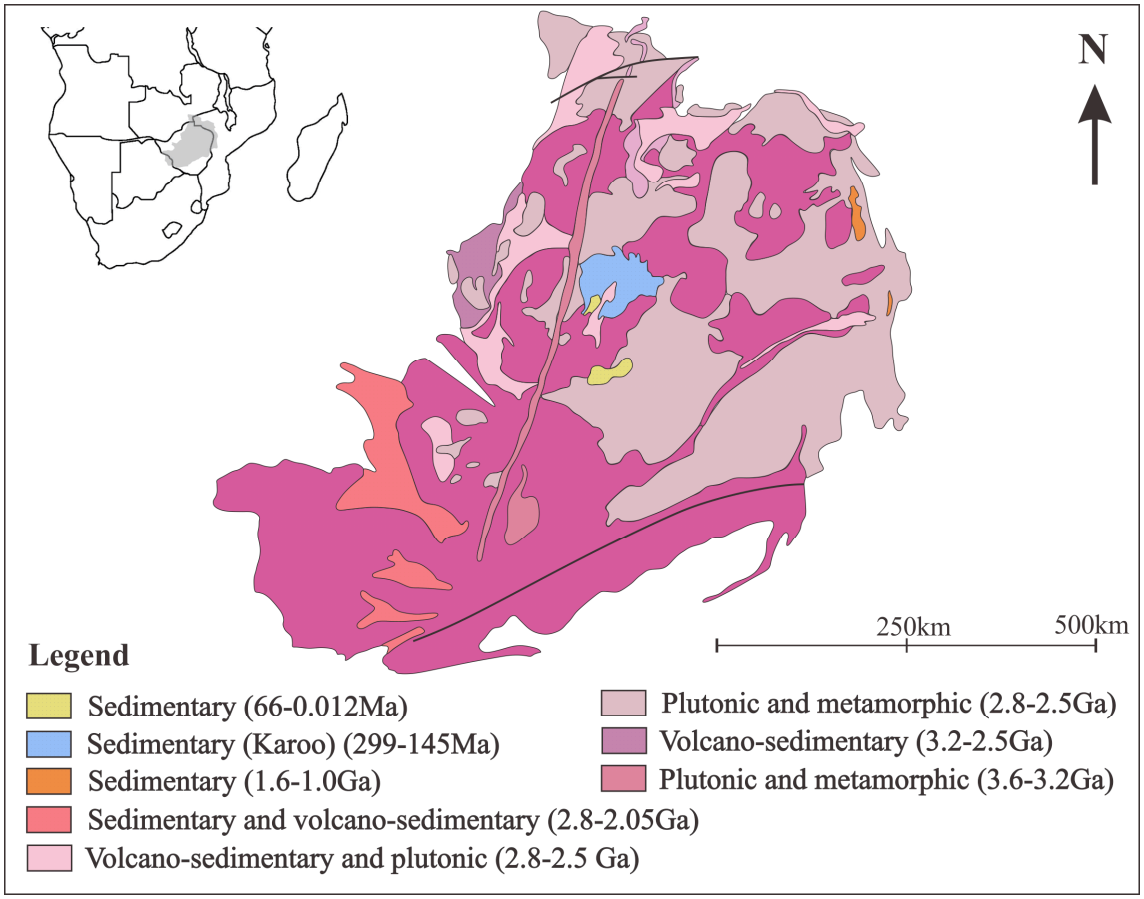

Figure 3.3. Geological map of the Zimbabwe Craton (modified from Tieblemont, 2016).

zones, the largest of which dip moderately to steeply towards the southwest and another east-west trending subvertical zone occurring in the centre of the pit. A network of smaller shears is found amongst the larger ones, including steeply northeast dipping, vertical north-south trending and occasional northeast trending shears, which dip to the northwest or southeast.

3.2.2. Strength properties of intact rock

All material types were considered to be isotropic, having identical mechanical properties in all directions, thus acting uniformly when subjected to stress. All materials were specified to be plastic in nature in order for their strength properties to be employed in the analysis of stresses and displacements in the event of failure. Furthermore, identical peak and residual strength properties (tensile strength, friction angle, cohesion) were used so as to define an elastic-perfectly plastic material where the rock mass continues to deform while keeping its strength and not changing its volume (Hoek and Brown, 1997). The use of a disturbance factor of $D = 0.7$ or higher results in post-failure strength and modulus reduction, thus making this model viable when better quality hard rock masses are experienced (Hoek, n.d.). Solutions from elastic-perfectly plastic

stress-strain relations can be comparable to those of the conventional limit equilibrium methods and the elastic perfectly-plastic model is the most common model used in the calculation of safety factors in the FEM (Zheng et al., 2005). In order to simulate the behaviour of rock masses, it is important to determine reliable estimates of rock mass properties and discontinuity properties (Ulusay, 2013). The elastic properties were defined by Young's Modulus (E_m) and Poisson's Ratio (v). Due to the limited availability of data, estimates of these parameters were based upon typical values from practical problems addressed by Hoek and Brown (1997). Values of 42 GPa and 0.2 for E_m and v respectively were employed in this study. The selection of these values relate to the Geological Strength Indices (GSI) of 67, 70 and 62 for tonalite, metagabbro and dolerite respectively which were calculated by Consultant B (2006) (Table 3.2). These values correspond to the 'very good quality' hard rock mass category defined by Hoek and Brown (1997) (Table 3.1).

Table 3.1. Typical properties of varying rock mass quality (Hoek and Brown, 1997).

	σ_{ci} (MPa)	m_i	GSI	φ' (°)	c' (MPa)	σ_{cm} (MPa)	σ_{tm} (MPa)	E_m (GPa)	v
Very good quality	150	25	**75**	46	13	64.8	-0.9	**42**	**0.2**
Average quality	80	12	55	33	3.5	13	-0.15	9	0.25
Very poor	20	8	30	24	0.55	1.7	-0.01	1.4	0.3

The strength of jointed rock masses were estimated using the Generalized Hoek-Brown strength criterion (Hoek and Brown, 1980a) which relied upon the uniaxial compressive strength (σ_{ci}) values obtained from consultant B (2006), m_i constants of intact rock from consultant C (2009) as well as the Geological Strength Index (GSI) and disturbance factor (D) of the rock mass from Consultant C (2009). Triaxial testing was conducted on metagabbro and tonalite samples during the year 1996 and 2005 by consultants A (1996) and B (2006) respectively. The triaxial test results (Appendix B, Table 1) were imported into RocData 5.0 (Rocscience Inc., 2015) in order to obtain representative and reliable estimates of rock mass strength parameters pertaining to the Generalized Hoek-Brown strength criterion (Hoek et al., 2002), and equivalent Mohr-Coulomb strength criteria parameters. The minor principal stress (σ_3) and major principal stress (σ_1) values resulted in intact uniaxial compressive strengths (σ_{ci}) of 299.15 MPa and 214.05 MPa and m_i constants of 11.07 and 33.6 for metagabbro and tonalite respectively (Table 3.3). A D value of 1, as suggested by consultant B (2006), was used and corresponds to a 'disturbed' rock mass which may be attributable to blast damage and stress relief from overburden rock removal (Hoek and Brown, 1988). These parameters were derived by performing a curve fit of the laboratory data using the Modified Cuckoo fitting algorithm (Walton et al., 2011). This algorithm

Table 3.2. Rock Mass Rating (RMR) and Geological Strength Index (GSI) values (Consultant B, 2006).

Parameter	**Tonalite** (country rock)		**Metagabbro** (ore body)		**Dolerite**		**Brittle shears (metagabbro)**		**QF Intrusions**	
	Value	Rating	Value	Rating	Value	Rating	Value	Rating	Value	Rating
Intact strength (MPa)	231	12	308	15	145	12	308	15	178	7
RQD (%)	88	17	83	17	85	17	79	17	91	20
Spacing (m)	0.48	8	0.22	8	0.20	8	0.22	8	0.35	8
Joint condition	Slightly rough, separation < 1mm, slightly weathered	25	Slightly rough, separation < 1mm, slightly weathered	25	Slightly rough, separation < 1mm, slightly weathered	25	Slickensided or gouge or < 5mm, separation 1-5mm, continuous	10	Slightly rough, separation < 1mm, slightly weathered	25
Groundwater	Dry	15	Dry	15	Dry	10	Dry	15	Dry	15
Initial RMR89	77		80		72		65		75	
Orientation adjustment	Slope favourable	-5	Slope favourable	-5	Slope favourable	-5	Slope favourable	-5	Slope favourable	-5
Final RMR	72		75		67		60		70	
GSI	67		70		62		55		65	

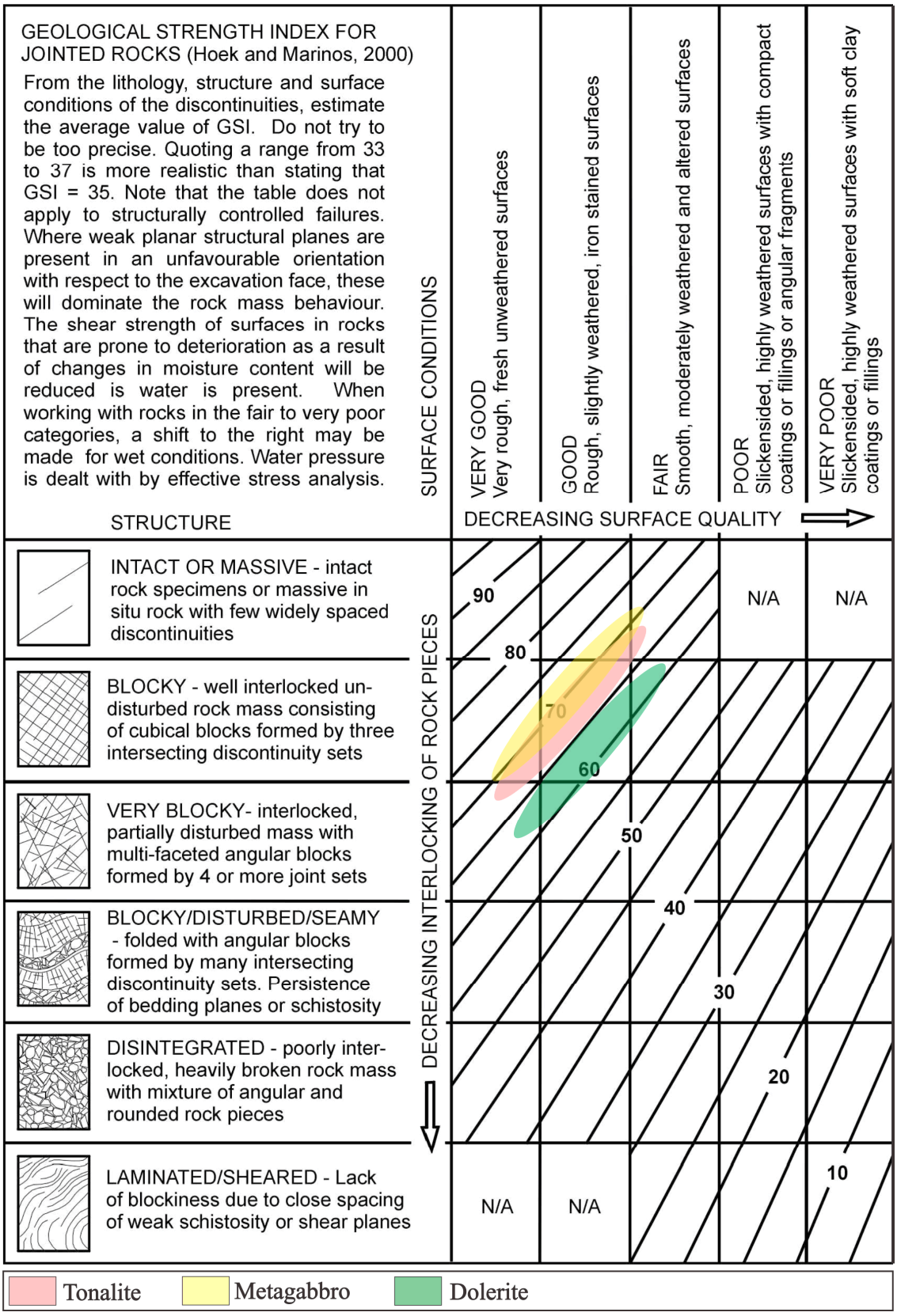

Figure 3.4. Geological Strength Index values characterizing blocky rock masses on the basis of particle interlocking and discontinuity condition (Hoek and Marinos, 2000).

is used in the calculation of residuals or errors which gives an indication of how well the selected strength criterion fits the triaxial test data set. The resulting residuals for Metagabbro and Tonalite were 52 295 and 24 242 respectively. Based on σ_{ci}, GSI, m_i and D input values, the Hoek-Brown criterion strength properties *mb*, *s* and *a* were computed (Table 3.3). Equivalent Mohr-Coulomb values for cohesion (c) and friction angle (ϕ) were calculated simultaneously (Table 3.3). The resulting rock mass properties were employed in the LEM and numerical analyses.

The GSI values were estimated directly from RMR (Bieniawski, 1989) values (Equation 4) by Consultant B (2006). The Mohr-Coulomb best-fit envelope was generated in RocData (Rocscience Inc., 2015) based on a defined stress range, which was in turn dependent on the field of application; in this case, slopes with a height of 200 m and an average material unit weight, γ, of 0.028 MN/m^3 (Table 3.3). Rock mass parameters were also calculated and include the tensile strength (σ_t), uniaxial compressive strength (σ_c) and the global strength (σ_{cm}) (Table 3.3). The principal stress (σ_1 vs. σ_3) and the shear-normal (τ vs. σ_n) failure envelopes were plotted automatically in order to observe the effects of strength parameters on the shape of failure envelopes (Figure 3.5).

Table 3.3. Rock mass strength properties.

	Parameters	Metagabbro	Tonalite	Dolerite
Hoek-Brown classification	σ_{ci} (MPa)	299.15	214.05	145
	GSI	70	67	62
	m_i	11.07	33.6	16
	D	1	1	1
Hoek-Brown Criterion	m_b	1.30	3.18	1.06
	s	0.0067	0.0041	0.0018
	a	0.50	0.50	0.50
Failure envelope range	Application	Slopes	Slopes	Slopes
	σ_{3max} (MPa)	4.82	4.84	4.45
	γ (MN/m^3)	0.028	0.028	0.028
	Slope height (m)	200	200	200
Mohr-Coulomb fit	c (MPa)	4.24	2.84	1.73
	φ (°)	49.19	55.23	44.00
Rock mass parameters	σ_t	-1.55	-0.27	-0.24
	σ_c	24.39	13.56	6.02
	σ_{cm} (MPa)	48.47	51.54	20.16

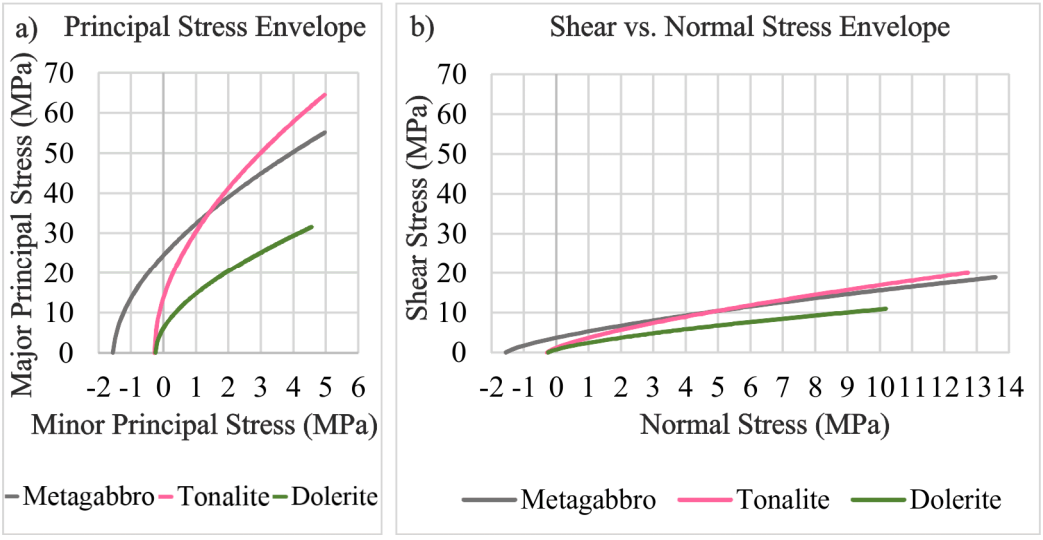

Figure 3.5. Principal stress and shear-normal failure envelopes for metagabbro, tonalite and dolerite.

3.2.3. Shear strength of discontinuities

Input data pertaining to the shear strength of failure surfaces include the selection of the preferred joint shear strength model and the associated properties. Throughout this study, the Mohr-Coulomb shear strength model or slip criterion was employed, with the friction angle (ϕ_{joint}) and cohesion (c_{joint}) being the input parameters. Consultant C (2009) determined basic friction angles (ϕ_b) of metagabbro and dolerite by performing shear tests on saw cut samples. Instantaneous friction (ϕ_i) and c_{joint} values were determined using the Barton-Bandis (Barton, 1973; Barton, 1976) equation (equation 17), which rely on normal statistical distributions for Joint Roughness Coefficients (*JRC*) (based on typical roughness profiles, Figure 2.5) and basic friction angles (ϕ_b), as well as average values of Joint Compressive Strength (*JCS*), normal stress (σ_n) and unit weight (γ) (Appendix B, Table 1). The average of the combined data was subsequently used in the Monte-Carlo simulation risk analysis program called @Risk (Palisade, 1997) to obtain statistical ranges of friction and cohesion values. The resulting mean friction angle of 48.82° and cohesion of 0.0145 MPa were used for all discontinuities throughout this study. The only specified driving force acting on the slope was gravity. The effect of water pressure on stability was not considered in this study since Consultant D (2011) noted that the majority of discontinuities in the pit were dry. Data relating to groundwater conditions were also unavailable, hence all models were assumed to be dry.

Discontinuity properties such as roughness, infilling material and persistence can greatly influence the stability or instability of slopes (Giani, 1992). Microscale and macroscale roughness

characteristics were estimated for all joints across the pit shell by Consultant D (2011). Microscale roughness characteristics were considered to be of a sample length of 200 mm from which the Joint Roughness Coefficient (JRC) was determined using typical joint profiles prescribed by Barton (1987) (Figure 2.5). Macroscale roughness in contrast was estimated on a scale starting from approximately 3 m to 10 m.

The microscale roughnesses of most discontinuities in profiles A, B and C are undulating rough, undulating smooth and undulating smooth again, respectively (Figure 3.6). The macroscale roughnesses of most discontinuities in profiles A, B and C are planar, undulating and planar, respectively (Figure 3.6).

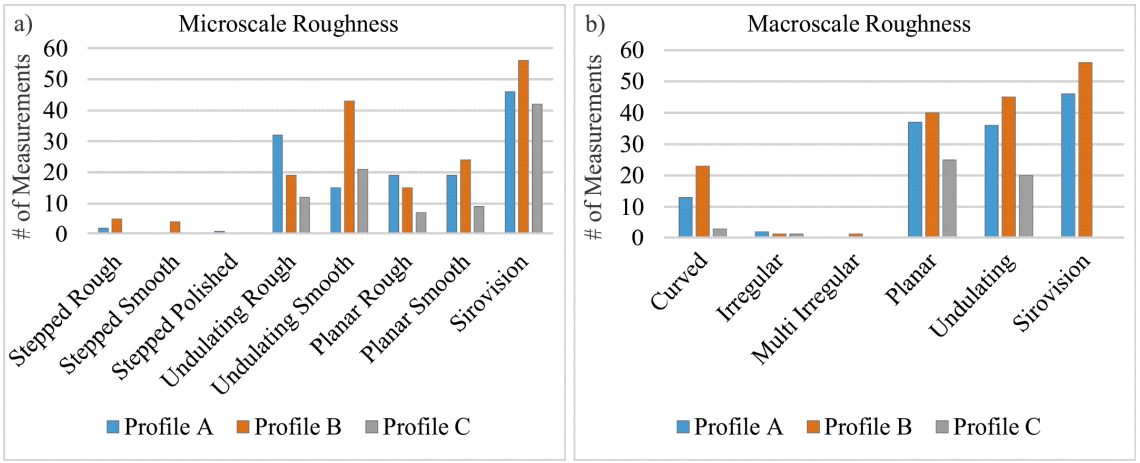

Figure 3.6. Microscale and macroscale roughness of discontinuities.

The type of infilling material within a discontinuity can also have an impact on slope stability by influencing the shear strengths of discontinuities. According to Figure 3.7, most discontinuities in profiles A, B and C have no infilling material followed by 15, 30 and 14 discontinuities in section A, B and C respectively having calcite as the infilling material. It should be noted that the majority of data have either no information of the infilling type (Sirovision data) or no information was recorded during field investigations.

The discontinuity persistences of the two mean critical joint sets associated with profiles A, B and C are shown in Figure 3.8a, b and c. In joint set 1 of profile A, most discontinuities have a persistence ranging between 10 m and 20 m thus giving a mean value of 10 m, a relative minimum of 9.5 m and a relative maximum of 10 m. The same relationship is apparent for joint set 3 (Figure 3.8a). In joint set 1 of profile B, most discontinuities have a persistence ranging from 3 m to 10 m resulting in a mean value of 6.5 m and a relative minimum and maximum value of 3.5 m. The majority of joints in joint set 2 have a persistence ranging from 1 m to 10 m resulting in a mean

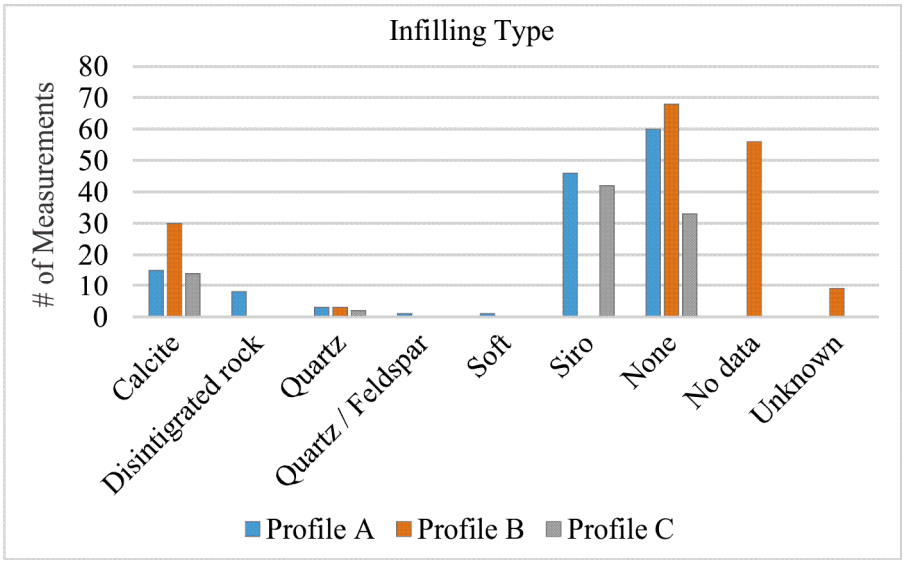

Figure 3.7. Discontinuity infilling material for profiles A, B and C.

value of 4.5 m, a relative minimum of 3.5 m and a relative maximum of 5.5 m (Figure 3.8b). Discontinuities of joint set 1 in section C have a persistence ranging from 3 m to 10 m thus giving a mean value of 6.5 m and a relative minimum and maximum value of 3.5 m. For joint set 2 however, most discontinuities ranged in persistence from 1 m to 3 m which gave a mean persistence of 2 m and a relative minimum and maximum value of 1 m (Figure 3.8c). These values were employed as input parameters for the joint network models.

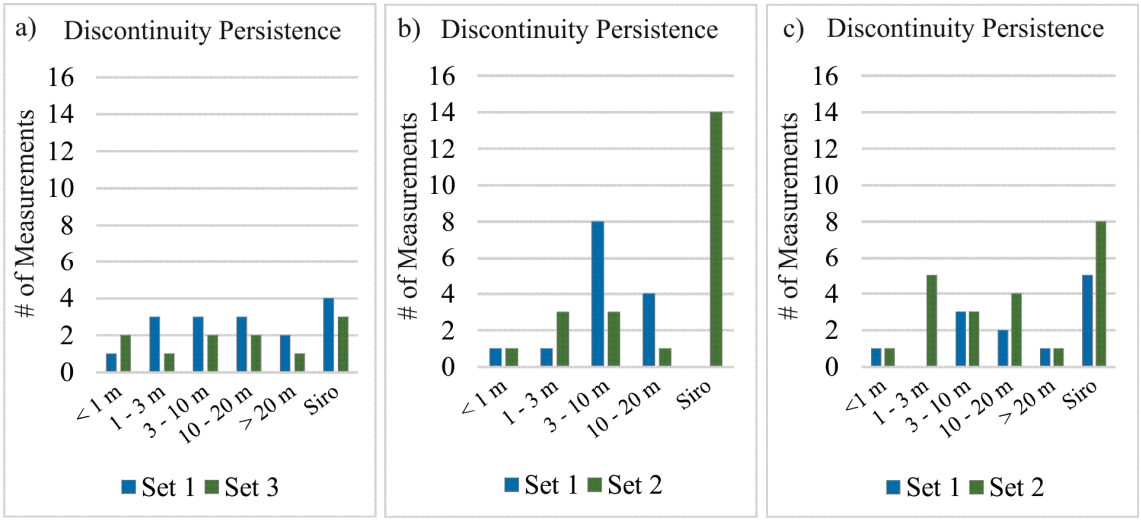

Figure 3.8. Discontinuity persistence of critical mean discontinuity sets for a) Profile A, b) Profile B and c) Profile C.

3.2.4. Joint network models

The issue of epistemic uncertainty surfaces in the numerical modelling of discontinuum media, in the case of describing discontinuities. Site characterization uncertainties regarding joints has resulted in the inability to confidently designate specific joints to numerical models. In view of structural data uncertainty, joints were instead incorporated into these models in the form of joint network models in the Finite Element Method (FEM), and Ubiquitous joints in the Finite Difference Method (FDM).

The Parallel Deterministic joint network in Phase2 (Rocscience Inc., 2015) defines discontinuities as a network of parallel joints where the spacing, orientation and length were assumed to be constant. The joint orientations were based on unstable joint sets found in the kinematic analysis where only those responsible for plane and wedge failure were incorporated into the numerical models. The two-dimensional joint spacing was taken to be 5 m and the position of the initial location of the joint network was generated randomly. Results were reported as discontinuities being of infinite and finite length. Joints of infinite length extended continuously across profiles, whereas those of finite length employed the length and persistence as detailed in Table 3.4, thereby introducing rock bridges into the models. The joint persistence in the model refers to the length of intact material, or a rock bridge, between each joint segment. The persistence was defined as 0.8 (Table 3.4) thus defining approximately 80% of joint continuity and making it comparable to the Ubiquitous Joint network employed in FLAC (Itasca, 2011). The length values employed were based on mean values of predetermined discontinuity persistence (Figure 3.8a, b and c). The joint end conditions were specified to be open at the external boundaries in order for two opposite joint faces to freely slip relative to one another at exposed faces (Hammah and Yacoub, 2009).

The Veneziano joint network was employed to introduce more random and thus more realistic joint conditions since it is based on the Poisson line process (Dershowitz, 1985), which defines random locations for joints and assumes that the joints pass through each of these locations. Joint lengths were defined as random variables based on an exponential distribution, where the distribution parameters were again based on the predetermined discontinuity mean, relative minimum and relative maximum values of each section (Table 3.4). The length persistence was defined as a random variable of exponential distribution, having a mean value of 0.5 and relative minimum and maximum values of 0.3 (Table 3.4). The degree of jointing, known as the joint intensity, was measured as the sum of squared joint trace lengths per unit area. The code associated with the dimensionless measure is P4 (Table 3.4). The Fisher K value (Fisher, 1953) is a measure of the density of a cluster of orientation data, where a larger K-value suggests a

confinement of data in a small area as opposed to a K-value of zero, which implies a uniform distribution across the stereonet (Fisher, 1953). A default Fisher K value of 5 was used for all joint sets (Table 3.4).

A plasticity model in FLAC (Itasca, 2011) known as the Ubiquitous joint model was used to represent joints in the FDM. The strength properties of the intact material and discontinuities were those associated with the Mohr-Coulomb failure and slip criterion, being the friction angle and cohesion. The joint angles employed include the mean sets determined to be the cause of potential planar and wedge instability in the kinematic analysis. The joint angles added to the models were applied anticlockwise from the x-axis.

It is important to acknowledge that the quantity and quality of data forming a geotechnical model can have major impacts on slope stability analysis results (Fillion and Hadjigeorgiou, 2015). Parameter uncertainty is thus an important consideration in this study since statistical ranges of strength properties are estimated, based on values obtained from the imprecise transformation of intact to rock mass parameters.

3.3. Kinematic analysis

Geological orientation data were analysed using Dips (Rocscience Inc., 2015), which allows users to examine structural data via stereographic projections. These analyses were performed using the lower hemisphere stereographical projection method as detailed by Hoek and Bray (1981) and Goodman (1989). This program was used to investigate potential rock slope stability failure modes including planar sliding, wedge sliding, flexural toppling and direct toppling. Apart from the selection of the failure mode, the slope orientation, friction angle and lateral limits were also specified. The slope orientations for profiles A, B and C were 133˚, 81˚ and 230˚ respectively (Table 3.5), whereas the friction angle and lateral limits for all sections were 35˚ and 20˚ respectively (Consultant D, 2011). The orientation columns in the data file were interpreted as dip and dip direction values and the declination remained at zero, as it was assumed that all measurements were recorded by considering this adjustment (Consultant D, 2011). Windows were drawn around data clusters of pole vectors and contour plots to obtain mean orientations (Table 3.5). These were then plotted as both poles and planes and were subsequently employed in the kinematic analysis. This analysis was carried out for both the overall slope angle of 57°, as well as for the stack angle of 76°, as described by Consultant D (2011). The kinematic analysis overlays for the respective failure modes were subsequently displayed on the stereonet in order to investigate whether or not failure is kinematically feasible.

Table 3.4. Joint network properties employed in Phase2.

	Profile A		Profile B		Profile C	
	J1	**J2**	**J1**	**J2**	**J1**	**J2**
Orientation definition						
Joint method	Fisher	Fisher	Fisher	Fisher	Fisher	Fisher
Trace plane dip direction (°)	0	0	0	0	0	0
Mean dip (°)	81	57	56	44	53	87
Mean dip direction (°)	031	128	010	070	298	009
Fisher K	5	5	5	5	5	5
Joint length						
Mean	10	10	6.5	4.5	6.5	2
Distribution	Exponential	Exponential	Exponential	Exponential	Exponential	Exponential
Rel. min (m)	9.5	9.5	3.5	3.5	3.5	1
Rel. max (m)	10	10	3.5	5.5	3.5	1
Length Persistence						
Mean	0.5	0.5	0.5	0.5	0.5	0.5
Distribution	Exponential	Exponential	Exponential	Exponential	Exponential	Exponential
Rel. Min	0.3	0.3	0.3	0.3	0.3	0.3
Rel. Max	0.3	0.3	0.3	0.3	0.3	0.3
Joint intensity measure						
Intensity type	P4	P4	P4	P4	P4	P4
Value	0.5	0.5	0.5	0.5	0.5	0.5
Joint end condition						
Joint ends	Open at boundary contacts	Open at boundary contacts	Open at boundary contacts	Open at boundary contacts	Open at boundary contacts	Open at boundary contacts
Open at surface contact	Yes	Yes	Yes	Yes	Yes	Yes
Open at excavation contact	Yes	Yes	Yes	Yes	Yes	Yes

	Profile A		Profile B		Profile C	
	J1	**J3**	**J1**		**J1**	**J3**
Persistence	0.8	0.8	0.8	0.8	0.8	0.8
Trace plane	No	No	No	No	No	No
Inclination	-81	-57	-56	-44	53	87

Table 3.5. Discontinuity set measurements for critical sections.

	Set	Mean dip	Mean Dip Direction	Window dip range	Window dip direction range	Slope face dip direction
Section A-A'	J1	81°	031°	66-90° & 90-82°	044-018° & 198-224°	133°
	J2	83°	305°	64-90° & 90-80°	321-284° & 104-140°	133°
	J3	58°	128°	41°-72°	116°-140°	133°
Section B-B'	J1	56°	010°	41°-70°	031°-347°	081°
	J2	44°	070°	32°-61°	114°-037°	081°
	J3	85°	284°	71-90° & 90-78°	294-264° & 084-114°	081°
	J4	85°	052°	74-90° & 90-83°	084-020° & 200-264°	081°
	J5	69°	235°	58°-82°	210°-260°	081°
Section C-C'	J1	53°	298°	42°-62°	270°-329°	230°
	J2	87°	009°	74-90° & 90-76°	031-346° & 166-211°	230°
	J3	06°	296°	0-15	15-206	230

The combined data employed in the kinematic analysis were obtained by Consultant C (2009) and D (2011). The data comprised details on the feature type, dip and dip direction, persistence, roughness, aperture and infilling. Discontinuity orientation measurements were also collected from Sirovision 3-dimensional photographs for areas which were not easily or safely accessible. Hand measurements took place at 5 different faces located throughout the entire pit, whereas Sirovision measurements were taken at three of these faces, and an additional two elsewhere in the pit (Figure 3.2).

The types of features measured by consultant D (2011) included shear zones, mylonite zones, normal faults, dykes, contacts, veins (pegmatite) and joints; the total number of each collected was 87, 8, 50, 28, 3, 65 and 562 respectively. The major discontinuities were selected based on their level of influence, which were considered to be joints, with a persistence exceeding 3 m, as well as major structures, including shears, dykes, veins and faults. With such filters, there are 86 shear zones, 8 mylonite zones, 50 normal faults, 28 dykes, 3 contacts, 63 veins, 191 joints and 54 Sirovision measurements (Figure 3.9). The 5 main discontinuity sets identified by consultant D (2011) were based on measurements across the entire pit shell and were further employed in a rockfall hazard analysis (Table 3.7). The major discontinuity sets in this study, however, were based on discontinuity measurements of 3 of the 9 mapping areas in which the 3 critical profiles were selected. This was attributable to the potential overshadowing effect by the larger quantity and variability of discontinuity measurements. Set windows were drawn, based on pole and contour plots, and their mean orientations (Table 3.5) were plotted as both poles and planes.

3.4. Limit equilibrium analysis

Both deterministic and probabilistic limit equilibrium analyses were conducted in which the safety factors and probabilities of failure were computed respectively. These computations took place using standard Rocscience Suite programmes (Rocscience Inc., 2015) for structurally controlled and non-structurally controlled failure modes.

3.4.1. Deterministic analysis

For the deterministic analysis of plane, wedge and toppling failure modes, input parameters relating to the geometry of the slope and failure surface were specified, and include slope dip and dip direction, slope height (*H*), failure plane dip and dip direction, upper face angle, and bench width, and the toppling joint spacing and overall base inclination in the case of toppling failure. The slope design, as stipulated by Consultant D (2011), comprised a stack of four 10 m vertical

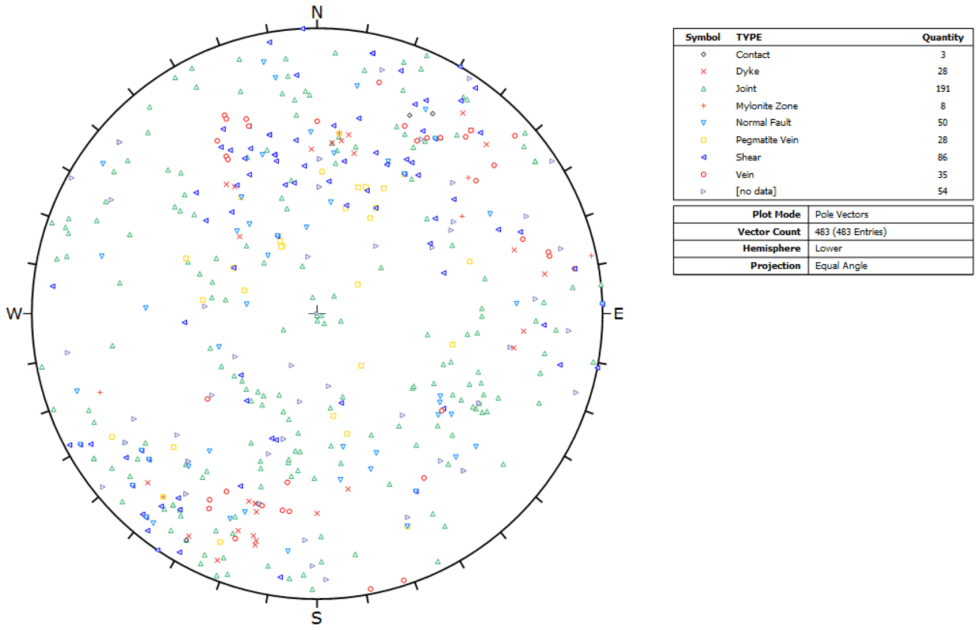

Figure 3.9. Persistent and most influential discontinuities present throughout the pit.

benches with 2.5 m step-offs between each bench and a 15 m wide catchment berm between each stack of four benches. A stack angle of 76˚ and overall slope angle of roughly 58˚ was produced from the 40 m high stacks and 200 m deep pit (Figure 3.10.). The ramp width is 25 m. The slope angle represents the inclination of the slope, which was specified as either 58˚ or 76˚. The slope height refers to the vertical distance from the crest to the toe of the slope. The slope height was again specified to be 200 m or 40 m. The failure plane angle refers to the dip of the sliding plane or the critical joint set angle whereas the upper face angle is the dip of the upper face of the slope, which was estimated to be flat hence using 0˚. The bench width is the horizontal distance from the crest forming the planar wedge to the contact point of the slope, which was 15 m. The unit weight (γ) of the rock mass was also specified in order to calculate the total weight of a planar wedge. A γ-value of 28 kN/m^3 was used for all models and all geological materials throughout the study as given by Consultant D (2011).

The Mohr-Coulomb shear strength model was employed to represent the shear strength of failure surfaces. Consultant D (2011) made use of the Monte-Carlo simulation risk analysis program @Risk (Palisade, 1997) to obtain a statistical range of these two parameters. The resulting values are shown in Table 3.6

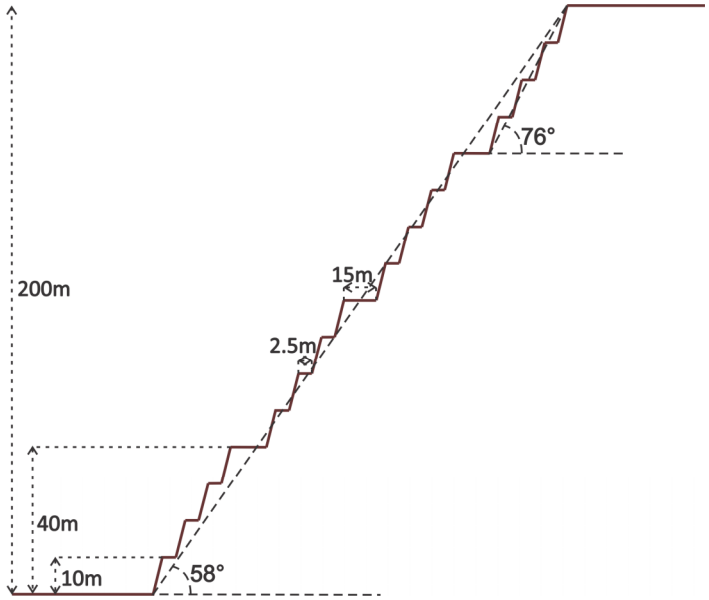

Figure 3.10. Current pit slope configuration.

3.4.2. Probabilistic analysis

Probabilistic analyses were conducted to determine the Probability of Failure (PoF) in which the uncertainties of input parameters are accounted for by entering statistical data. The sampling method selected was the Monte Carlo technique in which random numbers are sampled from the input data probability distributions. A total of 10 000 values of each input datum random variable was produced in accordance with this sampling technique and the preferred statistical distribution. Normal statistical distributions were employed for the selected random variables for all analyses. The distribution parameters defined in the probability analyses were the mean, standard deviation, and relative minimum and maximum values (Table 3.6). The design safety factor is used as a failure threshold value for post-processing of the probability of failure. This value remained as the default value of one.

Table 3.6. Deterministic and probabilistic LEM input parameters.

	Mean	Standard deviation	Minimum	Maximum
Slope height (m)	200 and 40	-	-	-
Slope face angle (°)	58 and 76	-	-	-
Unit weight (MN/m^3)	0.0275	-	-	-
Upper face angle (°)	0	-	-	-
Bench width (m)	15	-	-	-
Cohesion (MPa)	0.0145	0.00441	0.00933	0.0175
Friction angle (°)	43.823	3.155	11.810	12.047

The input parameters defined as random variables in this study included the discontinuity dip and dip direction, cohesion and friction angle, and toppling joint spacing. All failure plane dip and dip directions had a standard deviation, relative minimum and relative maximum of 2˚, 5˚ and 5˚ respectively and toppling joint spacing of 2 m, 4 m and 5 m for the standard deviation, relative minimum and relative maximum values respectively. When assessing wedge instability, a correlation coefficient between the cohesion and friction angle was defined as -0.5. This coefficient accounts for an inverse correlation between these parameters, where materials possessing low cohesion tend to have high friction angles and vice versa.

The two-dimensional limit equilibrium slope stability program, Slide (Rocscience Inc., 2015) was used in the evaluation of safety factors against circular sliding surfaces by using various vertical slice limit equilibrium methods. In this study all Slide (Rocscience Inc., 2015) models were analysed using both the Bishop simplified (Bishop, 1955) and Janbu corrected (Janbu, 1954; Janbu, 1968) methods. The convergence specifications were maintained at default values with the number of slices being 25, the tolerance being 0.005 and the maximum number of iterations being 50. The extents of the slopes were defined as external boundaries, whereas the zones separating different material properties within the external boundary were defined as material boundaries. To maintain consistency throughout all models, no phreatic surfaces or tension cracks were defined. The non-circular slip surface was specified for all models via the path search method, which produces random non-circular failure surfaces by randomly generating a slip surface starting point. This point is defined by the slope limits by automatically defining a double set of slope limit coordinate pairs, allowing for an increased accuracy in defining the initiation range for the failure surfaces. A default number of 5000 surfaces was specified for the path search options. For additional accuracy, the ‘optimize surfaces’ option was enabled which allows for the search and location of lower safety factor sliding planes by employing the surfaces generated by the path search. The material properties defined were identical to those employed in the deterministic analysis previously mentioned (Table 3.3).

3.5. Numerical modelling

3.5.1. Finite Element Method

The two-dimensional finite element analysis code, Phase2 (RS2) (Rocscience Inc., 2015) is an implicit continuum model that was employed with the Shear Strength Reduction (SSR) technique to analyse the stability of the three critical sections. The modelling or pre-processing module of Phase2 (Rocscience Inc., 2015) allowed for the building of models by introducing and adapting

the geometry of the problem domain, specifying stresses, defining material and discontinuity properties, generating the finite element mesh, and finally, specifying boundary conditions. All analyses were performed under plane strain conditions where the major and minor principal stresses (σ_1 and σ_3 respectively), out-of-plane principal stress (σ_z), and in-plane displacements and strains were calculated. The Gaussian Elimination solver type was employed in all analyses. For stress analyses, a maximum number of 500 iterations was specified and an automatic number of load steps was selected. The absolute energy convergence type was adopted. The initial estimate of the SRF was set to 1 and an automatic step size was employed. External boundaries were imported as DXF files whereas material boundaries were created manually. The initial in-situ stresses imposed on all models was the gravitational field stress which made use of the actual model ground surface to calculate the depth below it. A total stress ratio, K (horizontal: vertical in- and out-of-plane directions) of 1 was used for all analyses. The horizontal stress at the surface, also referred to as the locked-in horizontal stresses (in- and out-of-plane directions) remained as zero in all models. A uniform finite element mesh type was employed in all models which defines approximately equally sized elements throughout. The 6-noded-triangle element type was used as they incorporate mid-side nodes to enhance results. The displacement boundary conditions were specified next. Pinned conditions suggests boundaries which are unable to move in the X and Y directions and thus maintains a zero displacement during the analysis. Such conditions were applied to all external boundaries except for those representing the ground surface, which were instead characterised as free boundaries. The type of initial element loading was specified as 'Field stress and body force' where field stress refers to the stress properties previously specified in the loading properties, and body force represents the self-weight of elements which is derived from the material unit weight to be specified. The strength properties employed include the failure criterion, material type, tensile strength, friction angle and cohesion of each material present in the section. The Generalized Hoek-Brown strength criterion and associated parameters were employed in the analysis of sections without the introduction of discontinuities. Equivalent Mohr-Coulomb strength parameters however were employed in both discontinuum and continuum models. The elastic properties used, Young's Modulus (E_m) and Poisson's Ratio (ν), are those associated with good quality rock masses as seen in Table 3.1.

3.5.2. Finite Difference Method

FLAC (Itasca, 2011) was operated in menu-driven mode via the GIIC (Graphical Interface for Itasca Codes). The external and material boundaries defining the problem geometry were imported as DXF files using the 'Sketch' tool. The 'Cleanup' stage of this tool was then employed

to eliminate or merge any non-essential vertices from the sketch. Next the boundaries were copied to the geometry builder in order to construct quadrilateral zones. In the geometry builder the 'Create' stage was used to produce additional construction lines in order to partition the problem domain into several four-sided blocks which are subsequently filled with zones. The 'Cleanup' stage was again made use of to remove erroneous lines or vertices. In the 'Blocks' stage, block points were marked manually to create the four-sided blocks which then enclosed the mesh. The 'Edit' tool was employed for modifying the virtual grid. Here, the 'Boundary' stage was used to assign external automatic boundary conditions where roller and pinned conditions were applied to the sides and bottom of the virtual grid respectively. The 'Mesh' stage was subsequently used to adjust the zone density to a predefined average total number of 60 horizontal zones which by default represents a fine mesh. Once the virtual grid was created, the 'Execute' action sent the newly defined FLAC commands to FLAC (Itasca, 2011). In the case of a slightly poor aspect ratio of individual zones, additional improvements were made via the 'Shape' stage of the 'Alter' tool. Here, points were manually selected and shifted to enhance zone ratios. Material properties were then assigned to the various geological materials based on predetermined constitutive models (Table 3.3). In this study the Mohr-Coulomb and Hoek-Brown constitutive models were selected in a plastic state. Once a material was selected via a rectangular range, the properties were inserted. Thereafter, the gravitational acceleration was incorporated into the model via the 'Gravity' tool. Gravity was defined in terms of magnitude and direction angle and was specified automatically. Following the generation of the model, the 'Solve' stage of the 'Run' tool was employed to calculate a steady-state equilibrium solution which was followed by a factor of safety calculation via the 'SolveFoS' stage. FLAC variables were then superimposed to create a model plot of the calculation results. Using the 'Model' stage of the 'Plot' tool, the model boundary, factor of safety, maximum shear strain and plasticity indicators were selected from the item tree and the plots were created and exported. The overall process followed in FLAC can be seen in Figure 3.11.

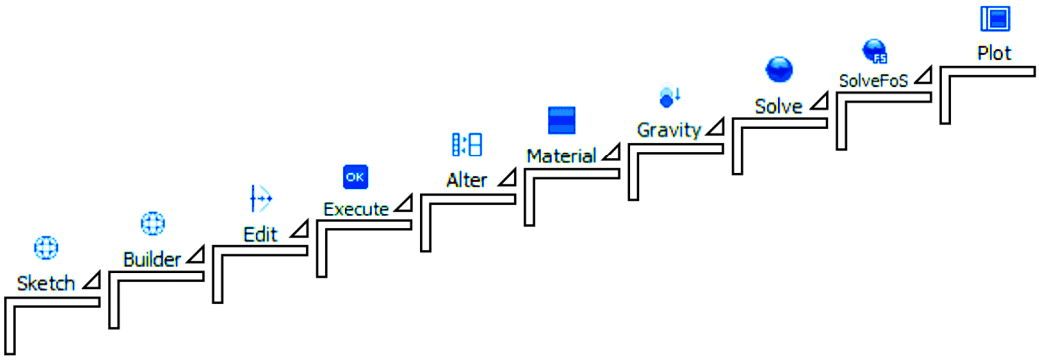

Figure 3.11. Tools and stages employed in creating and running a FLAC model.

3.6. Rockfall hazard analysis

Rockfall hazards pose an additional threat to surface mining operations. The prediction of rockfall behaviour is critical in the selection and design of effective protection measures (Hoek and Bray, 1981) thus improving safety in the mining environment. A rockfall hazard simulation study was conducted to compare a standard two-dimensional (2D) code, RocFall (Rocscience, 2015), to a three-dimensional (3D) code, Trajec3D (BasRock, 2016). Both methods were based on rigid body dynamics, where the physical interaction between materials is a function of the combined properties of the fall body and the impact surface.

RocFall (Rocscience Inc., 2015) is used in the prediction of rock fall paths. It operates by computing energies and requires a normal coefficient of restitution (R_n), tangential coefficient of restitution (R_t), dynamic friction coefficient and rolling resistance coefficient as input parameters. The trajectories may subsequently be analysed according to the bounce height (h), kinetic energy (E), velocity (V) and run-out distance. Trajec3D simulates the paths of 3D falling bodies which take on various shapes (Basson, 2012). The projected trajectories may then be analysed according to their velocity, energy and vertical displacements. It requires three input parameters, these being the coefficient of restitution (COR) and the static and dynamic friction angles. The COR represents the elasticity of the interactions between a slope and a falling body. A COR value of zero suggests a perfectly plastic impact with all the energy being absorbed by the surface, and the body coming to a complete stop upon contact. On the contrary, a value of one suggests a perfectly elastic impact, with no loss in energy and, therefore, no loss in velocity (Basson et al., 2013). In a rockfall analysis where fall bodies do not interact, the static friction angle is irrelevant and takes

on the same value as the dynamic friction angle. If, however, fall bodies are set to interact and the fall body that came is rest is impacted by another oncoming fall body, the static friction angle is important and should be specified.

The theoretical optimum geotechnical design domain comprise a stacks of four, 10 m vertical benches with 2.5 m step-offs between each bench, giving a stack angle of 76°. There is a 10 m wide catchment berm between each stack of 4 benches and the overall slope angle is approximately 58°. This represented a theoretically ideal yet unrealistic design profile (Figure 3.12a) due to effects of backbreak at the crests and underbreak at the toes of berms, which ultimately reduces berm widths. More realistic slope profiles representing stages of these processes are visible in Figure 3.12b-d ranging from good slope/cut slope topography, where the effects of backbreak and underbreak is less conspicuous, to poor slope/cut slope topography where the effects are obvious.

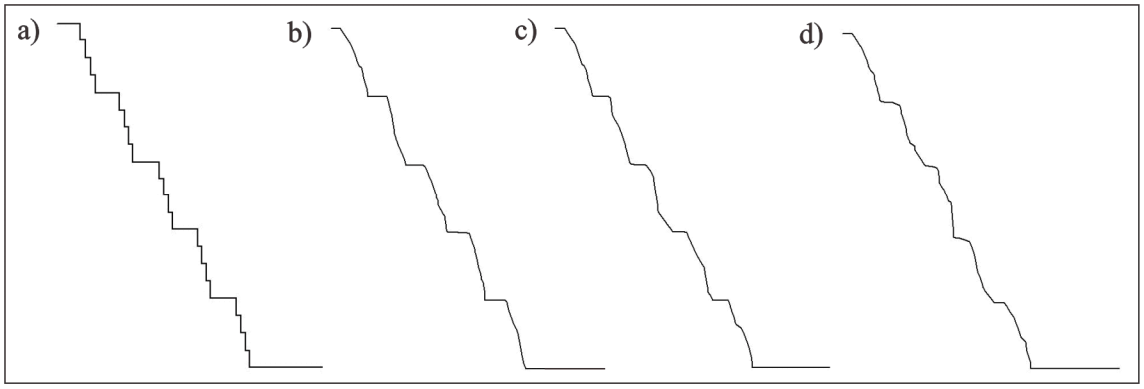

Figure 3.12. Slope profiles depicting a) theoretical design profile, b) realistic profile simulating a good slope/cut slope topography, c) realistic profile simulating a moderate slope/cut slope topography and d) realistic profile simulating a poor slope/cut slope topography.

Rockfall trajectories are affected by the shape and orientation of the falling body with respect to the slope surface (Alejano et al., 2007). Discontinuity orientation data was thus used in order to estimate probable shape and volume of rock falls. The selection of five prominent joint sets (Table 3.7) using DIPS (Rocscience Inc., 2015) was based on 483 discontinuities considered to have influential properties, such as higher persistence, as well as the major structures being shears, dykes, veins and faults (Consultant D, 2011). Discontinuity set 1 comprised the near vertical groupings of shears, faults, dykes, veins and joints which strike NW-SE, whereas those from set 2 were all joints striking WNW-ESE. Fault and joint measurements comprise discontinuity set 3, all of which strike SSW-NNE. Discontinuity set 4 included groupings from shears, faults, and

veins, which strike ENE-WSW, and lastly, set 5 was based on groupings from dyke and vein measurements which strike ESE-WNW.

Table 3.7. Mean discontinuity sets employed in the estimation of block size in rockfall analyses.

Discontinuity Set	Mean Dip (°)	Mean Dip Direction (°)	Joint spacing (m)	Angle between joint sets (°)
J1	81	036	0.3	34.65 (J1 & J2)
J2	48	024	0.3	65.37 (J2 & J3)
J3	62	303	0.3	62.63 (J3 & J4)
J4	64	156	0.3	40.86 (J4 & J5)
J5	67	201	0.3	-

Volume estimation of the falling block was based on 43 walkover inspections (Consultant D, 2011). A rating of 100 was given to 18 (42 %) of the sites which had a volume greater than 8 m^3 and diameter greater than 1 m. A further 17 (40 %) sites had a rating of 38 representing a volume ranging from 4 m^3 to 8 m^3 and a diameter ranging from 0.5 m^3 to 1 m^3. The remaining 8 sites (18 %) were given a rating of 6 which is suggestive of a block volume ranging from 2.5 m^3 to 4 m^3 and a diameter of 0.25 m to 0.5 m. Since the majority of rock block volumes from site inspections exceed 8 m^3, the mean block volume was assessed using a method proposed by Cai et al. (2004), in which the block size (V_b) is a volumetric expression of joint density, which gives an indication of the rock mass quality. According to the same authors, if three or more sets are present, the size of a falling body can be calculated using the joint spacing (S_1, S_2, S_3) and the angle between joint sets ($sin\gamma_1$, $sin\gamma_2$, $sin\gamma_3$) (Table 3.7) as follows:

$$V_b = \frac{S_1 S_2 S_3}{sin\gamma_1 sin\gamma_2 sin\gamma_3} \tag{20}$$

The average discontinuity spacing of 0.3 m was employed based on the RMR classification conducted by consultant B (2006). The resulting mean block volume was 0.059 m^3. A density of 1694.91 kg/m^3 was calculated using this value as well as a mass of 100 kg, corresponding to the minimum allowable mass in Trajec3D.

In the 2D simulation 3000 rocks were released from the same initial slope seed point. Falls from lower benches or from operational mining faces were not considered in this method, since these rocks would always reach the toe of the slope and thus should be handled via a different approach. The rolling resistance of the 2D model represents the frictional effect of the ground on the falling body (Azzoni et al., 1995). A value of 0.4 for the fresh and near vertical rock was selected based

on findings by Azzoni and de Freitas (1995) and corresponds to fresh limestone rock, whereas a value of 0.75 for the berms relates to soft debris with loose angular rock fragments and earth with some boulders. Table 3.8 shows the various R_n, R_t and dynamic friction coefficients used for benches and slope faces. In the 3D simulation, one of each fall body shape was released from each starting point. Table 3.8 shows the *COR* and static and dynamic friction angles used.

The shapes employed in the 2D and 3D simulations are shown in Table 3.9. All the 3D shapes from Trajec3D (BasRock, 2016) were employed in the models and their approximate equivalents were chosen from a list of 22 possible 2D shapes in RocFall (Rocscience Inc. 2015).

Table 3.8. Parameters used in 2D and 3D rockfall simulation codes.

Parameters		**2-D analysis**	**3-D analysis**
COR		-	0.1
Static φ (°)		-	30
Dynamic φ	Fresh rock	0.73	30°
	Berm	0.51	
R_n	Fresh rock	0.48	-
	Berm	0.36	-
R_t	Fresh rock	0.89	-
	Berm	0.77	-
Block mass (kg)		100	100
Rolling resistance	Fresh rock	0.4	-
	Berm	0.75	-

Table 3.9. 2D and 3D shapes employed in rockfall simulation.

RocFall 2-D		Trajec3D 3-D	
Sphere		Perfect sphere	
Circle		Flat cylinder	
Super ellipse^6 (1:1)		Square box	
Super ellipse^6 (1:2)		Flat box	
Super ellipse^6 (1:2)		Flat elongated box	
Octagon		Angular (rough) cylinder	
Hexagon		Angular (rough) smartie shape	
Pentagon		Angular (rough) flat cylinder	

CHAPTER FOUR
RESULTS

4.1. Kinematic analysis

Kinematic analyses were performed for each of the critical profiles to determine potential instability driven by pervasive mean discontinuity sets (Chapter 3, Table 3.5). Profile A incorporates discontinuity data collected on cut 7 north wall 1, profile B on cut 7 west wall 1 and profile C on cut 6 east wall 1. Results indicate possible planar failure in profiles A and B at both overall and stack angle levels (Figure 4.1). Wedge failure is also likely at stack angle level in profiles A, B and C and at the overall slope angle in profile B (Figure 4.1). Potential flexural toppling is seen in profile A along both overall and stack angles, and direct toppling in profiles A and B along both overall and stack angles as well (Figure 4.1).

In profile A, planar sliding is a feasible failure mechanism at both the overall slope angle as well as the stack angle since the pole vector belonging to joint set 3 (J3) lies inside the daylight envelope of the slope plane, outside the area of the cone (35˚) representing frictional stability and within the lateral limits of 20˚ (Figure 4.1). Potential wedge sliding was determined by analysing the position of the intersection of two planes. It is evident from Figure 4.1 that wedge failure is admissible at stack angle level since the intersection between joint set 1 (J1) and J3 lies within the primary critical curved zone defined by the inside of the friction cone and the outside of the slope plane. Since the intersection occurred within the primary critical zone for wedge sliding, this wedge could slide on either one plane or along both. This was determined based on methods discussed in section 2.5.4.2. With the line of intersection having a trend of 111˚, sliding will take place along J3. Flexural toppling analysis relied upon the position of the mean joint set poles rather than planes. Flexural toppling is feasible for profile A at both the overall slope and stack angle level since joint set 2 (J2) lies within the critical zone which is defined by the outside of the slip limit plane and the inside of the lateral limits (Figure 4.1). The slip limit is the difference between the slope angle and friction angle which were 23˚ and 41˚ for the overall slope and stack angle respectively. Direct toppling requires the intersection of two joint sets dipping into the slope as well as a third set which is a sliding surface known as a base plane. In profile A, an intersection between J1 and J2 represents an oblique toppling intersection which falls within the friction cone. The J3 pole plotted outside the friction cone and inside the slope face angle and lateral limits (Figure 4.1). This position represents a release or sliding plane which thus indicates the admissibility of simultaneous sliding and toppling failure.

In profile B, it is evident that planar failure is feasible at both the overall slope angle as well as the stack angle since the pole belonging to J2 is positioned within the daylight envelope, outside the friction cone and within the lateral limits (Figure 4.1). Wedge sliding is also admissible along both overall slope and stack angles, since the intersection between J1 and J2 lies within the primary critical zone defined by the inside of the friction cone and the outside of the slope plane (Figure 4.1). With the line of intersection having a trend of 064˚, sliding takes place along J2. Flexural toppling was found to be an inadmissible failure mode in profile B as opposed to direct toppling, which is seen at both overall slope and stack angle levels. Two plane intersections, J3 and J4 as well as J3 and J5, represented oblique toppling intersections, whereas the J2 pole represented a release or sliding plane that could result in the simultaneous failure by sliding and toppling.

In profile C, wedge failure at stack angle level is the admissible failure mechanism. The intersection between J1 and J2 dips into the slope and occurs in the critical primary zone thus representing a wedge which could slide along one plane or along the intersection (Figure 4.1). With the intersection having a trend of 280˚, the wedge is expected to slide along the line of intersection. Neither flexural toppling nor direct toppling is a concern for profile C (Figure 4.1).

From Figure 4.1 it is evident that wedge failure can be considered a greater threat at stack angle level and therefore steeper slope face angles, whereas planar failure could be seen as a risk for the overall pit wall stability. Toppling failure in profiles A and B could be a potential failure mechanism at both overall and stack angles.

4.2. Limit equilibrium analysis

The kinematically feasible joint sets for structurally controlled failure modes (i.e. planar, wedge and toppling) as well as non-structurally controlled failure modes (i.e. circular) were analysed using the LEM to determine safety factors and probabilities of failure. For structurally controlled failure modes the FoS and PoF were determined for each of the mean joint sets according to the failure modes detected in the kinematic analyses. The slope angle and height input parameters were identical to those employed in the kinematic analyses where the overall slope angle of 58˚ is accompanied by a slope height of 200 m, and a stack angle of 76˚ with a slope height of 40 m (Chapter 3, Table 3.6). Material strength properties used are those seen in Table 3.3 (Chapter 3).

The critical joint set responsible for planar failure in profile A is J3 and is associated with safety factors of 0.93 and 0.72 at 58° and 76° respectively (Table 4.1). Similarly, wedge failure is a possibility at stack angle level, having a safety factor of 0.77 (Table 4.1). The RocTopple (Version

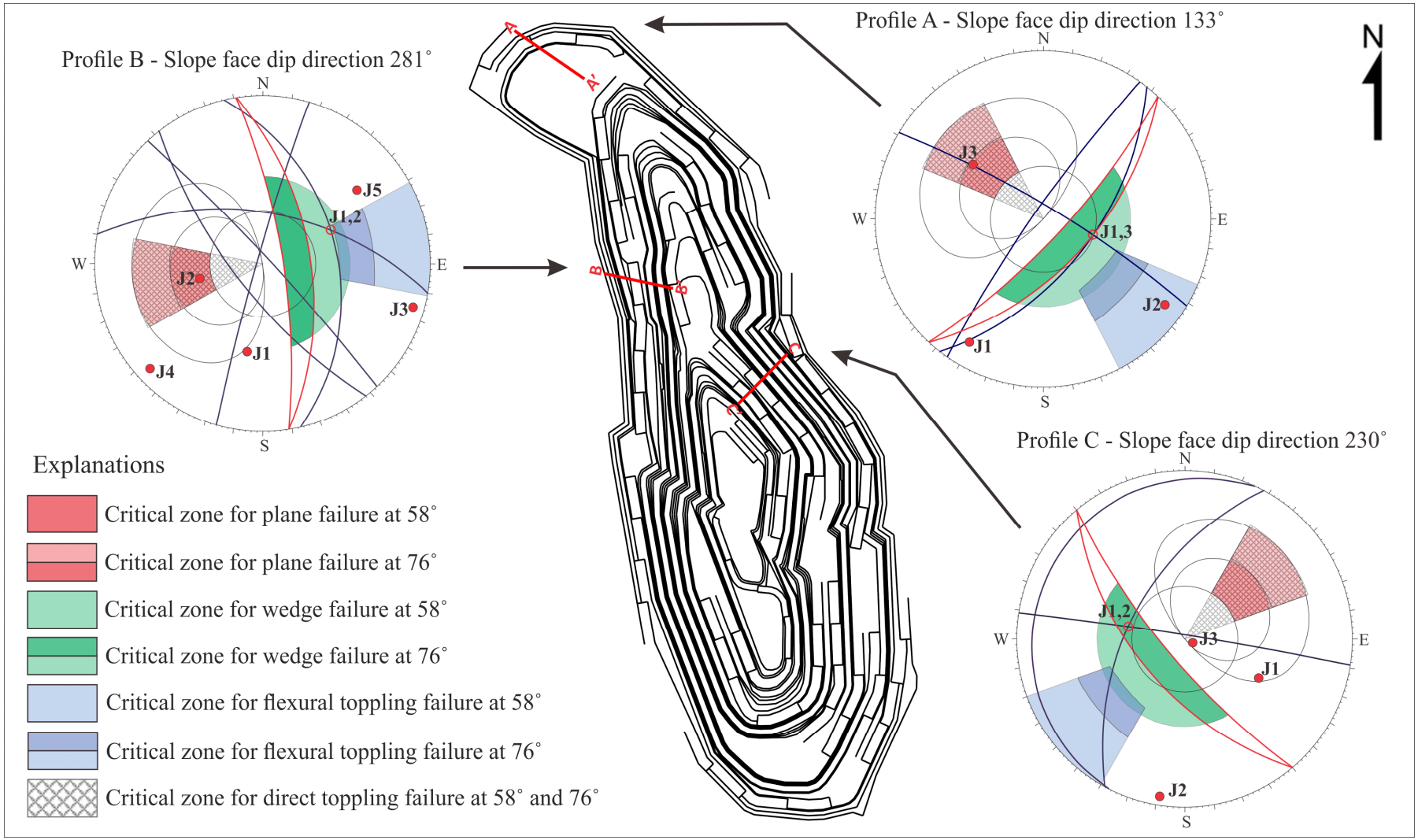

Figure 4.1. Kinematic analysis for thee critical profiles along overall slope angle and stack angle levels.

1.004, Rocscience Inc., 2015) program employed only allows for the limit equilibrium analysis of direct or block toppling analysis as defined by Goodman and Bray (1976) and does not perform flexural toppling analysis. According to the analysis, direct toppling is less likely in profile A, having greater safety factors and low probabilities of failure. With a slope face angle of 58˚, height of 200 m and toppling joint spacing of 5 m, there is a 0.70 % probability of failure whereas at a stack angle of 76˚ and height of 40 m, there is a 4.10 % probability of failure (Table 4.1). Both models shows that the direct toppling mode of failure would be through sliding.

Table 4.1 Deterministic and probabilistic LEM results for Profile A.

Overall slope angle (58°)				Stack angle (76°)			
Type	Joint set	FoS	PoF (%)	Type	Joint set	FoS	PoF (%)
Planar	J3	0.93	n/a	Planar	J3	0.72	n/a
Wedge	-	-	-	Wedge	J1, **J3**	0.77	n/a
Direct Toppling	J1&J2 (int.) J3 (base)	5.34	0.70	Direct Toppling	J1&J2 (int.) J3 (base)	5.11	4.10

In profile B the potential for plane failure is attributable to J2 and results are identical at overall slope angle and stack angle levels with a FoS of 1.14 and PoF of 13.86 % (Table 4.2). Although low, there is a probability of wedge failure with J1 and J2, with a FoS and PoF of 1.23 and 4.90 % respectively at both overall slope and stack angles. Direct toppling at the overall slope angle and using the J3 and J4 intersection, resulted in a FoS and PoF of 1.20 and 18.60 % respectively (Table 4.2) where toppling commences behind the crest and continues towards to the toe of the slope at which point sliding takes over. At stack angle level, a higher safety factor of 5.09 and a reduced probability of failure of 0.4 % were computed, where sliding originates behind the crest and continues until reaching the toe of the slope. When performing direct toppling analysis using the intersection between J3 and J5, and the overall slope angle, a FoS and a PoF of 1.18 and 6.10 % respectively are calculated, where the prevalent failure mode is toppling. At stack angle level however, a safety factor and a probability of failure of 2.24 and 2.20 % (Table 4.2) respectively are generated, with the mode of failure being sliding. For profile C there is a 0 % probability of wedge failure for J1 and J2 at the stack angle level, with a safety factor of 1.36.

To evaluate potential non-structurally controlled instability modes, i.e. circular failure, the LEM code Slide (Rocsience Inc., 2015) was used. Analyses were based on the Bishop Simplified and Janbu Corrected methods and the resultant safety factors placed in the range of 4.35 and 5.67, with profile B having the greatest safety factors (Table 4.3). When statistical values corresponding

Table 4.2. Deterministic and probabilistic LEM results for Profile B.

Overall slope angle (58°)				Stack angle (76°)			
Type	Joint set	FoS	PoF (%)	Type	Joint set	FoS	PoF (%)
Planar	J2	1.14	13.86	Planar	J2	1.14	13.86
Wedge	J1, **J2**	1.23	4.90	Wedge	J1, **J2**	1.23	4.90
Direct Toppling	J3&J4 (int.) J2 (base)	1.20	18.60	Direct Toppling	J3&J4 (int.) J2 (base)	5.09	0.40
Direct Toppling	J3&J5 (int.) J2 (base)	1.18	6.10	Direct Toppling	J3&J5 (int.) J2 (base)	2.24	2.20

to 10 % of strength properties are employed in probabilistic analyses, all models revealed a 0.0 % probability of circular failure. Reliability Indices (β) were calculated to evaluate the uncertainty associated with slope stability (Abbaszadeh et al., 2011), and take into account the standard deviation and mean values of the safety factors. For Generalized Hoek-Brown material parameters, average β values for profiles A, B and C were found to be 11.9, 9.1 and 13.1 respectively. For equivalent Mohr-Coulomb parameters, average β values for profiles A, B and C were 24.7, 17.6 and 23.8 respectively. The critical failure surfaces are shown in Figures 4.2-4.7.

Table 4.3. Safety factors determined using Slide with both Generalized Hoek-Brown and equivalent Mohr-Coulomb strength parameters.

	Profile A		Profile B		Profile C	
Method	M-C	G. H-B	M-C	G. H-B	M-C	G. H-B
Bishop simplified	4.49	4.78	5.26	5.23	4.64	4.35
Janbu corrected	4.90	5.11	5.67	5.56	4.89	4.37

4.3. Numerical modelling

4.3.1. Continuum media

The analysis of profile A as a continuum medium via the Generalized Hoek-Brown failure criterion (GH-B) computes safety factors in Phase2 (Rocscience Inc., 2015) and FLAC (Itasca Corp., 2011) of 4.95 and 5.06 respectively (Table 4.4). The resulting maximum shear strain contours are shown in Figure 4.2a and c. In both models, strain contours show a thin band along the dolerite dyke material boundaries. The FEM indicate that the maximum shear strain of $2.1e^{-002}$ occurs on the dolerite contact behind the uppermost bench, and in the FDM, a lower shear strain of $5.00e^{-03}$ occurs in the same position. The failure mode in the FEM involves a combination

of both shearing and tension throughout the rock mass and along the toes of the three uppermost benches (Figure 4.2b). Shearing indicators alone exist as a deep seated circular surface closely resembling that of the Slide failure surface (Figure 4.2b). Plasticity indicators in the FDM display the zones that have failed in the past (shear-p) and those that are currently in a state of failure, which also represent the size of the failure region (shear-n) (Figure 4.2d). The failure region is similar to the shearing surface produced by the FEM, but less defined (Figure 4.2d).

In profile B the safety factors obtained from the FEM and FDM were 5.53 and 6.08 respectively (Table 4.4). The strain contours for both models are presented in Figure 4.3a and c and depict a tendency of circular failure, where the failure surface in the FDM is more defined than in the FEM. In the FEM, the greatest shear strain of $5.3e^{-004}$ exists at the edge of the boundary away from the slope face as opposed to the highest value of $1.25e^{-03}$ in the FDM occurring at the toe of the slope. The plasticity indicators show that the slope will fail in shear along a failure surface similar to that calculated by Slide (Figure 4.3b, d). This failure state indicator plane is well defined in both models.

For multi-material profile C, the FEM and FDM computed safety factors of 4.30 and 5.52 respectively (Table 4.4). While there is a fairly strong agreement between the observed failure surfaces produced in both methods, there is no single clearly defined failure surface (Figure 4.4a and c). In the FEM the greatest shear strain value of $9.8e^{-004}$ occurs on the external boundary away from the slope face whereas strains reaching $1.25e^{-03}$ arise along the dolerite contact on the centre berm, and extend into the slope (Figure 4.4a). The yielded elements indicate that the failure modes involve a combination of shearing and tension taking place on benches, shearing along the dolerite intrusion, and tension along the upper central portion of the profile (Figure 4.4b, d).

When performing the same analysis, but with equivalent Mohr-Coulomb strength parameters in profile A, the safety factors generated by the FEM and FDM are 4.84 and 4.91 respectively (Table 4.4). The maximum shear strain contours are shown in Figure 4.5a and c. There is good agreement in results between the methods, where a thin band is formed at the dolerite-metagabbro contact closest to the slope face. The FEM, however, shows evidence of an indistinct failure surface resembling a circular failure surface which originates at the outermost external boundary and extends to the toe of the slope (Figure 4.5a). The greatest shear strain values of $1.8e^{-003}$ and $1.75e^{-03}$ were produced by the FEM and FDM respectively, both of which can be seen along the upper dolerite-metagabbro contact (Figure 4.5a, d). In both models, this contact indicates failure in tension from the surface to approximately 90 m into the slope, while the faint circular failure surface is due to shearing (Figure 4.5b, d).

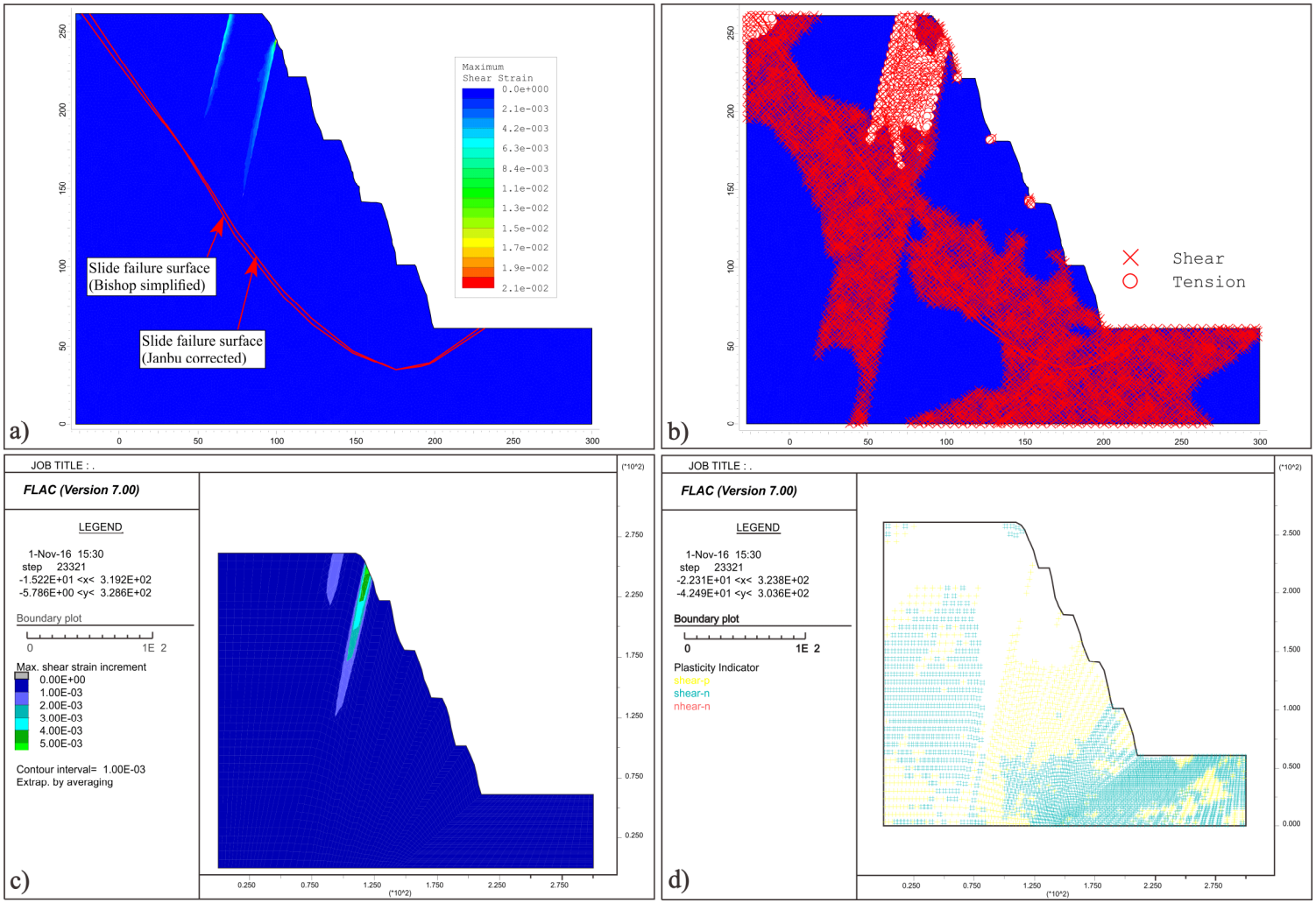

Figure 4.2. Profile A FEM results showing a) Maximum shear strain contours with Slide failure surfaces included, and b) Plasticity indicators, and FDM results showing c) maximum shear strain contours and d) Plasticity indicators, using the Generalized Hoek-Brown criterion.

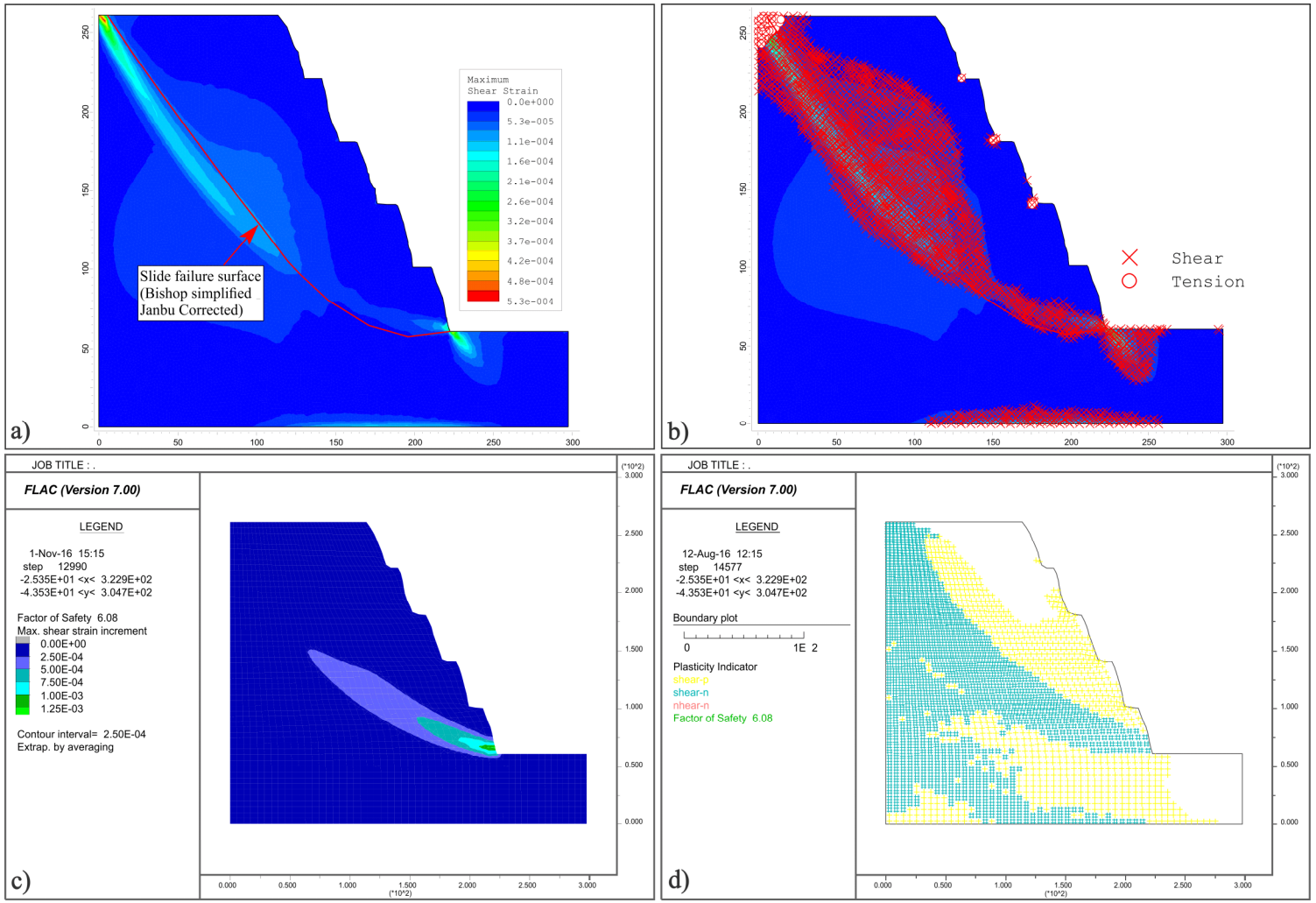

Figure 4.3. Profile B FEM results showing a) Maximum shear strain contours with Slide failure surfaces included, and b) Plasticity indicators, and FDM results showing c) maximum shear strain contours and d) Plasticity indicators, using the Generalized Hoek-Brown criterion.

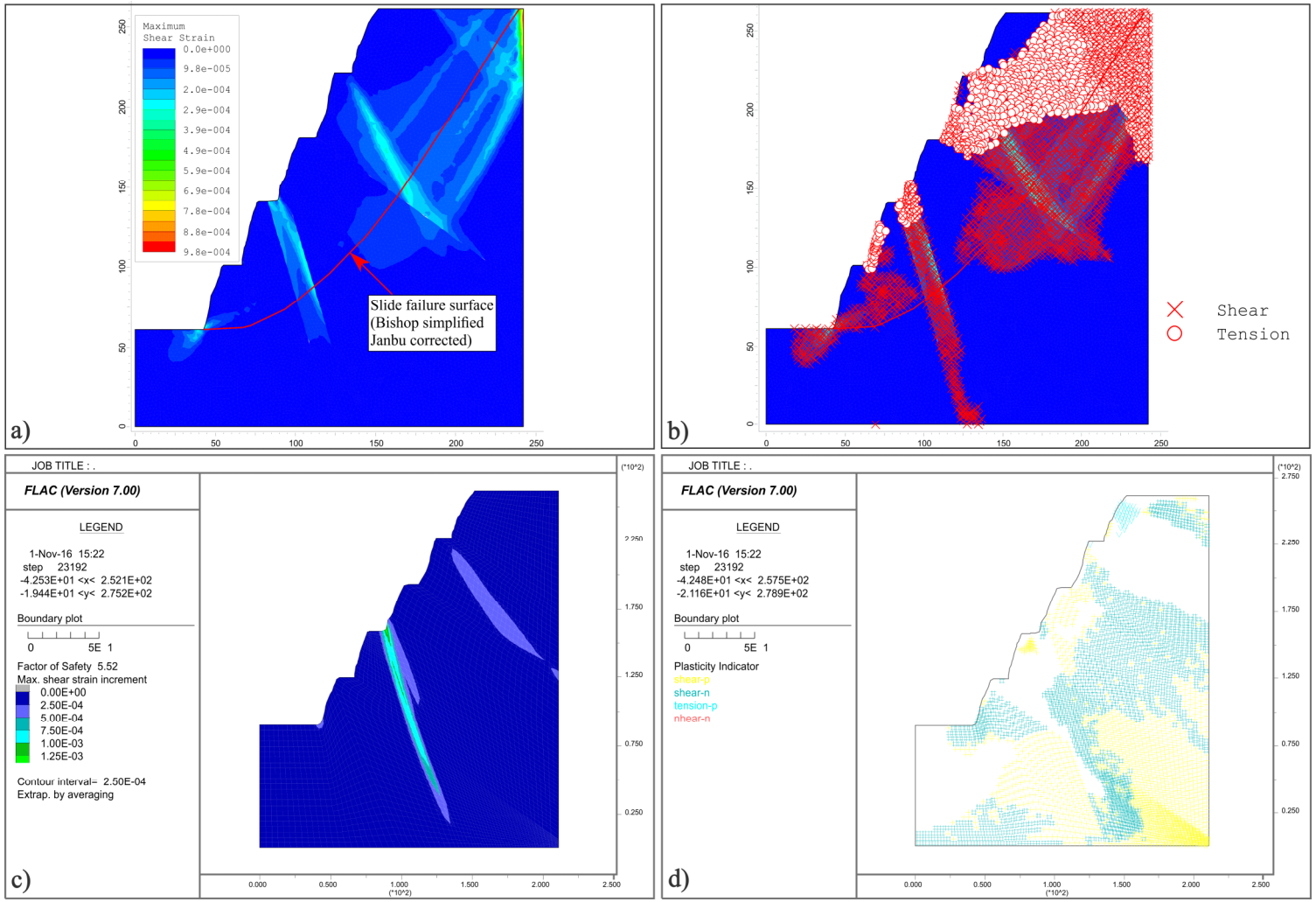

Figure 4.4. Profile C FEM results showing a) Maximum shear strain contours with Slide failure surfaces included, and b) Plasticity indicators, and FDM results showing c) maximum shear strain contours and d) Plasticity indicators, using the Generalized Hoek-Brown criterion.

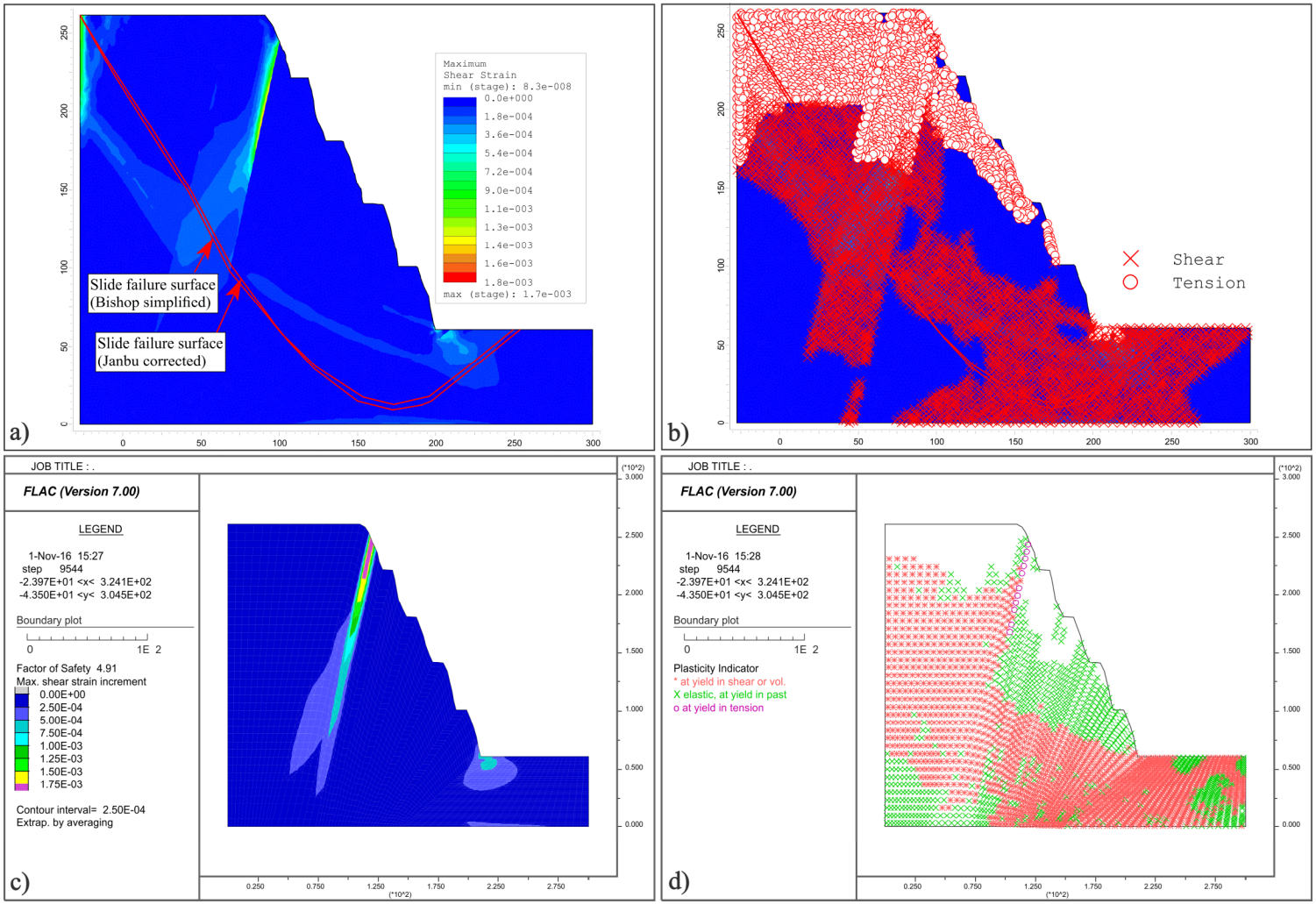

Figure 4.5. Profile A FEM results showing a) Maximum shear strain contours with Slide failure surfaces incorporated, and b) Plasticity indicators, and FDM results showing c) maximum shear strain contours and d) Plasticity indicators, using the Mohr-Coulomb strength criterion.

In profile B, safety factors of 5.57 and 5.69 were computed by the FEM and FDM respectively (Table 4.4). The maximum shear strain contours are shown in Figure 4.6a and c where a tendency of circular failure is observed from a clearly defined failure surface in both models. Both failure surfaces are initiated at the edge of the external boundary and extend down to the toe of the slope (Figure 4.6a, c). The maximum strain values of $1.3e^{-003}$ and $3.50e^{-03}$ in the FEM and FDM models respectively, occur along the inception point (behind crest) in the FEM and termination point (toe) in the FDM. The failure mode involves shearing through the profile with an accumulation of tension along benches (Figure 4.6b, d).

In profile C the safety factors computed by the FEM and FDM were 4.58 and 5.47 respectively (Table 4.4). The failure surfaces are similar to those seen using the GH-B failure criterion where no single surface is presented, but rather several (Figure 4.7a and c). In the FEM, the maximum shear strain of $9.8e^{-004}$ occurs at the edge of the outer external boundary followed by its confinement to the dolerite-metagabbro contacts (Figure 4.7a, c). There is also a faint surface comparable with the Slide surface which is approximately circular (Figure 4.7a). In the FDM the maximum strain of $1.25e^{-03}$ reveals a thin band confined to the dolerite intrusion (Figure 4.7c). According to the yielded elements in Figure 4.7b and d, this region fails by shearing through the rock mass.

Table 4.4. Results for the FEM and FDM for continuum profiles using the Generalized Hoek-Brown and equivalent Mohr-Coulomb strength criteria.

	Continuum			
	FEM (Phase2)		FDM (FLAC)	
	EM-C	GH-B	EM-C	GH-B
Profile A	4.84	4.95	4.91	5.06
Profile B	5.33	5.53	5.69	6.08
Profile C	4.58	4.30	5.47	5.52

4.3.2. Pseudo-discontinuum media

Ubiquitous joint rock mass model

In order to account for the presence of weak planes in a FDM Mohr-Coulomb model, joint networks were simulated via the Ubiquitous Joint network model. Two joint set inclinations were analysed separately, the inclination selection being based on critical mean joint sets that predicted plane and wedge failure.

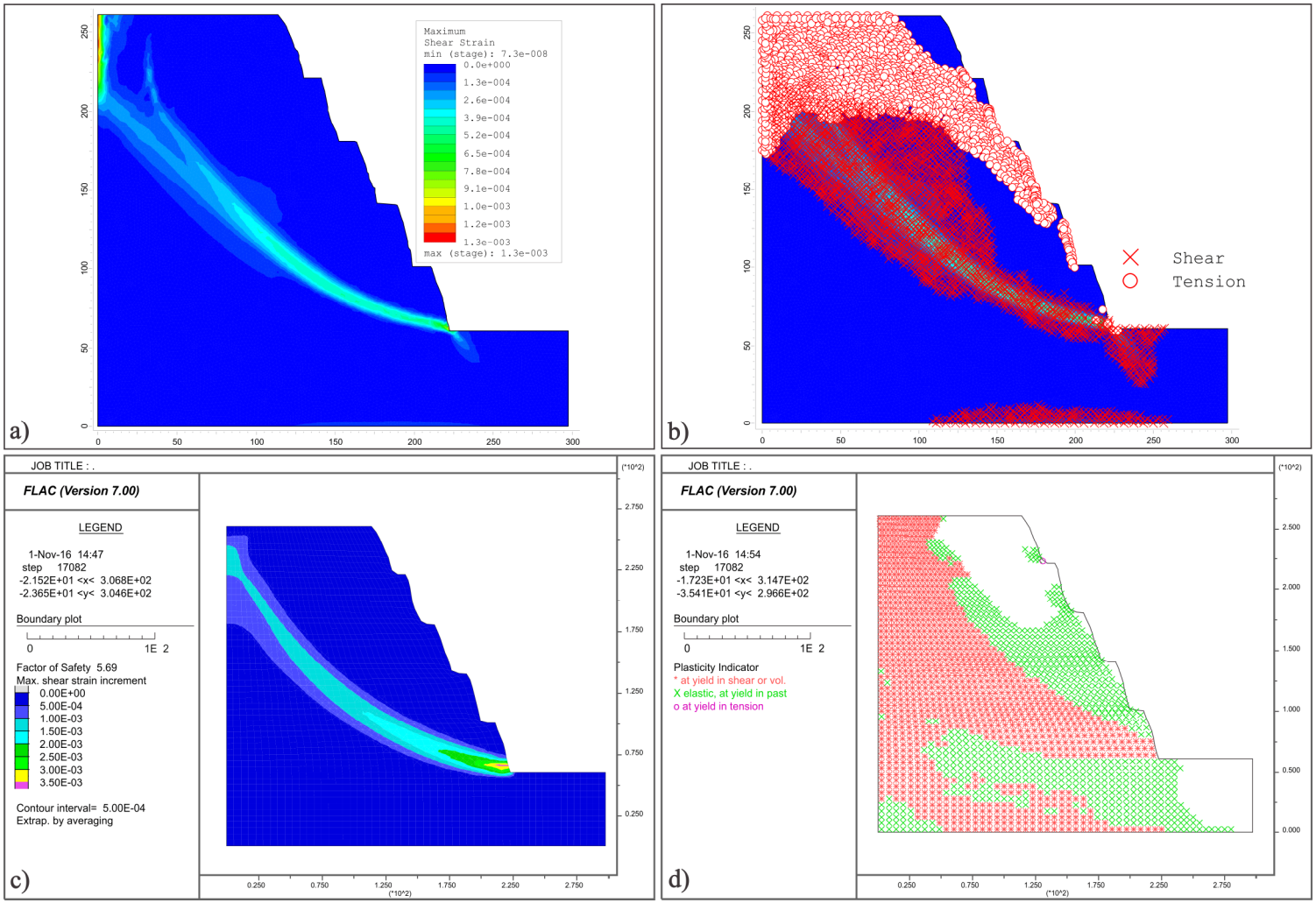

Figure 4.6. Profile B FEM results showing a) Maximum shear strain contours which Slide failure surfaces incorporated, and b) Plasticity indicators, and FDM results showing c) maximum shear strain contours and d) Plasticity indicators, using the Mohr-Coulomb strength criterion.

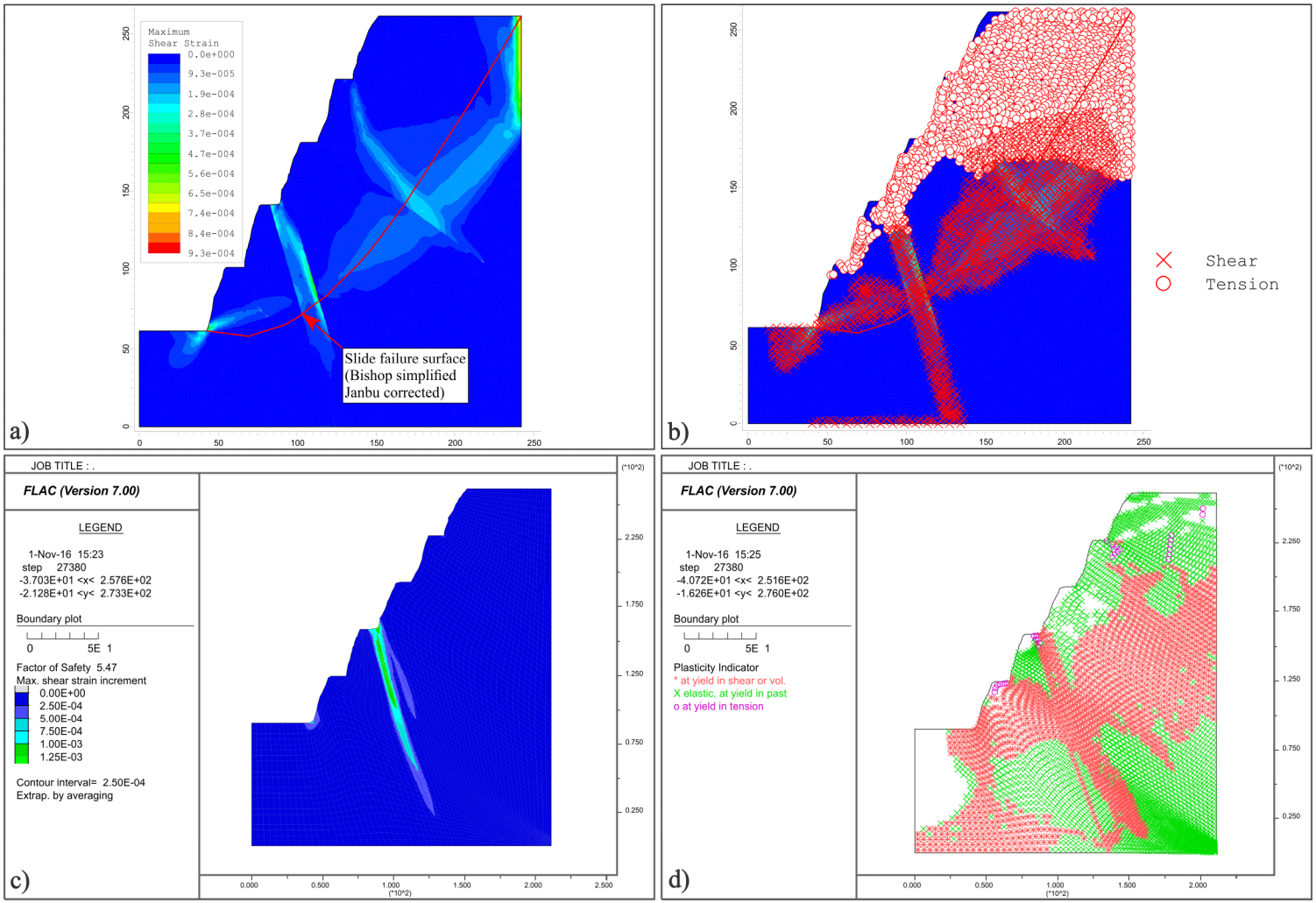

Figure 4.7. Profile C FEM results showing a) Maximum shear strain contours with Slide failure surfaces incorporated, and b) Plasticity indicators, and FDM results showing c) maximum shear strain contours and d) Plasticity indicators, using the Mohr-Coulomb strength criterion.

In profile A, joints sets incorporated into the model include J1 and J3 having inclinations of 81° and 57° respectively. The maximum shear strain contours associated with these inclinations are shown in Figure 4.8a and c. At 81° the safety factor obtained was 2.52 (Table 4.5). The maximum shear strain of $2.50e^{-04}$ occurs along the dolerite-metagabbro boundary and gradually diminishes to the outer external boundaries of the model (Figure 4.8a). The plasticity indicators show that this area is dominated by slip along ubiquitous joints (Figure 4.8b). When employing a joint inclination of 57°, very different results are obtained. The safety factor calculated was 0.51 (Table 4.5) where the highest shear strain of $1.0e^{+00}$ occurred along thin bands at the slope faces of the bottom two benches (Figure 4.8c). Upon examination of the yielded elements, it is evident that failure in tension occurs at these locations (Figure 4.8d). Tensile failures along ubiquitous joints are apparent at bench crests, whereas slip along ubiquitous joints occur predominantly throughout each bench (Figure 4.8d).

In profile B, J1 and J2 were applied to the ubiquitous joint model and had inclinations of 56° and 44° respectively. Safety factors of 0.65 and 1.01 were computed for J1 and J2 respectively (Table 4.5). Results found using an angle of 56° reveal an indication of planar failure along the uppermost bench slope face where the highest shear strain of $4.0e^{-0}$ occurs (Figure 4.9a). Yielded elements in this location show a combination of slippage along ubiquitous joints as well as tension (Figure 4.9b). With a joint inclination of 44° the highest shear strain of $8.0e^{-04}$ arises along the uppermost and lowermost benches. There is evidence of the formation and propagation of tension cracks behind the crest, as well as a deep-seated approximately planar failure surface, that is created from the corner of the external boundary farthest away from the slope face, and extends down to the toe of the slope (Figure 4.9c). Yielded elements also indicate slip along uqibuitous joints (Figure 4.9d).

In profile C, J1 and J2 with inclinations of 53˚ and 87˚ respectively, were incorporated into FDM models. Safety factor of 0.80 and 1.57 were computed for J1 and J2 respectively (Table 4.5). At 53˚ the sliding plane daylights out of the overall and bench face slope angles, thereby suggesting the formation of rigid blocks sliding along these planar joints. The highest value of shear strain being $1.00e^{-02}$ occurs at the uppermost bench face and extends slightly into the slope. A similar pattern is seen on all successive benches. Shear stain contours suggest the presence of a series of toppling blocks along the overall pit slope (Figure 4.10a). According to the plasticity indicators in Figure 4.10b, the bench floors are associated with tension, whereas the bench faces coincide with slip along ubiquitous joints. Non-daylighting joints such as J2 result in a failure mode involving sliding along ubiquitous joints and shearing through the rock mass (Figure 4.10d). The greatest shear strain of $3.50e^{-04}$ is seen at the vertical external boundary away from the slope

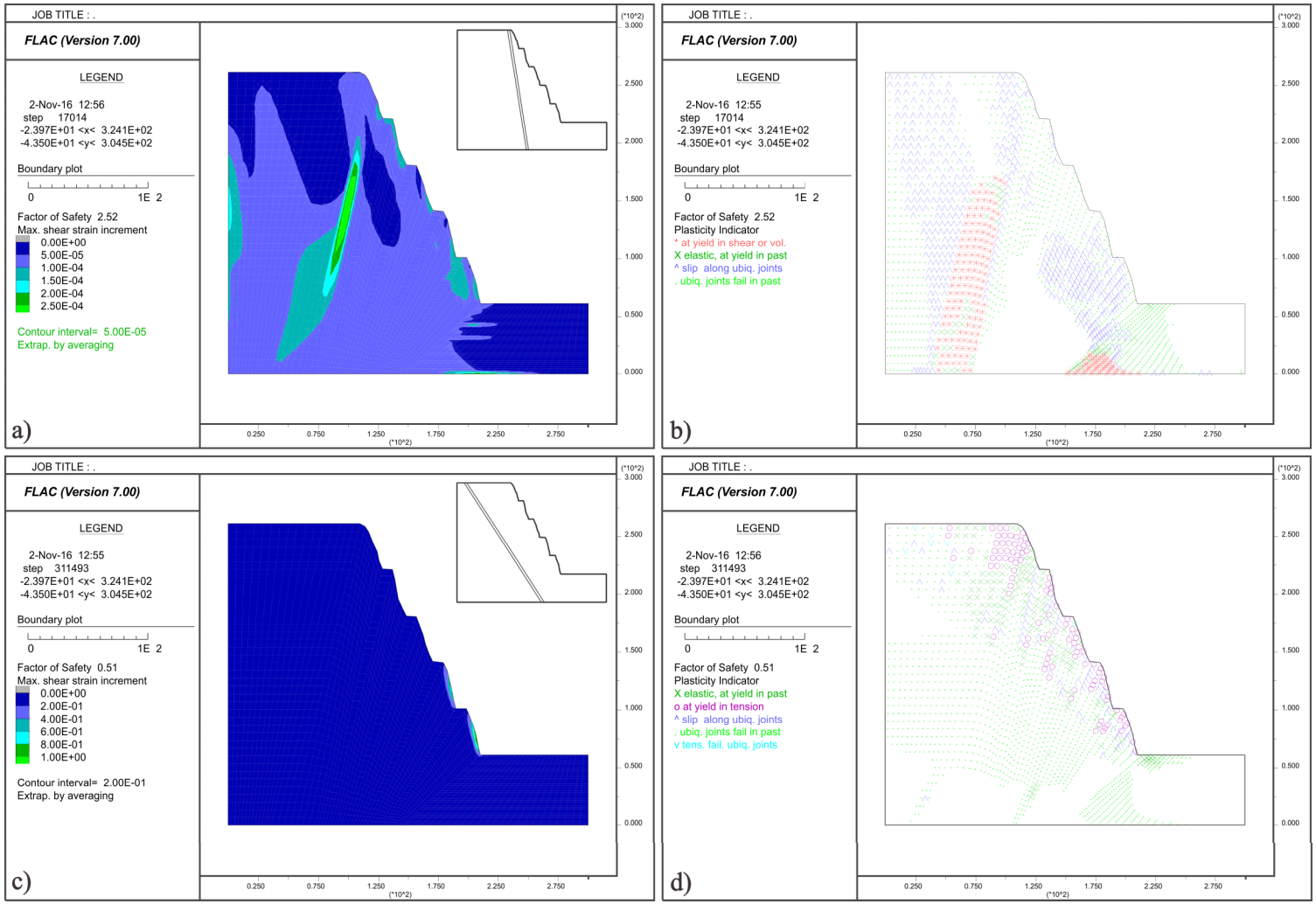

Figure 4.8. Results of the FDM with the Ubiquitous Joint network model for profile A with a) an inclination of 57° (J1), and its associated b) plasticity indicators and, c) an inclination of 81° (J3) and its associated d) plasticity indicators.

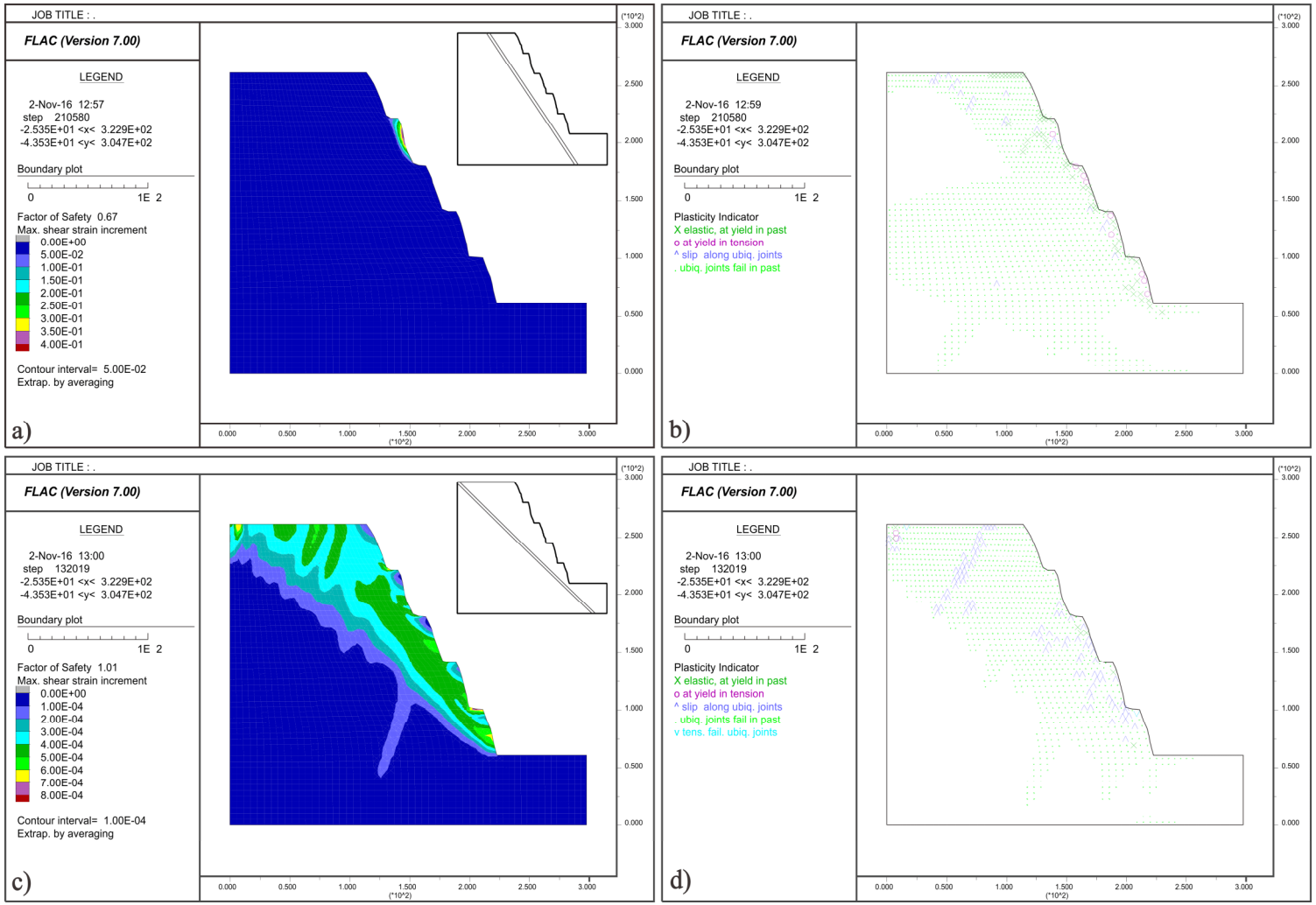

Figure 4.9. Results of the FDM with the Ubiquitous Joint network model for profile B with a) an inclination of 56° (J1), and its associated b) plasticity indicators and c) an inclination of 44° (J2) and its associated d) plasticity indicators.

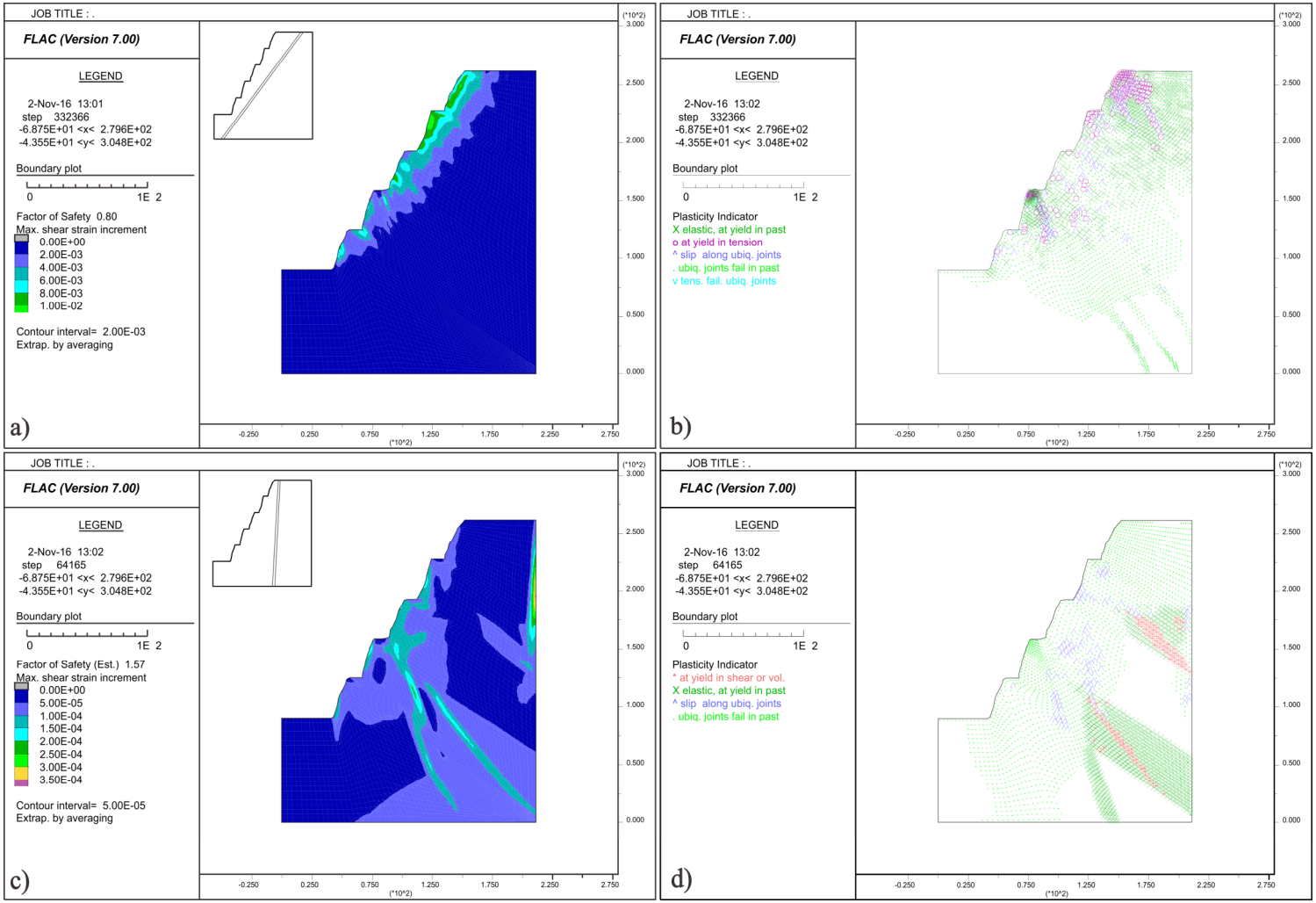

Figure 4.10. Results of the FDM with the Ubiquitous Joint network model for profile C with a) an inclination of 53° (J1), and its associated b) plasticity indicators and c) an inclination of 87° (J2) and its associated d) plasticity indicators.

face. No single clear failure plane is presented, but instead several thin bands are shown across the profile (Figure 4.10c). The bands bordering the slope face represent zones of shearing as opposed to the deep seated bands which represent zones where sliding occurs along ubiquitous joints. Shearing is confined within the tonalite material boundaries whereas sliding occurs within metagabbro (Figure 4.10d).

Parallel deterministic joint network

The Parallel Deterministic joint network also applied critical joint sets responsible for potential plane and wedge failures individually and combined. This was conducted by first assuming discontinuities to be of infinite length and subsequently of finite length, having a persistence of 0.8. This value is indicative of the uniform length of rock bridges occurring between each joint segment, where a value close to 1 implies near infinite length and a value closer to 0 suggests a near continuum material. This value was selected for comparative purposes with the Ubiquitous Joint network model in the FDM.

Joint set 1 (81˚ dip) in profile A shows a similar failure surface to that seen in the FDM, where the highest shear strain of $2.4e^{-003}$ occurs along the dolerite-metagabbro interface, and is dominated by shear failure (Figure 4.11a). The safety factor was found to be 2.89 (Table 4.5). Most horizontal displacement associated with this joint angle occurs in the vicinity of the second and third lowermost benches, and extends to the metagabbro-dolerite contact where the band of maximum shear strain exists. When applying J3 however, the maximum shear strain of $1.7e^{-004}$ occurs at the toe of the slope followed by the centre of the profile where the yielded elements are confined to the upper portion of the dolerite dyke (Figure 4.11b). A safety factor of 0.52 was calculated, and the highest degree of horizontal displacement is limited to the uppermost bench. When both joint sets are combined into a single model, similar results to J3 are obtained in terms of shear strength (Figure 4.11b, c), and a safety factor of 0.75 was obtained. Largest displacements however arise at the slope crests, as well as along the two succeeding bench faces, and follow J3 (58˚). In profile B, similar shear strain contours are seen for both J1 and J2, as well as a combination of J1 and J2, where greatest strain exists at the toe of the slope (Figure 4.11d, e, and f). Highest horizontal displacements are also nearly identical between the three models, occurring on the floor and slope face of the uppermost bench. The safety factors determined for J1, J2 and J1 and J2 combined were 0.41, 0.70 and 0.46 respectively (Table 4.5). Failure in tension is the main failure mode and is more prevalent at a joint angle of 44° in comparison to the other two angles. When applying a joint set angle of 53˚ (J1) in profile C, no clear failure surface arises from shear strength contours (Figure 4.11g), but since the joint set daylights into the slope face,

the mode of failure is expected to be in tension. On the contrary, J2 (87˚) has a non-daylighting inclination where sliding on discontinuities and shearing through the rock mass occurs. Several irregular bands can be observed from the shear strain contour plot (Figure 4.11h). When combining both sets, the shear strain contours do no not reveal a definite sliding plane, but the largest strain is experienced at the toe of the slope (Figure 4.11i). Yielded elements occur along bench floors and slope faces and signify failure in tension. The safety factors determined for J1, J2 and J1 and J2 combined were 0.65, 3.44 and 0.76 respectively (Table 4.5).

Rock bridges were introduced into the models through the application of joints of finite length having a persistence ratio of 0.8. In profile A, safety factors produced for J1, J3 and J1 and J3 combined were 4.51, 4.45 and 3.77 respectively (Table 4.5). The shear strain contours for all three situations show faint signs of the onset of circular failure, but the maximum strain continues to be confined to the upper boundary of the dolerite dyke when joint sets are analysed individually (Figure 4.12a-c). In profile B, the safety factors computed for J1, J2 and J1 and J2 combined were 5.00, 5.27 and 4.42 respectively (Table 4.5). The shear strain contours show well defined circular failure surfaces when joint sets are analysed independently (Figure 4.12d-f). In profile C, the safety factors computed for J1, J2 and J1 and J2 combined were 4.27, 4.55 and 3.84 respectively (Table 4.5). Shear strain contours are again more noticeable when joint sets are analysed independently (Figure 4.12g-i). Although multiple failure surfaces are shown for individual J1 and J2, there is a vague sign of circular failure for all three situations (Figure 4.12g-i).

Veneziano joint network

The Veneziano Joint network model was incorporated to introduce more realistic joint conditions due to the introduction of joints which vary in terms of orientation and inclination, and joint lengths which are based on an exponential statistical distribution.

In profile A the safety factors produced through the application of J1, J3 and J1 and J3 combined were 4.73, 4.60 and 4.34 respectively (Table 4.5). Greatest shear strain follows the upper boundary of the dolerite dyke when assessing J1 and a combination of J1 and J3 (Figure 4.13a and c). In all three cases however, there is an indication of an approximately circular surface extending from the overall slope crest to toe (Figure 4.13a-c). In profile B the safety factors produced through the application of J1, J2 and J1 and J2 combined were 4.30, 4.98 and 4.64 respectively (Table 4.5). All three cases show the maximum shear strain occurring along a thin circular band extending through the slope (Figure 4.13d-f). In profile C, the resulting safety factors

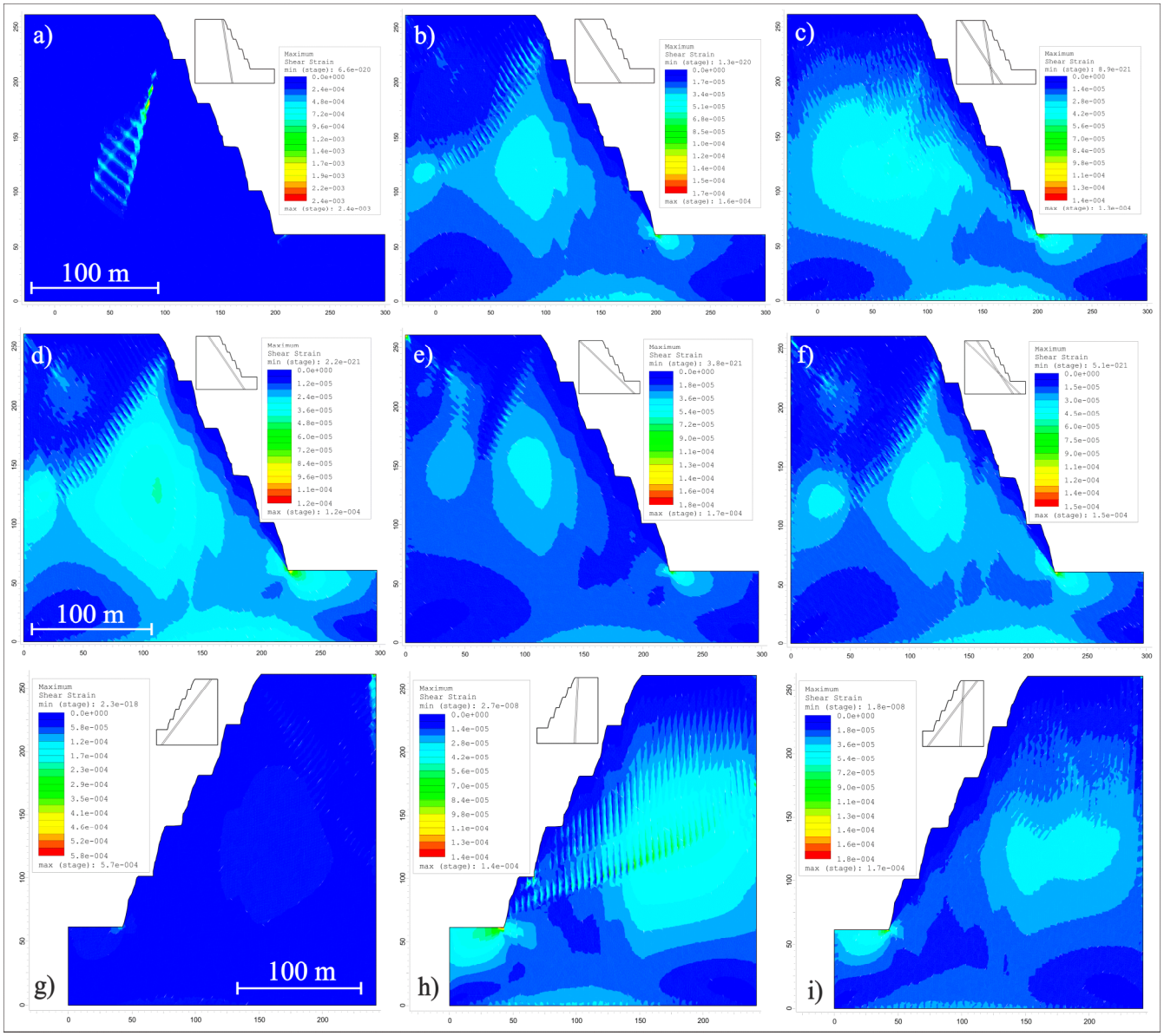

Figure 4.11. Maximum shear strain associated with the Parallel Deterministic joint network of infinite length showing a) profile A with joint set 1 b) profile A with joint set 3, c) profile A with combined joint sets 1 and 3, d) profile B with joint set 1 e) profile B with joint set 2, f) profile B with combined joint sets 1 and 2, g) profile C with joint set 1 h) profile C with joint set 2 and i) profile C with combined joint sets 1 and 2.

produced through the application of J1, J2 and J1 and J2 combined were 4.48, 4.51 and 4.22 respectively (Table 4.5). The maximum shear strain occurs along multiple approximately circular surfaces when analysing J1 and J2 independently (Figure 4.13g-i).

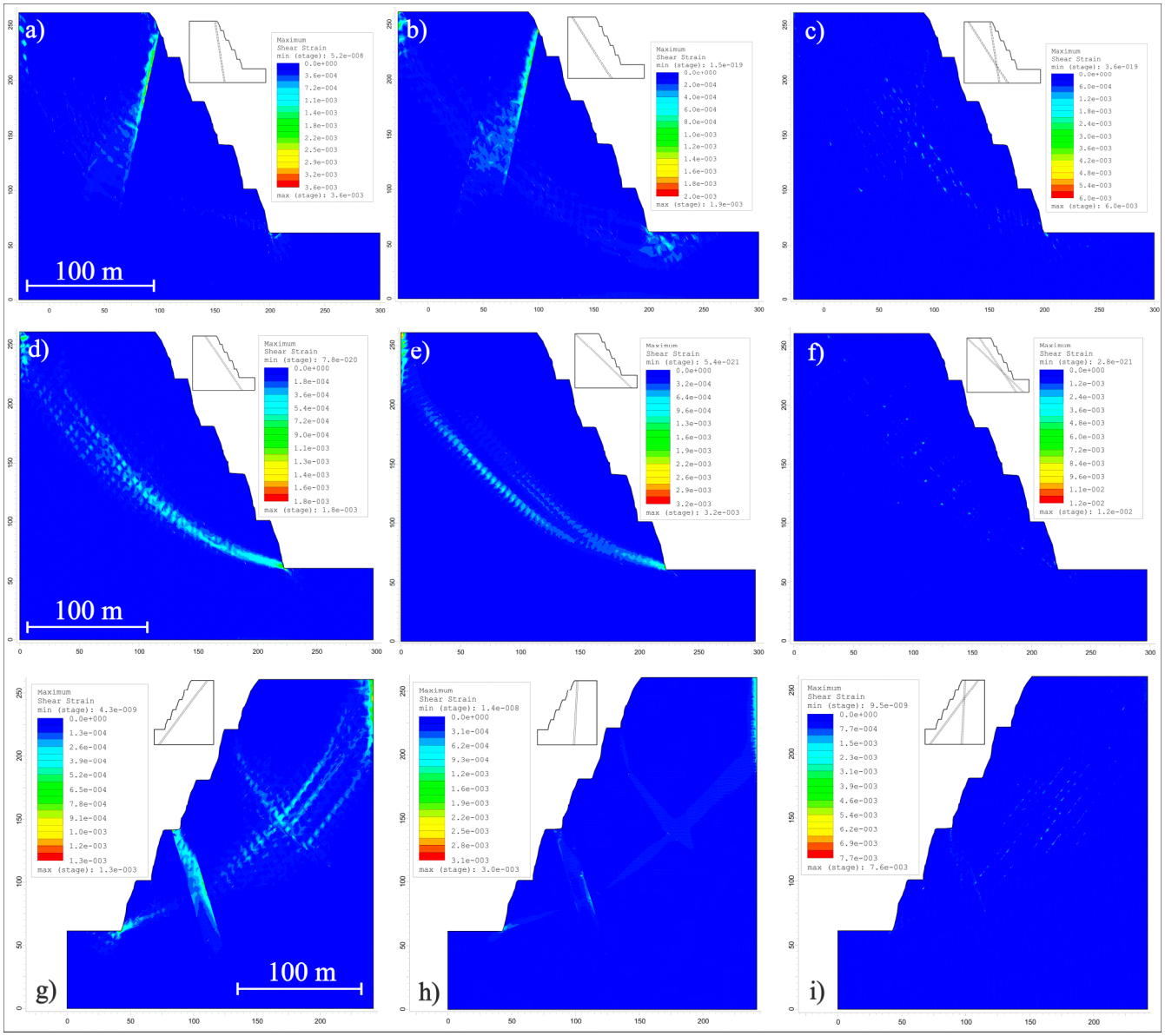

Figure 4.12. Maximum shear strain associated with the Parallel Deterministic joint network of finite length showing a) profile A with joint set 1 b) profile A with joint set 3, c) profile A with combined joint sets 1 and 3, d) profile B with joint set 1 e) profile B with joint set 2, f) profile B with combined joint sets 1 and 2, g) profile C with joint set 1 h) profile C with joint set 2 and i) profile C with combined joint sets 1 and 2.

4.4. Rockfall hazard assessment

Rockfall hazard analysis refers to the simulation of the trajectories of detached rock bodies. These analyses were conducted in two and three dimensions, taking into account the shape and volume of free rock blocks. For the 2D rockfall simulation it is evident that falling blocks of all shapes travelled to the bottom of the pit in all profiles (Figure 4.14a-c). According to Table 4.6, the majority of rocks terminated at the floor of the pit, the poor slope/cut slope topography of which

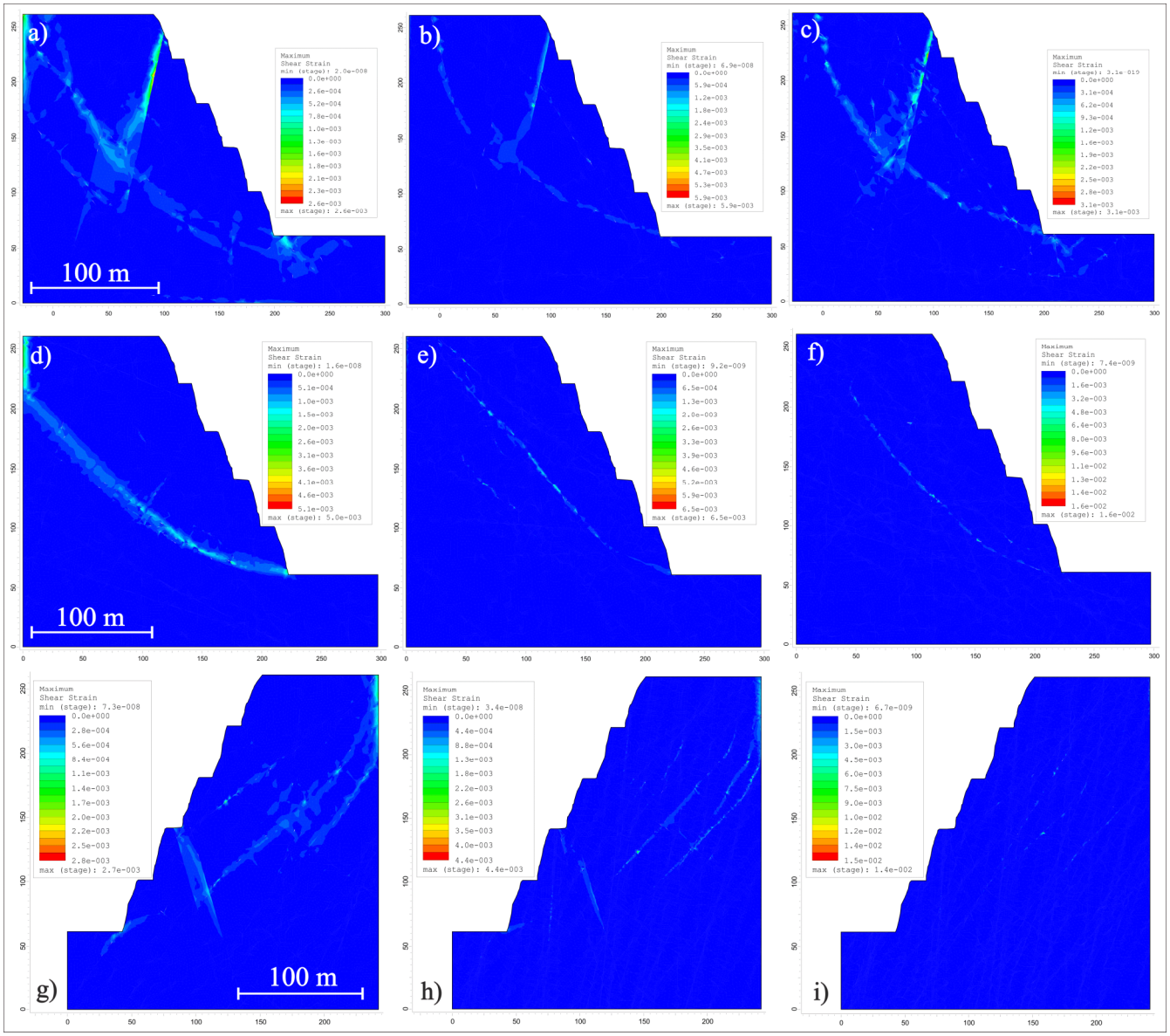

Figure 4.13. Maximum shear strain associated with the Veneziano joint network for a) profile A with joint set 1 b) profile A with joint set 3, c) profile A with combined joint sets 1 and 3, d) profile B with joint set 1 e) profile B with joint set 2, f) profile B with combined joint sets 1 and 2, g) profile C with joint set 1 h) profile C with joint set 2 and i) profile C with combined joint sets 1 and 2.

underperforms to the greatest extent where 94.4 % of rocks reach the bottom of the pit. Reduced berm widths caused by factors such as poor blasting, which creates overbreak at the crests and underbreak at the toes, by material being left at the toe of benches, and by berms becoming full, are clearly detrimental to the performance of the catch berms. The rock shapes achieving greatest velocities for good, moderate and poor slope/cut slope topography are the circle, the circle and the sphere shapes respectively. Their trajectory maximum velocity, energy and bounce heights

are shown in Table 4.7. These paths are shown in Figure 4.15a-c for the most problematic topography, which is the poor slope/cut slope topography.

Table 4.5. Safety factors obtained for pseudo-discontinuum media using the FEM and FDM.

Profile A			
	J1	J3	J1 & J3
Parallel Deterministic joint network (Infinite length)	2.89	0.52	0.75
Ubiquitous joint network	2.52	0.51	-
Parallel Deterministic joint network (Finite length)	4.51	4.45	3.77
Veneziano joint network	4.73	4.60	4.34
Profile B			
	J1	J2	J1 & J2
Parallel Deterministic joint network (Infinite length)	0.41	0.70	0.46
Ubiquitous joint network	0.65	1.01	-
Parallel Deterministic joint network (Finite length)	5.00	5.27	4.42
Veneziano joint network	4.30	4.98	4.64
Profile C			
	J1	J2	J1 & J2
Parallel Deterministic joint network (Infinite length)	0.65	3.44	0.76
Ubiquitous joint network	0.80	1.57	-
Parallel Deterministic joint network (Finite length)	4.27	4.55	3.84
Veneziano joint network	4.48	4.51	4.22

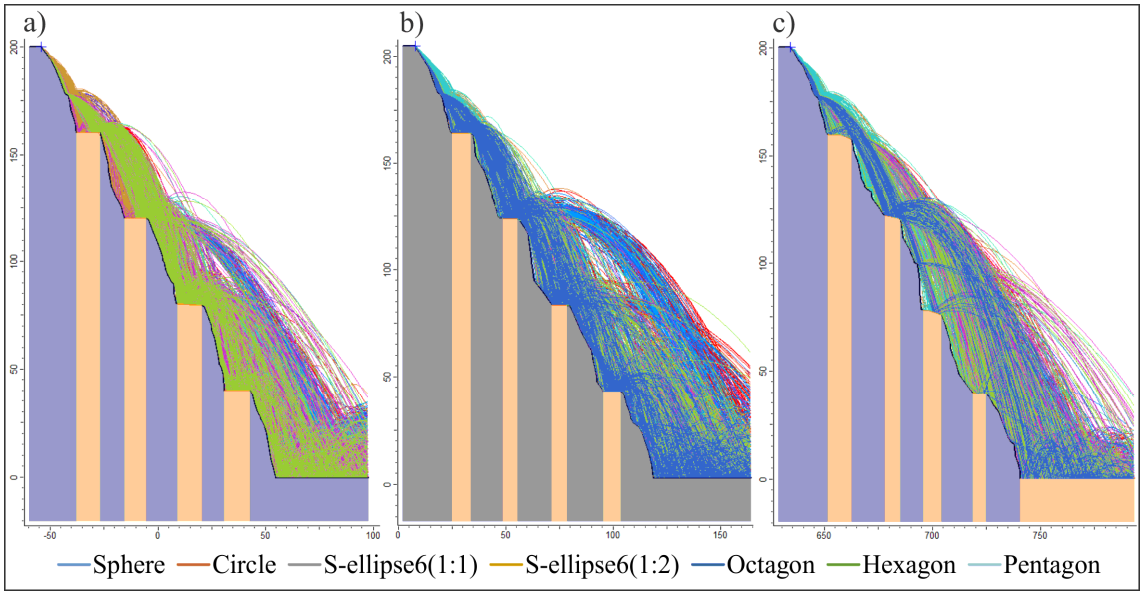

Figure 4.14. 2D rockfall trajectories along slopes simulating a) good slope/cut slope topography, b) moderate slope/cut slope topography and c) poor slope/cut slope topography.

Table 4.6. Total percentage of rocks collected at each bench.

	Good slope/cut slope topography	Moderate slope/cut slope topography	Poor slope/cut slope topography
	Collected rocks (%)	Collected rocks (%)	Collected rocks (%)
Bench 1	6.8	8.6	3.6
Bench 2	3.3	2.6	1.0
Bench 3	2.5	1.3	0.3
Bench 4	7.8	1.6	0.7
Floor	79.8	86.4	94.4

Table 4.7. Results of 2D rockfall trajectories along good, moderate and poor slope/cut slope topography.

	Translational velocity (m/s)	Rotational velocity (m/s)	Energy (kJ)			Bounce height (m)
			Rotational	Translational	Total	
Good	32.5	71.9	6.6	56.5	60.9	39.2
Moderate	34.2	79.7	8.2	58.5	62.0	53.9
Poor	40.0	76.3	8.7	85.7	94.3	47.82

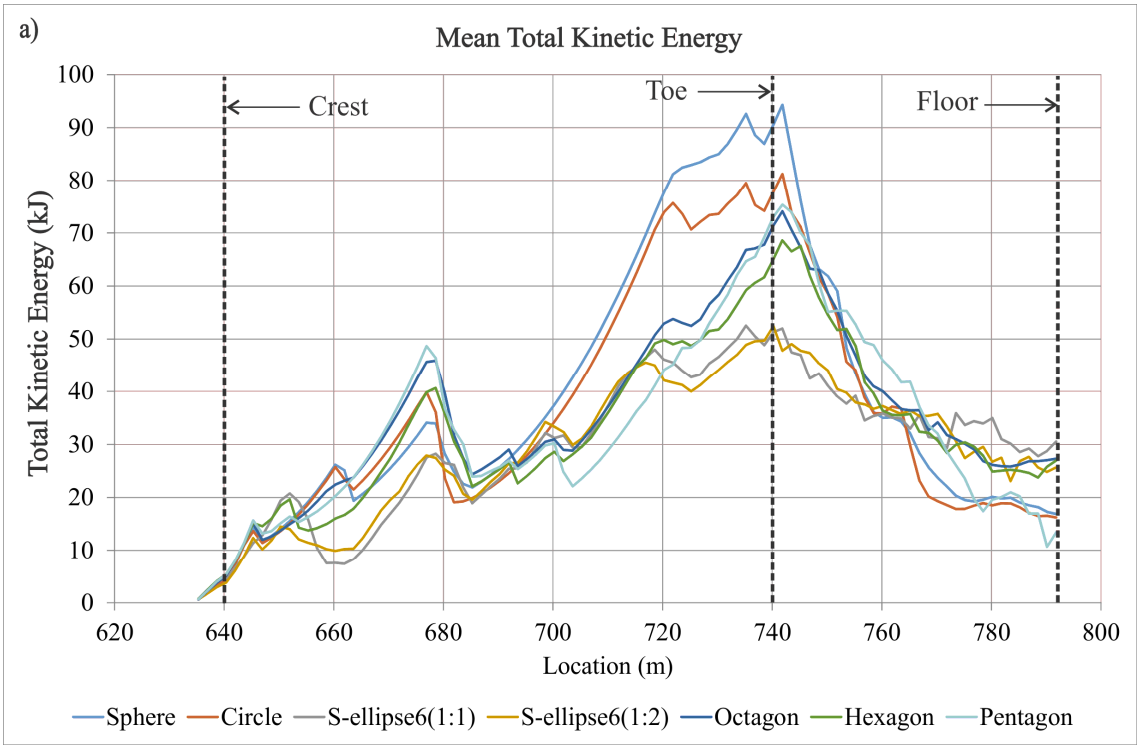

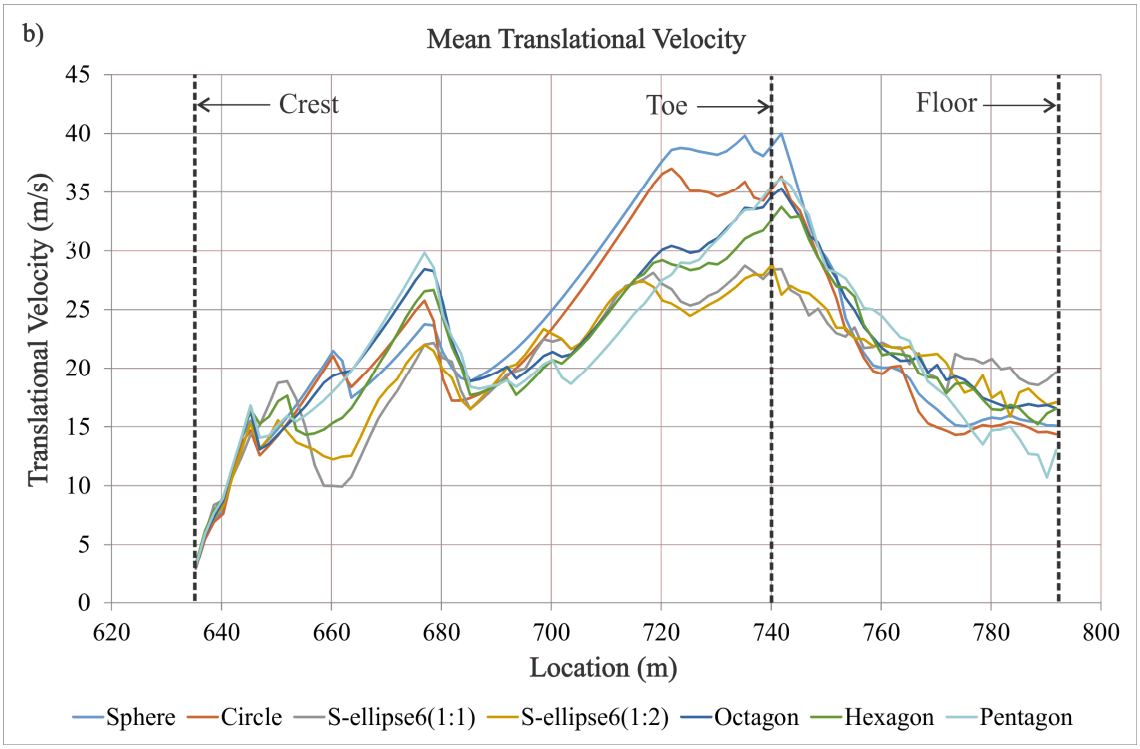

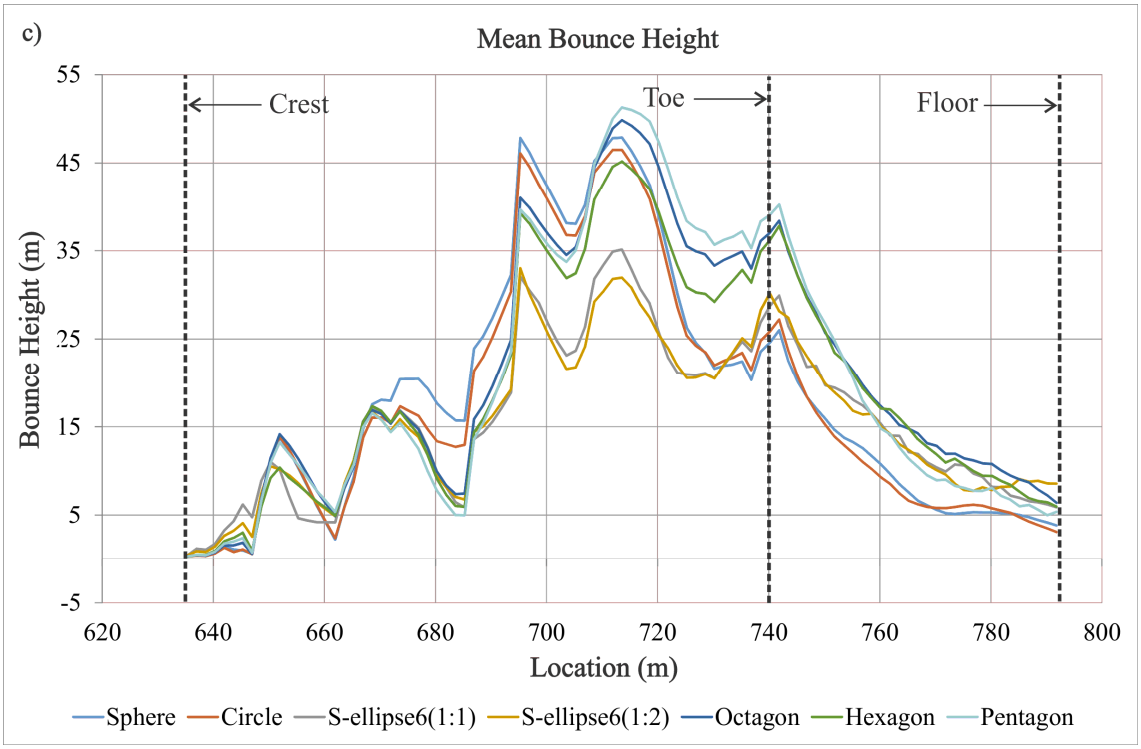

Figure 4.15. 2D results of poor slope/cut slope topography showing a) total kinetic energy, b) translational velocity and c) bounce heights.

For the 3D analysis, the rockfall paths (P1-P6) are shown as velocity contours in Figure 4.16 for the three cases of slope/cut slope topography, where they are seen ranging from slow movements, in blue, to rapid movements, in red. The rock shape achieving greatest velocities for good, moderate and poor slope/cut slope topography was the square box in path 1, sphere in path 6 and flat elongated box in path 4 respectively. Their trajectory maximum velocity and energy are shown in Table 4.8 and their full path details in Figures 4.17a-c and 4.18a-c, where it is apparent that the poor slope/cut slope topography produces the greatest rockfall velocity and total kinetic energy.

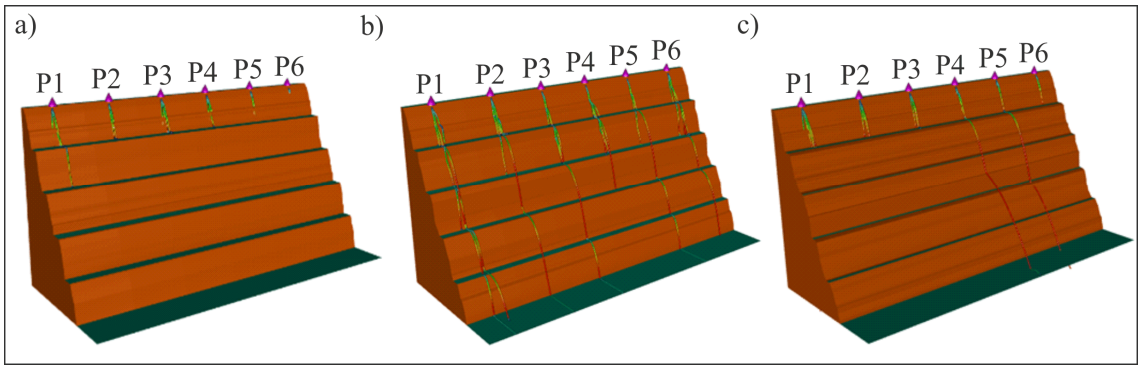

Figure 4.16. Rock fall trajectories along slopes depicting a) good slope/cut slope topography, b) moderate slope/cut slope topography and c) poor slope/cut slope topography.

Table 4.8. Comparison of Trajec3D rockfall trajectories along good, moderate and poor slope/cut slope topography.

	Velocity (m/s)	Energy (kJ)		
		Rotational	Translational	Total kinetic
Good (P1)	22.4	0.4	25	25.4
Moderate (P6)	44.8	1.3	100.1	101.5
Poor (P4)	51.8	0.1	134.0	134.2

Analyzing the case of good slope/cut slope topography (Figure 4.16a), the square box shape in P1 is the only body passing the first berm, terminating at the second. All other blocks are caught by the first berm in all paths. Along the slope depicting a moderate slope/cut slope topography (Figure 4.16b), P1 is associated with the square box shape coming to a standstill at the third berm, and both the sphere and angular rough cylinder reaching the floor of the pit. In P2, the flat elongated box halted at the second berm and the sphere at the pit floor. P3 shows that the angular rough smartie shape and angular rough cylinder terminated at the second berm, while the sphere was caught by the third. In P5 the angular rough smartie shape stopped at the second berm and

the sphere travelled to the bottom of the pit. In the last path, P6, the angular rough flat cylinder, angular rough smartie and angular rough cylinder shapes were caught by the second berm, while the sphere passed all four benches, reaching the pit floor. Along the slope depicting a poor slope/cut slope topography (Figure 4.16c), P1, P2, P3 and P6 show that no falling blocks were permitted past the first berm. P4 however shows that the flat elongated box moved right down to the bottom of the pit. In P5 the sphere was caught by the third berm while the flat elongated box stopped at the pit floor.

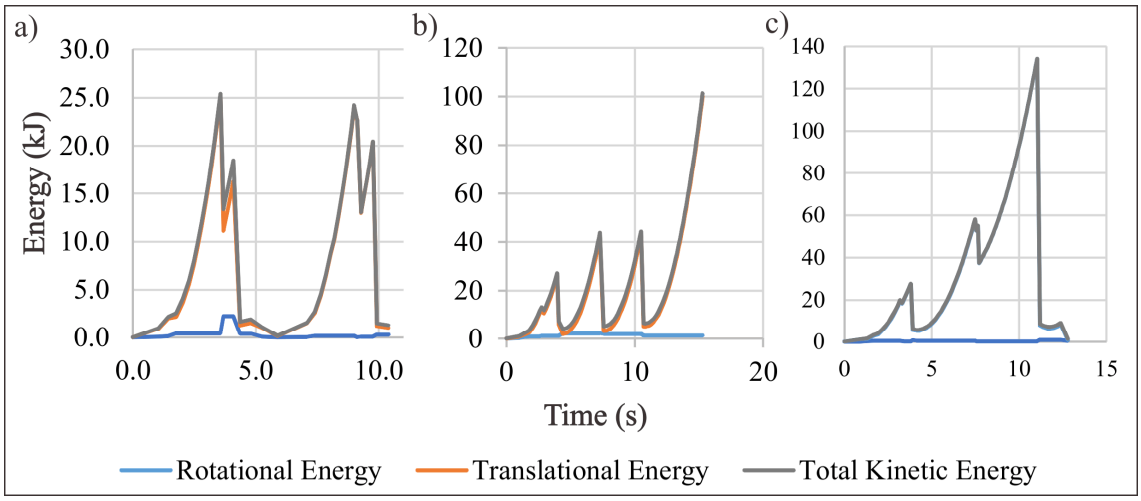

Figure 4.17. Trajec3D energy results for a) good slope/cut slope topography with path 1, b) moderate slope/cut slope topography with path 6 and c) poor slope/cut slope topography with path 4.

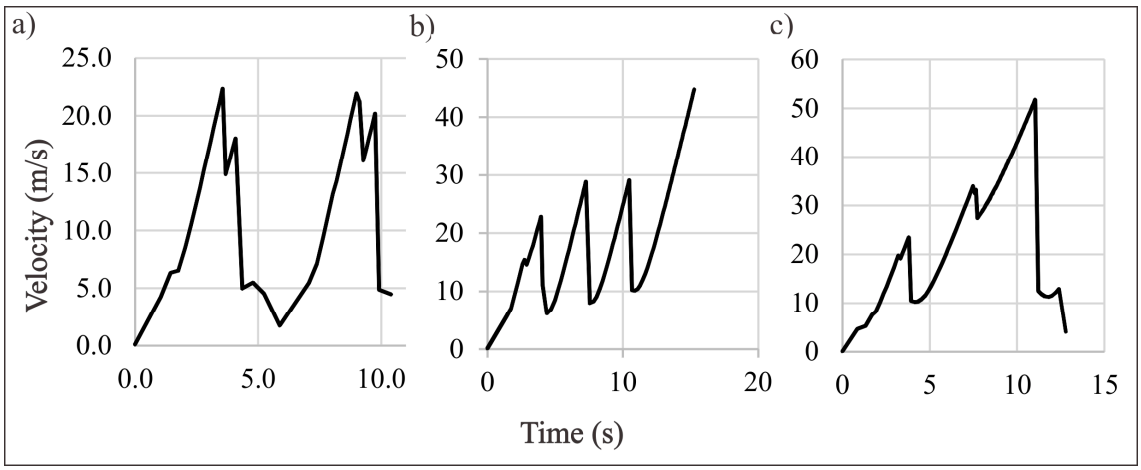

Figure 4.18. Trajec3D velocity results for a) good slope/cut slope topography with path 1, b) moderate slope/cut slope topography with path 6 and c) poor slope/cut slope topography with path 4.

It is evident that good slope/cut slope topography performs fairly well since only one falling block passed the first berm and none reached further than the second berm (Table 4.9). The moderate slope/cut slope topography seems to perform worst, where most paths are associated with falling blocks reaching the floor of the pit (Table 4.9). Poor slope/cut slope topographies allow for more flattened shapes such as the flat elongated box to reach the pit floor, whereas good slope/cut slope topography does not.

Table 4.9. 3D analysis findings of falling block shapes which passed the 1st berm ×, and ◊ represents falling blocks which travelled to the bottom of the pit.

	0.1 tons																									
Path	Good slope/cut slope topography								Moderate slope/cut slope topography								Poor slope/cut slope topography							
	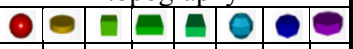																									
1			×						◊				×	◊												
2									◊			×														
3									◊					×	×											
4									×			×	×									◊				
5									◊						×		×									
6									◊	×				×	×											

CHAPTER 5

DISCUSSION

This chapter discusses the results of the stability of slopes in terms of the factor of safety (FoS), probability of failure (PoF) and strain, as well as rockfall hazard analysis. Intact material strength and behaviour was first analysed using the limit equilibrium program Slide (Rocscience Inc., 2015) to evaluate potential curved failure surfaces. The same situation was subsequently applied to continuum numerical FEM code, Phase2 (Rocscience Inc., 2015) and FDM code, FLAC (Itasca, 2011). Next, the influence of discontinuities on rock slope stability was assessed through the introduction of joints as joint network models, including the Parallel Deterministic joint network of infinite length and finite length, the Ubiquitous Joint network and the Veneziano Joint network models. Material modelling was based on strength parameters pertaining to the Generalized Hoek-Brown (GH-B) failure criterion as well as equivalent Mohr-Coulomb (EM-C) failure criterion strength parameters. The calculation of these equivalent parameters (ϕ and c) was based on the method described by Hoek et al. (2002) in which a range of minor principal stress values, defined by $\sigma_t < \sigma_3 < \sigma'_{3max}$, are employed in the GH-B equation, and then fitting an average linear relationship to the curve produced.

5.1. Continuum media

5.1.1. Stress controlled Limit Equilibrium Methods (LEM)

Factor of Safety

The stress controlled LEM was performed using the Bishop simplified and Janbu corrected methods. The resulting safety factors exceeded one for all profiles, thus suggesting that resisting forces have overcome driving forces, resulting in stable conditions. A general trend (profiles B and C) is apparent in which EM-C slopes are associated with slightly larger safety factors than GH-B slopes (Table 5.1). This agrees with a LEM of analysis conducted by Hammah et al. (2004) for homogeneous rock slopes.

Based on both the EM-C and GH-B strength criteria, the Janbu corrected method computes slightly greater safety factors for all profiles, in comparison with the Bishop simplified method (Table 5.1). A similar relationship was found by Fredlund and Krahn (1977), Verma et al. (2013) and Singh et al. (2016). These elevated safety factors may be attributed to the incorporation of a correction factor (f_o) to account for the effect of interslice shear forces, where without it, the method assumes no shear forces (Fredlund and Krahn, 1977). This factor is a function of the

material strength and shape of failure surfaces (Fredlund and Krahn, 1977). According to Fredlund et al. (1981), the use of this correction factor generally increases the factors of safety by up to ten percent. It is also known that safety factors calculated using force equilibrium methods, such as Janbu's method, are very sensitive to assumed inclinations of interslice side forces (Duncan, 1996). It is apparent that a greater difference in safety factors exists between the two methods when employing the EM-C strength criterion, with variations of 4.1 %, 3.8 % and 2.6 % as opposed to 3.3 %, 3.1 % and 0.3 % for the GH-B, criterion for profiles A, B and C respectively.

Table 5.1. Safety factors determined using stress controlled Limit Equilibrium Methods.

	Profile A		**Profile B**		**Profile C**	
Method	**EM-C**	**GH-B**	**EM-C**	**GH-B**	**EM-C**	**GH-B**
Bishop simplified	4.49	4.78	5.26	5.23	4.64	4.35
Janbu corrected	4.90	5.11	5.67	5.56	4.89	4.37

Failure surfaces – Circular failure mechanisms

Critical surfaces produced using the stress controlled LEM are approximately circular, with those produced in profiles B and C being shallower than those generated for profile A (Figure 5.1a-c). For all three profiles, the failure surfaces produced by the Bishop simplified and Janbu corrected methods are very similar for both strength criteria. Those generated using the EM-C parameters occur as marginally deeper set failure surfaces which terminate further away from the slope crest in comparison with those associated with the GH-B strength criterion (Figure 5.1a-c). Dong-Ping et al. (2016) compared results of the GH-B and EM-C failure criteria and categorized failure surfaces as shallow, intermediate and deep, and recognized variations in normal stress distributions along these surfaces, which thus indicates that stability conditions achieved via the two methods were inconsistent. For shallow failure surfaces such as those seen in profiles A and B, larger safety factors are determined by the EM-C criterion because normal stresses along these shallow failure surfaces are small. Dong-Ping et al. (2016) concluded that the EM-C criterion overestimates the stability of slopes with shallow failure surfaces.

For profile A, both strength criteria formed failure surfaces starting ahead of the toe of the slope (Figure 5.1a). The EM-C criterion with the Bishop simplified method produced a marginally shallower failure surface at the onset, but became inverted upslope with the failure surface of the Janbu corrected method in the metagabbro unit ahead of the dolerite dyke (Figure 5.1a). In contrast, the GH-B criterion with the Janbu corrected method produced a slightly shallower failure

surface, and only become inverted with that of the Bishop simplified method in the metagabbro unit after encountering the same dolerite dyke (Figure 5.1a). For profiles B and C, both strength criteria generated nearly identical sliding planes for the two LEMs, which commenced at the toe of the slope (Figure 5.1b, c). It is clear that the shape and location of the failure surfaces are governed by prevailing geological conditions, where the weaker and more extensive dolerite units in Profile A interrupt the truncation of failure surfaces, thus allowing them to extend beyond the toe of the slope.

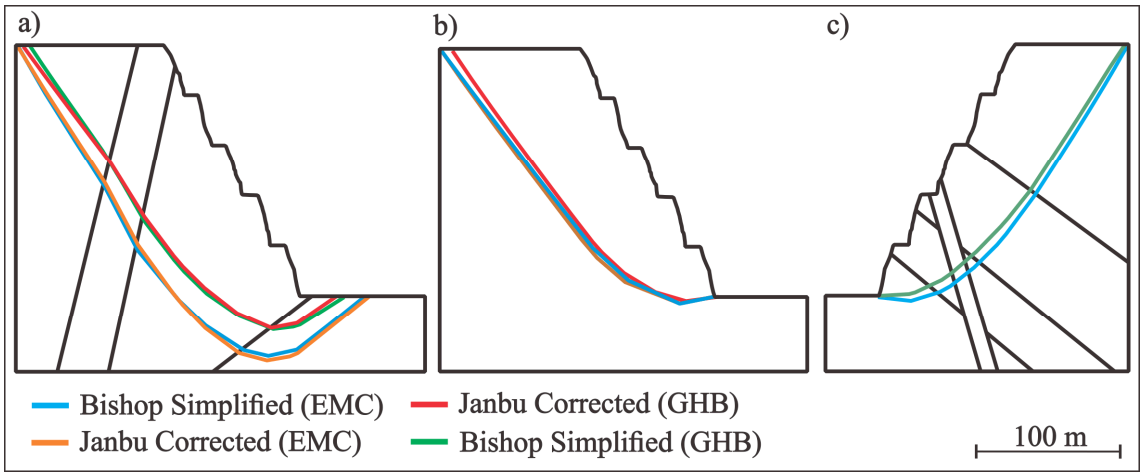

Figure 5.1. Stress controlled LEM sliding planes for profiles a) A, b) B, and c) C.

In summary, the resultant stable conditions imply that circular shear failure is not the likely mode of failure and that structurally controlled failure mechanisms may ensue, which is expected for low stress environments. The high level of stability corresponds to large shear strengths, which provide resistance over the balance of the slope (Tharp and Coffin, 1985). It may also be due to the fact that the toe of the slope occurs in the stronger metagabbro unit. There is fairly good agreement in results when employing GH-B and EM-C parameters, based on the technique proposed by Hoek et al. (2002), which suggests its effectiveness.

5.1.2. Numerical models

Factor of Safety

Safety factors calculated by the Finite Element Method (FEM) and Finite Difference Method (FDM) for continuum media are similar and exceed one, implying stable slopes (Table 5.2). There is relatively good agreement among the three profiles between the EM-C and GH-B strength criteria, where the latter generally produces slightly larger safety factors (Table 5.2), a relationship

similar to that found by Shukha and Baker (2003) using the same FDM code. This does not however correlate with findings of the stress controlled LEM where the application of the EM-C criterion returned greater safety factors. In comparison to the LEM, a reduced variation in safety factors between the two strength criteria is seen in profiles A and C, whereas an increase is apparent for profile B. Both methods calculate the greatest variation in safety factors for profile C and the lowest for profile A.

The FEM calculates lower safety factors than the FDM, which determines on average 5.3 %, 3.1 % and 11.1 % greater values for profiles A, B and C respectively. The lowest FoS calculated by the FEM with both strength criteria is associated with profile C, followed by A and then B (Table 5.2), which correlates with the average values presented by the stress controlled LEMs. In contrast, the lowest value calculated by the FDM with both strength criteria is associated with profile A, followed by C and then B (Table 5.2). It is therefore apparent that profile B is associated with the greatest safety factors among both numerical methods and strength criteria. Although Hammah et al. (2005) found identical safety factors for homogeneous GH-B and EM-C rock slopes using the FEM SSR technique, a reduction in safety factor occurred with the inclusion of a weaker layer, in which shear strength accumulation was more confined to the weaker material. It is therefore possible that reduced safety factors for profiles A and C could be associated with the inclusion of units of lower strength such as dolerite.

Table 5.2. Safety factors obtained for continuum media using the FEM and FDM.

	FEM		**FDM**	
	EM-C	**GH-B**	**EM-C**	**GH-B**
Profile A	4.84	4.95	4.91	5.06
Profile B	5.33	5.53	5.69	6.08
Profile C	4.58	4.30	5.47	5.52

When making comparisons between the numerical methods and LEMs it is evident that, for profile A, the FoS produced by the FEM is 0.6 % and 1.6 % lower for the EM-C and GH-B strength criteria respectively, than that derived by LEM (Figure 5.2). The same relationship is seen for profile C, but at 3.3 % and 0.8 % for EM-C and GH-B strength criteria respectively (Figure 5.2). According to Lorig and Varona (2001) the SSR technique is expected to determine lower safety factors than other methods, since numerical methods automatically satisfy rotational and translational equilibrium. A negative correlation however is depicted for profile B, where higher safety factors are computed by numerical methods rather than LEMs (Figure 5.2). This is consistent with results by Sjoberg (1999) where, for a homogeneous profile, safety factors

obtained via LEM were conservative in comparison with those determined by numerical models, which could be attributed to the LEM assumption that the full shear strength is mobilized at the same time along the complete failure surface. Inconsistencies are introduced by the FDM for profiles A and C. In profile A, a marginally greater FoS (0.1 %) is obtained using the FDM with the EM-C criterion when compared to LEM results (Figure 5.2). In profile C, the FDM with the GH-B criterion produces a greater FoS (11.6 %) compared to that produced using the LEM (Figure 5.2).

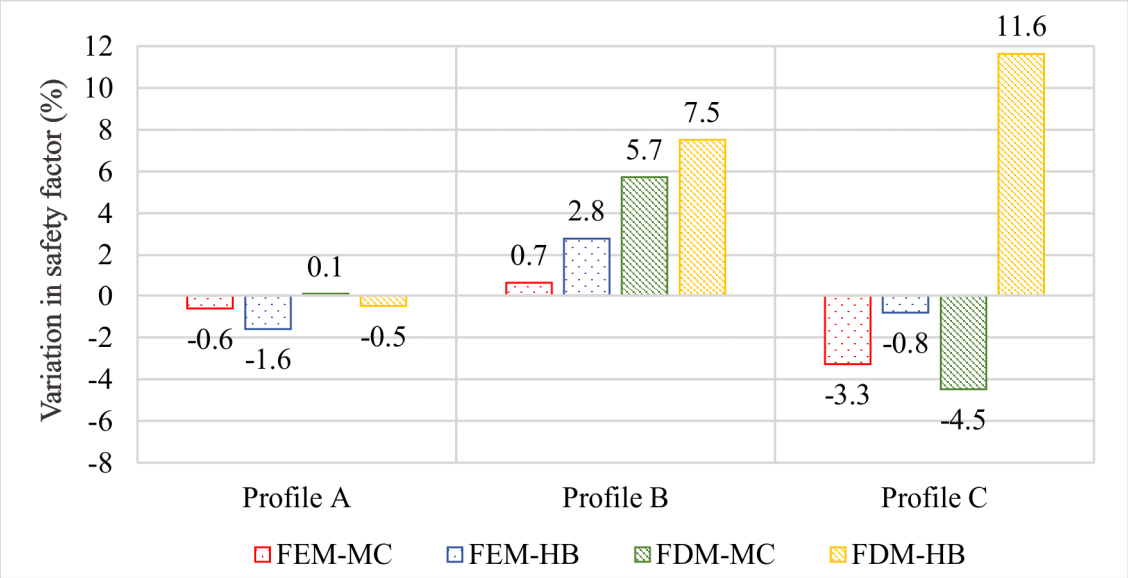

Figure 5.2. FEM and FDM FoS variation from LEM for continuum media.

Failure surfaces

In profile A, the location of the failure surfaces predicted using the two strength criteria with the FEM and FDM were comparable. The GH-B strength criterion produced greater shear strain values and more defined zones of accumulation, which occur as subvertical bands along the upper dolerite contacts. These shear strain accumulation zones indicate that as failure is approaching, this area would initially be damaged and would have experienced the most severe damage when failure commences (Zheng *et al*. 2008). Resulting failure surfaces produced by the numerical methods do not coincide with the critical failure path produced using the stress controlled LEM for profile C.

Although similar failure surfaces are produced for both criteria with the FEM and FDM for profile B, a contrasting relationship is apparent where the largest maximum shear strains result from the EM-C strength criterion. Both models indicate circular shear failure mechanisms, where the GH-B strength criterion generates more restricted shear zones in comparison to the EM-C criterion,

which propagates through the entire slope to the toe of the slope as demonstrated by Sjöberg (2001) for high slopes of homogeneous hard rock materials. The EM-C strength criterion also results in marginally deeper circular failure surfaces than the GH-B strength criterion, thus agreeing with results from the stress controlled LEMs.

For profile C, there is good agreement in failure surfaces generated via the FEM and FDM and using the GH-B and EM-C strength criteria. Identical values of maximum shear strain are produced between two strength criteria and for both models, where the FDM generated the greater value. In further detail, the FEM revealed identical shear strain contours among the two strength criteria where the greatest strain accumulation is associated with the dolerite intrusion and the tonalite-metagabbro contact. Shear strain contours also expose the formation of a circular surface through the slope, thus coinciding with the critical failure path produced using the stress controlled LEMs. This may be attributed to the occurrence of numerous inhomogeneous zones (Giani, 1992). The FDM however, show no signs of a circular failure surface in both models. When employing the EM-C criterion the maximum strain accumulation zones previously mentioned are revealed, but to a lesser degree, where the zone associated with the tonalite-metagabbro contact is lost completely. According to Cai (2008) the difference in yielded zones between the FEM and FDM relates to the solution scheme adopted, which forms different stress paths.

It can be concluded that the FEM/FDM with the SSR technique produce comparable safety factors when rock material is modelled using GH-B strength parameters and EM-C strength parameters. When compared to critical failure surfaces calculated by stress controlled LEMs, similar failure surfaces are only produced for homogeneous profile B, and potentially with profile C. According to Sjöberg (2001), such inconsistencies may be partially due to tensile failure not being accounted for in LEMs. Sjöberg (2001) also states that the failure surfaces produced using LEMs may not represent the final failure surface if retrogressive failure ensues through the removal of falling material. Numerical models also show little evidence of tension crack development, which may be attributed to large tensile strengths (Tharp and Coffin, 1985).

5.2. Pseudo-Discontinuum media

Near surface environments such as open pit mines are more often associated with structurally controlled failures due to low stresses. Joint orientation in massive rock units may be more or less random or may exist as numerous well-defined sets (Terzaghi, 1962). In this study both such circumstances are analysed in the form of a variety of joint networks, which form pseudo-discontinuum media. The joint networks range from having joints of infinite lengths across the

profile, to finite lengths where rock bridges are introduced along joint planes by altering joint persistence.

Factor of Safety

The results of the three profiles representing pseudo-discontinuum media can be compared among the various joint network models employed. In all profiles there is a good correlation in safety factors obtained between the Parallel Deterministic joint network of infinite length and Ubiquitous Joint network, as well as between the Parallel Deterministic of finite length and Veneziano Joint network (Figure 5.3). It is also apparent that the former correlate well with the structurally controlled LEMs and the latter with stress controlled LEMs (Figure 5.3). The structurally controlled LEM however seems to underestimate safety factors whereas the stress controlled LEM generally overestimates safety factors.

For profile A, comparable safety factors are calculated via the Parallel Deterministic joint network of infinite length and the Ubiquitous Joint network for J1 and J3 (Figure 5.3). In both joint network models, J1 suggest stable conditions as opposed to J3 suggesting unstable conditions (Figure 5.3). These results agree with those of the structurally controlled LEM, where planar failure along J3 was probable at both overall and stack angle levels, having safety factors of 0.93 and 0.72 respectively (Figure 5.3). When incorporating a combination of joint J1 and J3 via the FEM, unstable conditions are presented, with a safety factor 0.75 (Figure 5.3). A similar result was found using the kinematic and LEM of analysis for wedge failure, which indicated probable wedge sliding along J3 (Figure 5.3). Greatest safety factors for profile A are associated with the Parallel Deterministic of finite length and the Veneziano Joint network, which indicate stable conditions (FoS = 3.77-4.73), the lowest of which are computed for the combined mean joint sets (Figure 5.3). Very similar safety factors are also produced between these joint networks for individual sets J1 and J3 (Figure 5.3). Although safety factors vary between continuous joint networks and joint networks which include rock bridges, similar trends exist among them (Figure 5.3).

For profile B, safety factors produced via the Parallel Deterministic joint network of infinite length and the Ubiquitous Joint network indicate unstable conditions for all three joint orientation conditions (FoS = 0.41-0.70) apart from J2 for the Ubiquitous Joint network, which suggests a critically stable slope (FoS = 1.01) (Figure 5.3). Very similar values are computed for individual sets J1 and J2, where lowest safety factors are computed by the former. The values relating to the Parallel Deterministic joint network of infinite length do not coincide with those produced by the structurally controlled LEM, where slopes were deemed stable, and the lowest value was

associated with joint set 2 when assessing planar failure. Values produced through the application of joint set 2 in the Ubiquitous Joint network does, however, correlate with findings of the structurally controlled LEM, where wedge failure was possible along J2 at both overall (PoF = 13.86 %) and stack angle levels (PoF = 13.86 % (Figure 5.3). When combined sets J1 and J2 are incorporated into the model as Parallel Deterministic joint network of infinite length, there is a fair amount of variation when compared to the structurally controlled LEM for wedge failure, where the latter produce a safety factor that is 45 % greater. Stable slopes (FoS = 4.3-5.27) are computed for all joint orientation conditions applied to the Parallel Deterministic of finite length and the Veneziano Joint network, the lowest of which is associated with J1. Very similar values are computed between the two joint networks for J2 and combined J1 and J2 (Figure 5.3).

For profile C, the Parallel Deterministic joint network of infinite length and the Ubiquitous Joint network produce similar safety factors for J1, but a difference of 37 % arises for J2 (Figure 5.3). Individual sets J1 and J2 indicate stable and unstable conditions respectively in both cases (Figure 5.3). Since kinematic analysis predicted wedge failure along the line of intersection of J1 and J2, and the orientation of this intersection was not incorporated into the numerical analyses, a comparison cannot be made. Stable conditions are calculated for joint orientation conditions applied as Parallel Deterministic of finite length and Veneziano Joint network (Figure 5.3). There is good agreement in values obtained between these two joint networks for all three joint orientation conditions (Figure 5.3).

Failure surfaces

For profile A, similar strain accumulation zones are achieved using the FEM with the Parallel Deterministic joint network of infinite length and the FDM with the Ubiquitous Joint network at an angle of 81° (J1), where maximum shear strain occurs midway down the dolerite dyke. The failure mechanism predicted by the FDM using the Ubiquitous Joint network with a dip of 57° (J3) correlates with the LEM of planar failure, where shallow planar failure surfaces developed along the bottom two benches. This failure mode is however not evident using the Parallel Deterministic joint network of infinite length with the FEM, where the maximum shear strain occurs in the centre and toe of the slope. By applying the combined sets J1 and J3 in this model, shear strain contours do not define a single sliding plane. However, there is an obvious sign of slip along J3. This is consistent with results of the kinematic analysis and LEM for wedge failure analysis, which indicated probable sliding along J3. For the Parallel Deterministic of finite length and Veneziano Joint network, maximum shear strain accumulation continues to be confined by

the contacts of the dolerite dyke, but the manifestation of a circular failure surface is also evident for all three joint orientation conditions, particularly for the Veneziano Joint network.

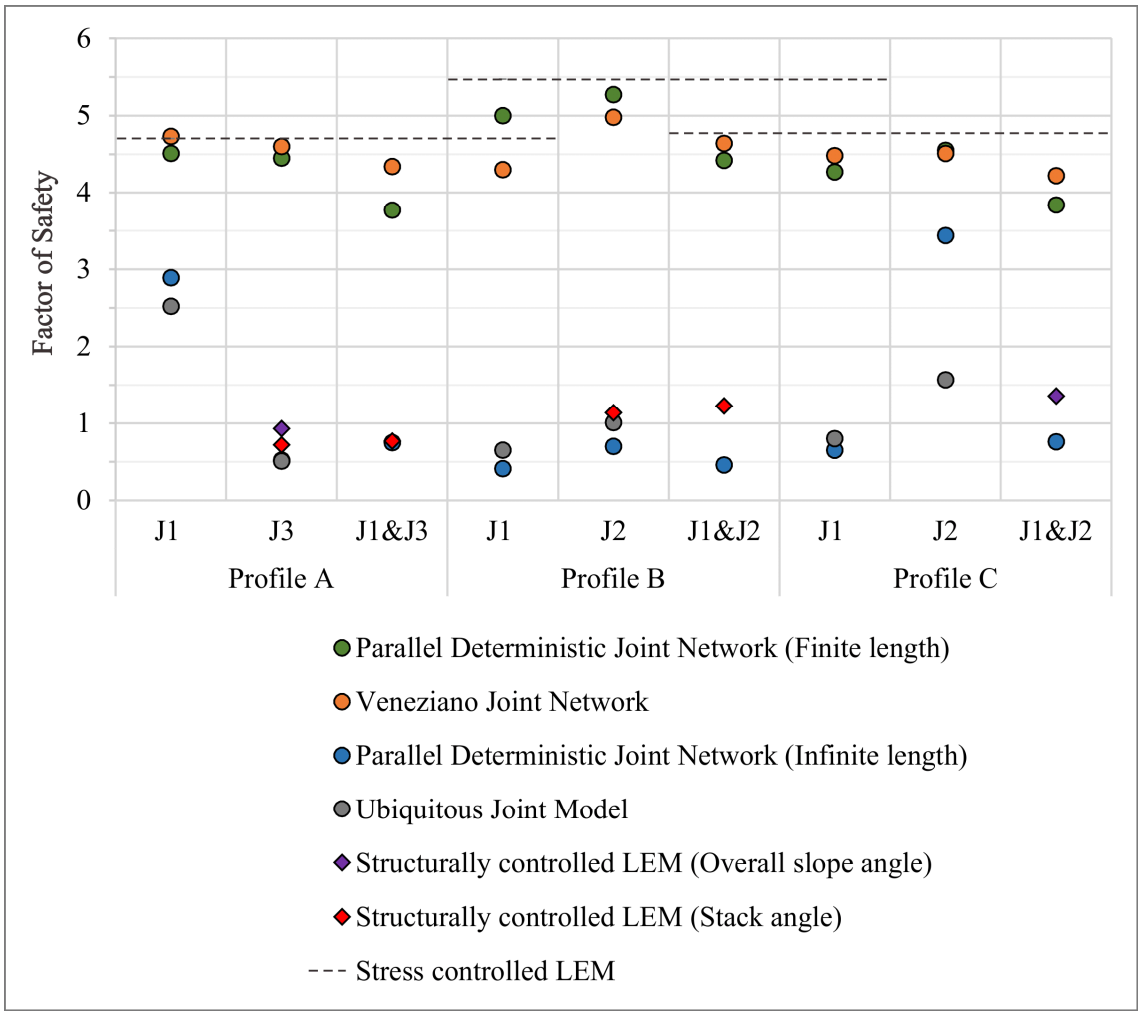

Figure 5.3. Safety factors produced for pseudo-discontinuum media using various joint networks.

For profile B, the resulting failure mode associated with J1, using the Ubiquitous Joint network, is planar failure along the uppermost bench. This finding does not coincide with results produced from the kinematic analysis and structurally controlled LEM, which predicted planar failure along J2. When applying J2 to the model however, shear strain contours form a large planar failure surface from tension cracks developed behind the crest to the toe of the slope, where the maximum strain accumulated, thus coinciding with the LEM for planar failure. This may also be associated with wedge sliding along J2, which was admissible to fail through the kinematic analysis at both overall and stack angle levels. With the application of J1, J2 and J1 and J2 combined in the FEM as Parallel Deterministic joint network of infinite length, there is no definitive failure mechanism. Shear strain accumulates in the centre of the profile and at the toe of the slope, with slip occurring along the respective joints and along J1 when combined. The resulting shear strain accumulation

associated with the Parallel Deterministic of finite length and Veneziano Joint network of J1 indicate deep set curved failure surfaces, which develop into less defined and more planar surfaces with the application of J2 and a combination of J1 and J2.

For profile C, the application of the J1 as the Ubiquitous Joint network of the FDM depicts strain accumulation along bench faces and strain contours extending into the slope to form potential toppling blocks. A different result is determined using the Parallel Deterministic joint network of infinite length, where strain accumulates in the centre and at the toe of the slope. Shear strain contours for J2 are however, comparable between the two joint networks, where the maximum strain accumulates within the dolerite intrusion. Similar failure surfaces are predicted using the Parallel Deterministic of finite length and the Veneziano Joint network, but with the addition of curved failure surfaces. These are less distinct using the latter joint network model, and also become less apparent when both joint sets are combined into a model.

It is clear that the Parallel Deterministic joint network of infinite length and Ubiquitous Joint network have a great effect the stability of slopes. According to Terzaghi (1962), a reduced spacing between continuous joints leads to these joints having an increasing influence on the stability of slopes. The intensely jointed profiles (spacing of 5 m) in relation to the scale of the slope could thus be the cause of reduced safety factors. It is also evident that the FDM, together with the Ubiquitous Joint network, performs best in terms of the simulation of failure mechanisms determined by structurally controlled LEMs. In reality however, most rock masses contain discontinuous joints, varying in persistence, length and spacing. The use of joint networks with the introduction of rock bridges indicate stable conditions. According to Terzaghi (1962), most cohesion in such jointed rock masses occurs in these gaps between disrupted joint planes. A shear failure along a plane comprising both joints and intact material is resisted by the combined effects of pressure-conditioned shearing resistance and the cohesion of the intact material. The developing near circular failure surfaces exhibited by most profiles using the Parallel Deterministic of finite length and Veneziano Joint network could be due to the intensity of jointing, where Bye and Bell (2001) stated that circular failures are possible in highly fractured rock masses, which could be considered to be randomly jointed and isotropic. Despite the fact that the presence of rock bridges could aid in stabilizing a rock slope, failure remains a possibility due to a potential buildup of shearing stresses resulting from an increasing slope height which may cause the gradual elimination of these rock bridges through their breakup thus causing a decrease in cohesion (Terzaghi, 1962). Tensile failure of intact rock bridges is typically the primary failure mode (Einstein et al., 1983; Einstein, 1993; Shen, 1993) followed by shear fracturing as the secondary mode (Sjöberg, 1999). With the advent of progressively more joints

becoming free to open, the distribution of normal stresses on joint walls gradually become irregular causing local stress accumulation on blocks located between these joints and eventually, their failure (Terzaghi, 1962).

5.3. Rockfall hazard analysis

Rockfall hazard analyses were conducted in two-dimensions (2D) and three-dimensions (3D) based on rigid body dynamics and across three profiles with increasingly adverse slope/cut slope topographies.

According to the findings of the 2D analyses, translational velocity and rotational, translational and total kinetic energy increases with an adverse change in slope geometry. The rotational energy and bounce height along moderate slope/cut slope topography however appears to be greater than that reached on poor slope/cut slope topography. Good slope/cut slope topography resulted in more frequent impacts than poor slope/cut slope topography, which is generally expected since good condition slopes represent the more elastic conditions.

The 3D analysis revealed that the velocity, and translational and total energy, increase considerably with an adverse change in slope geometry. The rotational energy is significantly lower than that obtained from the 2D analysis and the moderate slope/cut slope topography produced the highest value. Along a good slope/cut slope topography, the square box falling body travelled furthest downslope as opposed to the flat elongated box shape, which moved to the pit floor along the poor slope/cut slope topography. According to Basson (2012), flattened falling bodies are typically the easiest to stop by catch benches, as they tend to slide instead of roll. This is further confirmed by the flat cylinder, angular flat cylinder, flat box and flat elongated box shapes collecting at the first and second berms along good to moderate slope/cut slope topography, where continuous maintenance is required. Since catch bench widths become reduced and slope angles become inclined with an adverse change in slope geometry, conditions for sliding are more prevalent along poor slope/cut slope topographies, thus explaining why only the flat elongated box terminated at the pit floor. Along a moderate slope/cut slope topography, rounded shapes such as the perfect sphere and angular rough cylinder travelled furthest downslope, followed by those with sharp edges, namely the square box shape. It should also be noted that sharp corners could result in false bounces, especially if the falling bodies consist of few vertices and sharp corners, or if the fall bodies are large in relation to the polygons of the stationary slope geometry (Basson, 2012). Since the rockfall release points were designated

manually, it important to note that variability can arise in this regard. According to Kim et al. (2015), trajectory directions are particularly sensitive to surface geometry at the source area.

The investigation into the influence of a dynamic surface geometry, due to rock mass quality and slope design, on rockfall potential, confirmed that rock mass quality is a significant controlling factor. Findings also indicated that rock shapes have a significance influence on falling paths, which was also confirmed in field tests conducted by Kim et al. (2015).

Both models reveal that an adverse change in slope/cut slope topography conditions correspond to a progressive increase in slope smoothness, which in turn is related to an increase in falling velocity. It is evident that crest loss occurring from good to poor slope/cut slope topography strongly impacts on rockfall. Conspicuously high velocities are reached, which is most likely due to the topography in use. Agliardi and Crosta (2003) warned that when performing modelling using low-detail topography, one should expect to overestimate velocity, to underestimate the fly height, and to obtain less scattered values of the kinematic parameters for different computed trajectories. It is suggested that additional work be conducted in the form of back analysis in order to obtain more reliable and representative input parameters for rockfall analyses.

Energy along rockfall trajectories is considerably higher in 3D models than in 2D models for moderate and poor slope/cut slope topography, however energy curves tend to be of a similar nature. According to Kim et al. (2015), this can be attributed to the fact that the 2D code, RocFall (Rocscience Inc., 2015) commences movement with bouncing patterns while rocks in the 3D code, Trajec3D (BasRock, 2016) are initiated with a rolling pattern.

Energy changes occurring during a fall comprise a reduction in kinetic energy during impact as a result of compression and friction, followed by an increase in kinetic energy during the trajectory as a result of gravitational acceleration. The rotational energy will also change during impact, but will remain constant along the trajectory (Wyllie, 2015). When the velocity and energy lost during impact are less than the velocity and energy gained during the subsequent trajectory, the rock will continue to fall downslope. However, as the slope angle decreases such that the impacts occur at a steeper angle and the trajectories become shorter, the energy lost at the point of impact will be greater than the energy gained during the trajectory, and the falling block will come to a standstill (Wyllie, 2015).

CHAPTER 6

CONCLUSION

The major conclusions drawn from this research include the following:

- The estimation of equivalent Mohr-Coulomb strength parameters conforming to the non-linear Generalized Hoek-Brown failure criterion, based on a range of minor principal stress values, proved to be effective in terms of calculating comparable safety factors in all methods of analyses. Furthermore, analogous shear strain accumulation zones and shear strain values were found between the strength criteria using the FEM and FDM.
- Closely spaced joints with continuous or near-continuous joint lengths in continuum numerical models revealed that the stability of slopes is structurally controlled, where most safety factors were found to be below 1.5, and comparable to those of the predicted failure modes in the structurally controlled LEMs.
- Shear strain accumulation zones of the FDM depicts recognisable failure modes correlating to those of the LEMs, while the FEM portrays widely distributed strains with slippage along joints.
- Planar failure and/or wedge sliding is common at stack angle level, whereas planar and toppling modes are typically associated with overall pit slope angles.
- Potential toppling failure modes at overall pit slope angles are revealed in numerical analyses, along joint orientations which were not considered a problem in LEMs.
- The introduction of rock bridges along closely spaced and parallel discontinuity planes significantly enhances stability. A similar relationship is found with additional joint property variations (i.e. orientation, spacing, length). Due to the high degree of fracturing in relation to the profile scale, the failure surfaces described by the shear strain accumulations zones indicated approximately circular surfaces, which followed lines of least resistance.
- The 2D rockfall analyses showed an underperformance of all types of topographies, with circular shaped blocks reaching greatest velocities. The 3D analysis however, determined expected behaviour of falling blocks and showed how good slope/cut slope topography performs in terms of catching falling bodies at first and second benches, as opposed to the moderate and poor slope/cut slope topography, which permits movement to the bottom of the slope.

This study shows the importance of performing more than one type of analysis in assessing the stability of slopes. The LEM can give relevant information, but is recommended as an initial study

where results should be confirmed and/or enhanced through numerical modelling. Numerical modelling methods allow for a better understanding of material behaviour through the calculation of stresses and displacements, and are better suited to more complex conditions. These results, together with those of rockfall analyses, could be valuable in assessing methods of stabilising potentially hazardous zones in open pit mines.

References

Abbas, S. M. and Konietzky, H. H., 2015. Rock Mass Classification Systems. In: Konietzky, H. (Ed.), TU Bergakademie Freiberg, Geotechnical Institute, 1-43.

Abbaszadeh, M., Shahriar, K., Sharifzadeh, M. and Heydari, M., 2011. Uncertainty and Reliability Analysis Applied to Slope Stability: A Case Study from Sungun Copper Mine. Geotechnical and Geological Engineering 29 (4), 571-596.

Abramson, L.W., Lee, T.S., Sharma, S. and Boyce, G.M., 2002. Slope Stability and Stabilization Methods. 2nd Ed. Wiley, New York, 736 pp.

Agliardi, F. and Crosta, G., 2003. High resolution three-dimensional numerical modelling. International Journal of Rock Mechanics and Mining Sciences 40 (4), 455-471.

Alejano, L.R., Pons, B., Bastante, F.G., Alonso, F. and Stockhausen, H.W., 2007. Slope geometry design as a means for controlling rockfalls in quarries. International Journal of Rock Mechanics and Mining Sciences 44 (6), 903-921.

Amadei, B., Savage, W.Z. and Swolfs, H. S., 1987. Gravitational stresses in anisotropic rock masses. International Journal of Rock Mechanics and Mining Sciences and Geomechanics 24 (1), 5-14.

Azzoni, A. and de Freitas, M.H., 1995. Experimentally gained parameters, decisive rock fall analysis. Rock Mechanics and Rock Engineering 28 (2), 111-124.

Azzoni, A., La Barbera, G. and Zaninetti, A., 1995. Analysis and prediction of rockfalls using a mathematical model. International Journal of Rock Mechanics and Mining Sciences and Geomechanics 32 (7), 709-724.

Barton, N.R., 1971. A model study of the behaviour of steep excavated rock slopes. Unpublished PhD Thesis, University of London, Imperial College, 752 pp.

Barton, N.R., 1973. Review of a new shear strength criterion for rock joints. Engineering Geology 7 (4), 287-332.

Barton, N.R., 1976. The shear strength of rock and rock joints. International Journal of Rock Mechanics and Mining Sciences and Geomechanics 13 (9), 255-279.

Barton, N.R., 1987. Predicting the behaviour of underground openings in rock. Manuel Rocha Memorial Lecture, Lisbon. Norwegian Geotechnical Institution, Oslo.

BasRock, 2016. Trajec3D - Available from http://www.basrock.com/page13.htm - Beta version available as free download. [Available from: http://www.basrock.net/trajec3d].

Basson, F., 2012. Rigid body dynamics for rockfall trajectory simulation. Proceedings of the 46th U.S. Rock Mechanics/Geomechanics Symposium, Chicago, United States of America, American Rock Mechanics Association, 1438–1444.

Basson, F., Humphreys, R. and Temu, A., 2013. Coefficient of restitution for rigid body dynamics modelling from onsite experimental data. Proceedings of the 2013 International Symposium on Slope Stability in Open Pit Mining and Civil Engineering, Brisbane, Australia, Australian Centre for Geomechanics, 1161-1170.

Bieniawski, Z.T., 1973. Engineering classification of jointed rock masses. South African Institution of Civil Engineering 15 (12), 335-344.

Bieniawski, Z.T., 1976. Rock mass classification in rock engineering. Proceedings of the Symposium on Exploration for Rock Engineering. In: Bieniawski, Z. T. (Ed.), Balkema, Cape Town, 97-106.

Bieniawski, Z. T., 1989. Engineering Rock Mass Classifications. Wiley, New York, 251 pp.

Bishop, A.W., 1955. The use of the slip circle in the stability analysis of earth slopes. Geotechnique 5 (1), 7-17.

Blenkinsop, T.G., Martin, A., Jelsma, H.A. and Vinyu, M. L., 1997. The Zimbabwe Craton. In: de Wit, M.J., Ashwal, L. D. (Eds.), Greenstone belts. Oxford University Press, 567-580.

Brady, B.H.G. and Brown, E.T., 2005. Rock Mechanics for Underground Mining. 3rd Ed. Kluwer Academic Publishers, New York, 628 pp.

Bye, A.R. and Bell, F.G., 2001. Stability assessment and slope design at Sandsloot open pit, South Africa. International Journal of Rock Mechanics and Mining Sciences, 38 (3), 449-466.

Cai, M., 2008. Influence of stress path on tunnel excavation response – Numerical tool selection and modelling strategy. Tunneling and Underground Space Technology 23 (6), 618-626.

Cai, M., Kaiser, P.K., Uno, H., Tasaka, Y. and Minami, M., 2004. Estimation of rock mass deformation modulus and strength of jointed hard rock masses using GSI system. International Journal of Rock Mechanics and Mining Sciences, 41 (1), 3-19.

Charalambous, A. and Sakellariou, M., 2007. GIS-Based Rockfall Hazard Assessment in Support of Decision Making. Rockfall–Mechanism and Hazard Assessment, Lisbon, 1-5.

Cheng, Y.M., and Lau, C.A., 2008. Slope stability analysis and stabilization: New methods and insights. Routledge, New York, pp. 260.

Cheng, Y.M., Lansivaara, T. and Wei, W.B., 2007. Two-dimensional slope stability analysis by limit equilibrium and strength reduction methods. Computers and Geotechnics 34 (3), 137-150.

Cicchini, P.F., Ryan, T.M. and Barkley, R.C., 2001. Managing and Analyzing Overall Pit Slopes. In: Hustrulid, W.A., McCarter, M.K. and Van Zyl, D.J.A. (Eds.), Slope stability in surface mining. Society for Mining, Metallurgy and Exploration, Littleton, 39-46.

Coggan, J. S., Stead, D., and Eyre, J. M., 1998. Evaluation of techniques for quarry slope stability assessment. Transactions of the Institution of Mining and Metallurgy. Applied Earth Science 107, 139-147.

Crosta, G.B. and Agliardi, F., 2004. Parametric evaluation of 3D dispersion of rockfall trajectories. Natural Hazards and Earth System Science 4 (4), 583-598.

Crosta, G., and Locatelli, C., 1999. Approccio alla valutazione del rischio da frane per crollo. In: Orombelli (Ed.), Studi geografici e geologici in onore di Severino Belloni. Genova, Glauco Brigatti, 25-86.

Dawson, E.M., Roth, W.H. and Drescher, A., 1999. Slope stability analysis by strength reduction. Geotechnique 49 (6), 835-840.

Deere, D.U., 1964. Technical description of rock cores. Rock Mechanics and Engineering Geology, 1 (1), 16–22

Deere, D. U., 1968. Geological Considerations. In: Stagg, K.G. and Zienkiewicz, O.C. (Eds.), Rock mechanics in engineering practice. Wiley, London, 1-20.

Deere, D.U. and Miller, R.P., 1966. Engineering classification and index properties of rock. Research and Technology Division, Air Force Weapons Laboratory, Air Force Systems Command, Kirtland Air Force Base, New Mexico, Technical Report, AFWL-TR-65-116, 1-301.

Dershowitz, W. S., and Einstein, H. H., 1988. Characterizing rock joint geometry with joint system models. Rock Mechanics and Rock Engineering 21 (1), 21-51.

Dershowitz, W., 1985. Rock Joint Systems. Unpublished PhD. Thesis, Massachusetts Institute of Technology, Cambridge, 1-764.

Dong-Ping, D., Liang, L., Jian-Feng, W. and Lian-Heng, Z., 2016. Limit equilibrium method for rock slope stability analysis by using the Generalized Hoek–Brown criterion. International Journal of Rock Mechanics and Mining Sciences, 89, 176-184.

Duncan J. M., 1996. State of the art: Limit equilibrium and finite element analysis of slopes. Journal of Geotechnical Engineering 122 (7), 577-596.

Duncan, J. M., and Wright, S. G., 1980. The accuracy of equilibrium methods of slope stability analysis. Engineering Geology 16 (1-2), 5-17.

Eberhardt, 2014. The Hoek–Brown Failure Criterion. *In* The ISRM Suggested Methods for Rock Characterization, Testing and Monitoring: 2007-2014, Springer International Publishing, pp. 233-240.

Eberhardt, E. and Woo, K., 2015. Transitioning from Open Pit to Underground Mass Mining: Meeting the Rock Engineering Challenges of Going Deeper. International Society for Rock Mechanics, Proceedings of the 13th ISRM International Congress of Rock Mechanics, Montreal, Canada, 421-434.

Einstein, H.H., 1993. Modern Developments in Discontinuity Analysis: The Persistence-Connectivity Problem. In: Hudson, J.A. (Ed.), Comprehensive Rock Engineering. Principles, Practice and Projects. Volume 3: Rock Testing and Site Characterization, Oxford: Pergamon Press, 193-213.

Einstein, H.H., Veneziano, D., Beacher, G.B. and O'Reilly, K.J., 1983. The effect of discontinuity persistence on rock slope stability. International Journal of Rock Mechanics and Mining Sciences and Geomechanics 20 (5), 227-236.

Elburg, M. and Goldberg, A., 2000. Age and geochemistry of Karoo dolerite dykes from northeast Botswana. Journal of African Earth Sciences 31 (3-4), 539-554.

El-Ramly, H., Morgenstern, N.R. and Cruden, D.M., 2002. Probabilistic slope stability analysis for practice. Canadian Geotechnical Journal 39 (3), 665-683.

Fellenius, W. K. A., 1927. Erdstatische Berechnungen mit Reibung und Kohäsion (Adhäsion) und unter Annahme kreiszylindrischer Gleitflächen. Berlin, W. Ernst and Sohn. http://catalog.hathitrust.org/api/volumes/oclc/18623301.html.

Fillion, M.H. and Hadjigeorgiou, J., 2015. Implications of collected additional data on the slope design in an open pit operation. Journal of the Southern African Institute of Mining and Metallurgy 116 (5), 357-366.

Fisher, R., 1953. Dispersion of a Sphere. Proceedings of the Royal Society of London 217 (1130), 295-305.

Fookes, P. G., 1997. Geology for Engineers: The geological model, prediction and performance. Quarterly Journal of Engineering Geology and Hydrogeology 30 (4), 293-424.

Fossen, H., 2016. Structural Geology. 2nd Ed. Cambridge, United Kingdom, 524.

Fredlund, D.G., 1975. A comprehensive and flexible slope stability program. Association of Canada Meeting, Calgary 3, 109-142.

Fredlund, D.G. and Krahn, J., 1977. Comparison of slope stability methods of analysis. Canadian Geotechnical Journal 14 (3), 429-439.

Fredlund, D.G., Krahn, J. and Pufahl, D.E., 1981. The relationship between limit equilibrium slope stability methods. Proceedings of the International Conference on Soil Mechanics and Foundation Engineering 3, 409-416.

Gall, B.L., Tshoso, G., Dyment, T., Kampunzu, A.B., Jourdan, F., Fraud, D., Bertrand, H., Aubourg, C. and Vétel, W., 2005. The Okavango giant mafic dyke swarm (NE Botswana): Its structural significance within the Karoo Large Igneous Province. Journal of Structural Geology 27 (1), 2234-2255.

Gall, B.L., Tshoso, G., Jourdan, G.F., Féraud, G., Bertrand, H., Tiercelin, J.J., Kampunzu, A.B., Modisi, M P., Dyment, J. and Maia, M., 2002. 40Ar/39Ar geochronology and structural data from the giant Okavango and related mafic dyke swarms, Karoo Igneous Province, Botswana. Earth and Planetary Science Letters 202 (3-4), 595-606.

Gang, L., Hong, L., Harumi, K. and Yoshiaki, M., 2003. Application of ubiquitous joint model in numerical modelling of Hilltop Mines in Japan. Chinese Journal of Rock Mechanics and Engineering 22 (6), 951-956.

Giacomini, A., Thoeni, K., Lambert, C., Booth, S. and Sloan, S. W., 2012. Experimental study on rockfall drapery systems for open pit highwalls. International Journal of Rock Mechanics and Mining Sciences 56, 171-181.

Giani, G.P., 1992. Rock slope stability analysis. Balkema, Rotterdam, pp. 361.

Goodman, R.E., 1989. Introduction to Rock Mechanics, 2nd Ed. Wiley, New York, pp. 576.

Goodman, R.E. and Bray, J., 1976. Toppling of rock slopes. ASCE, Proceedings Specialty Conference on Rock Engineering for Foundations and Slopes, Boulder, 34-201.

Goudie, A.A. and Viles, H.V., 2016. Geomorphology in the Anthropocene. Cambridge University Press, Cambridge.

Griffiths, D.V. and Lane, P.A., 1999. Slope stability analysis by finite elements. Geotechnique 49 (3), 387-403.

Guzetti, F., Crosta, G., Setti, R. and Agliardi, F., 2002. STONE: A computer simulation program for three-dimensional simulation of rock-falls. Computers and Geosciences 28 (9), 1079-1093.

Hacking, I., 1975. The Emergence of Probability: The Emergence of Probability: A Philosophical Study of Early Ideas about Probability, Induction and Statistical Inference. 2nd Ed. Cambridge University Press, Cambridge, pp. 209.

Haimson, B., and Bobet, A., 2014. Introduction to Suggested Methods for Failure Criteria. In: Ulusay, R. (Ed.), The ISRM suggested methods for rock characterization, testing and monitoring: 2007-2014. Springer: Heidelberg, pp. 293.

Hammah, R. E., and Yacoub, T., 2009. Variation of Failure Mechanisms of Slopes in Jointed Rock Masses with Changing Scale. In: Diederichs, M. and Grasselli, G. (Ed.), Proceedings of the 3rd CANUS Rock Mechanics Symposium, Toronto, pp. 8.

Hammah, R. E., Curran, J. H., Yacoub, T. E., and Corkum, B. C., 2004. Stability Analysis of Rock Slopes using the Finite Element Method. Proceedings of the ISRM Regional Symposium EUROCK 2004 and the 53rd Geomechanics Colloquy, Salzburg, Austria.

Hammah, R. E., Yacoub, T. E., Corkum, B. C., and Curran, J. H., 2005. The shear strength reduction method for the Generalized Hoek-Brown Criterion. In Proceedings of the 40th U.S. Symposium on Rock Mechanics (USRMS): Rock Mechanics for Energy, Mineral and Infrastructure, Anchorage, Alaska, pp. 6.

Heyman, J. 1972. Coulomb's Memoir on Statics. Cambridge University Press, (reprinted by Imperial College Press 1998).

Hochbaum, D.S. and Chen, A., 2015. Performance Analysis and Best Implementations of Old and New Algorithms for the Open-Pit Mining Problem. Operations Research 48 (6), 894-914.

Hoek, E., n.d. Rocscience Online FAQ's. For Plastic Analysis, How Do I Estimate The Residual Value Of The Parameter Mi? [Online comments]. Response posted to https://support.rocscience.com/hc/en-us/articles/206734737-For-plastic-analysis-how-do-I-estimate-the-residual-value-of-the-parameter-mi-.

Hoek, E., 1994. Strength of rock and rock masses. International Society for Rock Mechanics, News Journal 2 (2), 4-16.

Hoek, E., 1999. Putting numbers to geology - an engineer's viewpoint. Quarterly Journal of Engineering Geology and Hydrogeology 32 (1), 1-19.

Hoek, E., 2007. Practical Rock Engineering. Rocscience, pp. 341.

Hoek, E. and Bray, J.W., 1981. Rock Slope Engineering, Revised 3rd Ed. The Institution of Mining and Metallurgy, London, pp 341-351.

Hoek, E. and Brown, E.T., 1980a. Empirical strength criterion for rock masses. Journal of the Geotechnical Engineering Division 106, 1013-1035.

Hoek, E, and Brown, E.T., 1980b. Underground Excavations in Rock. Institution of Mining Metallurgy, London, pp. 527.

Hoek, E. and Brown, E.T., 1988. The Hoek-Brown failure criterion. Proceedings of the 15th Canadian Rock Mechanic Symposium. In: Curran, J. C. (Ed.), Department of Civil Engineering, University of Toronto, 31-38.

Hoek, E. and Brown, E.T., 1997. Practical estimates of rock mass. International Journal of Rock Mechanics and Mining Sciences 34 (8), 1168-1186.

Hoek, E, and Marinos, P., 2000. Predicting tunnel squeezing problems in weak heterogeneous rock masses. Tunnels and Tunnelling International, pp. 22.

Hoek, E., Carranza-Torres, C. and Corkum, B., 2002. Hoek-Brown Failure Criterion, Proceedings of the North American Rock Mechanics Society Meeting, Toronro, Canada, 273-267.

Hoek, E., Grabinsky, M. W., and Diederichs, M. S., 1991. Numerical modelling for underground excavation design. Transactions of the Institution of Mining and Metallurgy, Section A: Mining Industry 100, A22-A30.

Hoek, E., Kaiser P.K., and Bawden, W.F., 1995. Support of Underground Excavations in Hard Rock. Balkema, Rotterdam, pp. 225.

Hoek, E., Marinos, P., and Benissi, M., 1998. Applicability of the Geological Strength Index (GSI) classification for very weak and sheared rock masses. The case of the Athens Schist Formation. Bulletin of Engineering Geology and the Environment 57 (2), 151-60.

Hoek, E., Rippere, K. H., and P. F. Stacey, P. F., 2001. Large-Scale Slope Designs. A Review of the State of the Art. In: Hustrulid, W. A., McCarter, M. K., and Van Zyl, D. J. A. (Eds.), Slope stability in surface mining. Society for Mining, Metallurgy and Exploration, Littleton, pp. 3-10.

Hoek, E., Wood, D., and Shah, S., 1992. A modified Hoek–Brown criterion for jointed rock masses. Proceedings of the Rock Characterization, Symposium International Society of Rock Mechanics- Eurock. In: Hudson, J. A. (Ed.), Britain Geotechnical Society, London, pp. 14-209.

Hoek, E., 1983. Strength of jointed rock masses, 23rd. Rankine Lecture. Géotechnique 33 (3), 187-223.

Hudson, J.A. and Harrison, J.P., 1997. Engineering Rock Mechanics: An introduction to the principles. Elsevier Science, Oxford, pp. 444.

Hungr, O., and Evans, S. G., 1988. Notes on dynamic analysis of flowslides. Landslides 1, 679-683.

International Society for Rock Mechanics (ISRM). 1981. Rock Characterization, Testing and Monitoring; ISRM Suggested Method. Pergamon Press, Oxford, pp. 211.

Itasca, 2011. Itasca Software Products - FLAC, FLAC3D, UDEC, 3DEC, PFC, PFC3D. Itasca Consulting Group Inc., Minneapolis.

Jaeger, J. C., and Cook, N. G., 1979. Fundamentals of Rock Mechanics. Chapman and Hall, London, pp. 593.

Jakubec, J., Terbrugge, P.J., Guest, A.A. and Ramsden, F., 2001. Pit Slope Design at Orapa Mine. In: Hustrulid, W.A., McCarter, M.K., and Van Zyl, D.J.A. (Eds.), Slope stability in surface mining. Society for Mining, Metallurgy and Exploration, Littleton, pp. 227-238.

Janbu, N., 1968. Slope stability computations, soil mechanics and foundation engineering report. The Technical University of Norway, Trondheim.

Janbu, N., 1954. Application of composite slip surfaces for stability analysis. Proceedings of the European conference on stability of earth slopes, Stockholm, 3, 43-49.

Janbu, N., Bjerrum, L., and Kjaernsli , B., 1956. Stability calculations for fillings, cuts and natural slopes. Oslo, Norway.

Jimenez-Rodriguez, R., Sitar, N., and Chacon, F., 2006. System reliability approach to rock slope stability. International Journal of Rock Mechanics and Mining Sciences 43 (6), 847-859.

Kim, D.H., Gratchev, I., Berends, J. and Balasubramaniam, A., 2015. Calibration of restitution coefficients using rockfall simulations based on 3D photogrammetry model: a case study. Natural Hazards 78 (3), 1931-1946.

Kliche, C.A., 1999. Rock slope stability. Colorado, United States of America. Society for Mining, Metallurgy, and Exploration, Inc., pp 273.

Labuz, J.F. and Zang, A., 2012. Mohr–Coulomb failure criterion. In The ISRM Suggested Methods for Rock Characterization, Testing and Monitoring: 2007-2014, Springer International Publishing, pp. 227-231.

Lorig, L., and Varona, P., 2001. Practical Slope-Stability Analysis Using Finite-Difference Codes. In: Hustrulid, W. A., McCarter, M. K., and Van Zyl, D. J. A. (Eds.), Slope stability in surface mining. Society for Mining, Metallurgy and Exploration, Littleton, pp. 115-124.

Lowe, J. and Karafiath, L., 1960. Stability of earth dams upon drawdown. Proceedings of the 1st. Pan-American Conference on Soil Mechanics and Foundation Engineering, México 2, 537-552.

Lusty, P.A.J. and Gunn, A.G., 2015. Challenges to global mineral resource security and options for future supply. Geological Society, London, Special Publications 393, 265-276.

Marinos, P, and Hoek, E., 2000. GSI – A geologically friendly tool for rock mass strength estimation. Proceedings GeoEng2000 Conference, Melbourne, pp. 1422-1442.

Marinos, P., and Hoek, E., 2001. Estimating the geotechnical properties of heterogeneous rock masses such as flysch. Bulletin of the International Association of Engineering Geology 60 (2), 85-92.

Markland, J.T., 1972. A useful technique for estimating the stability of rock slopes when the rigid wedge sliding type of failure is expected. Imperial College Rock Mechanics. Research Report 19, 10 pp.

Matsui, T., and San, K., 1992. Finite Element slope stability analysis by shear strength reduction technique. Soils and Foundations 32 (1), 59-70.

Moradi, A. and Hosseinitoudeshki, V., 2015. The effect of joint models on the stability of rock slopes. International Journal of Geology, Agriculture and Environmental Sciences 3 (1), 7-10.

Morgenstern, N.R. and Price, V.E., 1965. The analysis of the stability of general slip surfaces. Géotechnique 15, 79-93.

Muller, J., 1979. Contributions to engineering geology and slope movement investigations. In: Voight, B. (Ed.), Rockslides and Avalanches, Elsevier, New York, pp. 95-109.

Nadai, A., 1950. Theory of Flow and Fracture of Solids. Vol, 1st Ed. McGraw-Hill, New York, pp. 347-352.

Palisade, 1997. @RISK, Risk Analysis and Simulation Ad-In for Microsoft Excel, Palisade Corporation, New York, [Free Trail Version 7.5 available from: http://www.palisade.com/risk/].

Peckover, F.L. and Kerr, J.W.G., 1977. Treatment and maintenance of rock slopes on transportation routes. Canadian Geotechnical Journal 14 (4), 487-507.

Pfeiffer, T. and Bowen, T., 1989. Computer simulation of rockfall. Environmental and Engineering Geoscience 26 (1), 135-146.

Pierson, L., Davis, S.A. and Van Vickle, R., 1990. The rockfall hazard rating system, Implementation manual. Technical Report No. FHWA-OR-EG-90-01, Washington, DC.

Read, J., and Stacey, P., 2009. Guidelines for open pit slope design. CSIRO Publishing, Australia, pp 551.

Rocscience Inc., 2015. Rocscience software Suite – RocData, Dips, RocFall, Swedge, RocPlane, RocTopple, Slide, Phase2. Rocscience Inc., Toronto.

Rocscience Inc., 2016. Online Help Manual: Phase2 support. [online]. Available from: https://www.rocscience.com/help/phase2/webhelp9/phase2.htm. [Accessed 17 October 2016].

Schlüter, T., 2006. Geological Atlas of Africa - With Notes on Stratigraphy, Tectonics, Economic Geology, Geohazards and Geosites of Each Country. Springer-Verlag, Germany, pp. 272.

Shen, B. 1993. Mechanics of Fractures and Intervening Bridges in Hard Rocks. Unpublished PhD Thesis, Royal Institute of Technology, Division of Engineering Geology, Stockholm, pp. 156.

Sheorey, P.R., 1997. Empirical Rock Failure Criteria. Balkema, Rotterdam, pp. 176.

Shukha, R. and Baker, R. 2003. Mesh geometry effects on slope stability calculation by FLAC strength reduction method – linear and non-linear failure criteria. In: Brummer, R., Andrieux, P., Detournay, C. and Hart, R. (Eds.), FLAC and Numerical Modelling in Geomechanics, Proceedings of the Third International FLAC Symposium, Sudbury, Canada, pp. 109-116.

Singh, T.N., Singh, R., Singh, B., Sharma, L.K., Singh, R. and Ansari, M. L., 2016. Investigations and stability analyses of Malin village landslide of Pune district, Maharashtra, India. Natural Hazards 81 (3), 2019-2030.

Singh, V.K., Pradad, M. and Dhar, B.B., 1994. Stability analysis of an open pit mine by numerical modelling. Journal of Mines, Metals and Fuels 42, 39-46.

Sjöberg J., 1999. Analysis of large scale slopes. Unpublished PhD Thesis, Lulea University of Technology, Lueå, pp. 682.

Sjöberg, J., 1996. Large Scale Slope Stability in Open Pit Mining - A Review. Technical Report, Division of Rock Mechanics, Luleå University of Technology, Sweden, pp. 229.

Sjöberg, J., 2001. Failure Mechanisms for High Slopes in Hard Rock. In: Hustrulid, W.A., McCarter, M. K., and Van Zyl, D. J. A, (Eds.), Slope stability in surface mining. Society for Mining, Metallurgy and Exploration, Littleton, pp. 71-80.

Soren, K., Budi, G. and Sen, P., 2014. Stability analysis of open pit slope by finite difference method. International Journal of Research in Engineering and Technology 3 (5), 326-334.

Spencer, E., 1967. A method of analysis of the stability of embankments assuming parallel inter-slice forces. Géotechnique 17 (1), 11-26.

Stacey, T.R., Xianbin, Y., Armstrong, R. and Keyter, G.J., 2003. New slope stability considerations for deep open pit mines. The Journal of the South African Institute of Mining and Metallurgy 103 (6), 373-389.

Stead, D., Eberhardt, E. and Coggan, J. S., 2006. Developments in the characterization of complex rock slope deformation and failure using numerical modelling techniques. Engineering Geology 83 (1-2), 217-235.

Stead, D., Eberhardt, E., Coggan, J. and Benko, B., 2001. Advanced numerical techniques in rock slope stability analysis – applications and limitations. In: International Conference on Landslides—Causes, Impacts and Countermeasures, Davos, Switzerland, pp. 615-624

Taylor, D.W., 1937. Stability of earth slopes. Boston Society of Civil Engineers 24, 197-246.

Terzaghi, K., 1962. Stability of Steep Slopes on Hard Unweathered Rock. Géotechnique 12 (4), 251-270.

Tharp, T. M., and Coffin, D. T., 1985. Field Application of Fracture Mechanics Analysis to Small Rock Slopes. Proceedings of the 26th U.S. Symposium on Rock Mechanics (USRMS), South Dakota. American Rock Mechanics Association, pp. 667-674.

Tieblemont, D., 2016. Geological map of Africa at 1:10M scale, CGMW-BRGM.

Ulusay, R., 2013. Harmonizing engineering geology with rock engineering on stability of rock slopes. In: Feng, X., Hudson, J. A., and Tan, F. (Eds.), Rock characterisation, modelling and engineering design methods. CRC Press, Taylor and Francis Group, pp. 932.

Ulusay, R. and Hudson, J.A., 2014. Suggested Methods for Rock Failure Criteria: General Introduction. In: Ulusay, R. (Ed.), The ISRM suggested methods for rock characterization, testing and monitoring: 2007-2014. Springer, Heidelberg, pp. 293.

United Nations 2015. World Population Prospects: The 2015 Revision, Key Findings and Advance Tables. Department of Economic and Social Affairs, Population Division, United Nations, New York, pp. 66.

Valdivia, C. and Lorig, L., 2001. Slope Stability at Escondida Mine. In: Hustrulid, W.A., McCarter, M.K. and Van Zyl, D.J.A. (Eds.), Slope stability in surface mining. Society for Mining, Metallurgy and Exploration, Littleton, pp. 153-162.

Veneziano, D., 1978. Probabilistic model of joints in rock. Unpublished manuscript, Massachusetts Institute of Technology, Cambridge, Massachusetts.

Verma, D., Kainthola, A., Thareja, R., and Singh, R. N., 2013. Stability Analysis of an Open Cut Slope in Wardha Valley Coal Field. Journal Geological Society of India 81 (6), 804-812.

Walton, S., Hassan, O., Morgan, K. and Brown, M.R., 2011. Modified cuckoo search: A new gradient free optimisation algorithm. Chaos, Solitons and Fractals: Nonlinear Science, and Nonequilibrium and Complex Phenomena 44 (9), 710-718.

Wang, T. and Huang, T., 2009. A constitutive model for the deformation of a rock mass containing sets of ubiquitous joints. International Journal of Rock Mechanics and Mining Sciences 46 (3), 521-530.

Wen, A., Sturzenegger, M. and Stead, D., 2014. Analysis of a Complex Rock Slope Instability with a Stepped Failure Surface using Discrete Fracture Network Models. Proceedings of the International Discrete Fracture Network Engineering Conference, Vancouver, Canada, pp. 8.

Whitman, R.V. and Bailey, W.A., 1967. Use of computers for slope stability analysis. Journal of Soil Mechanics and Foundations Division 93, 475-498.

Wyllie, D.C. and Mah, C. W., 2004. Rock slope engineering: Civil and mining. 4th Ed. Taylor and Francis Group, New York, pp. 456.

Wyllie, D.C., 2015. Rock Fall Engineering. CRC Press, Taylor and Francis Group: Florida

Zhang, L., 2016. Engineering Properties of Rock. 2nd Ed. Elsevier, Oxford, pp. 394.

Zheng, J., Liu, D.F. and Li, C.G., 2008. On the assessment of failure in slope stability analysis by the finite element method. Rock Mechanics and Rock Engineering 41 (4), 629-639.

Zheng, H., Liu, D.F. and Li, C., 2005. Slope stability analysis based on elasto-plastic finite element method. International Journal for Numerical Methods in Engineering, 64 (14), 1871-1888.

Zienkiewicz, O.C., Humpheson, C. and Lewis, R. W., 1975. Associated and non-associated visco-plasticity and plasticity in soil mechanics. Géotechnique 25 (4), 671-689.

APPENDIX A – ROCK MASS CLASSIFICATION SYSTEMS

Table 1. The Rock Mass Rating System (Geomechanics Classification of Rock Masses) (Bieniawski, 1989)

A.CLASSIFICATION PARAMTERS AND THEIR RATINGS									
Parameter			Ranges of Values						
1	Strength of intact rock material	Point-load strength index (MPa)	>10	4 – 10	2 – 4	1 – 2	For this low range, uniaxial compressive test is preferred		
		Uniaxial compressive strength (MPa)	>250	100 - 250	50 - 100	25 - 50	5 - 25	1 - 5	<1
	Rating		15	12	7	4	2	1	0
2	Drill core quality RQD (%)		90 - 100	75 - 90	50 - 75	25 - 50	<25		
	Rating		20	17	13	8	3		
3	Spacing of discontinuities		>2 m	0.6 – 2 m	200 – 600 mm	60 – 200 mm	<60 mm		
	Rating		20	15	10	8	5		
4	Condition of discontinuities		Very rough surfaces Not continuous No separation Unweathered wall rock	Slightly rough surfaces Separation <1 mm Slightly weathered walls	Slightly rough surfaces Separation <1 mm Highly weathered walls	Slickensided-surfaces or Gouge <5 mm thick or Separation 1 – 5 mm Continuous	Soft gouge >5 mm thick or Separation >5 mm Continuous		
	Rating		30	25	20	10	0		
5	Groundwater	Inflow per 10 m tunnel length	None	<10	10 - 25	25 - 125	>125		
		Ratio $\frac{Joint\ water\ pressure}{Major\ principal\ stress}$	0	<0.1	0.1 – 0.2	0.2 – 0.5	>0.5		
		General conditions	Completely dry	Damp	Wet	Dripping	Flowing		
	Rating		15	10	7	4	0		
B. RATING ADJUSTMENT FOR DISCONTINUITY ORIENTATIONS									
	Strike and Dip Orientations of Discontinuities		Very Favourable	Favourable	Fair	Unfavourable	Very Unfavourable		
Ratings		Tunnels	0	-2	-5	-10	-12		
		Foundations	0	-2	-7	-15	-25		
		Slopes	0	-5	-25	-50	-60		

Parameter	Ranges of Values				
C. ROCK MASS CLASSES DETERMINED FROM TOTAL RATINGS					
Rating	100 - 81	80 - 61	60 - 41	40 - 21	<20
Class no.	I	II	III	IV	V
Description	Very goof rock	Good rock	Fair rock	Poor rock	Very poor rock
D. MEANING OF ROCK MASS CLASSES					
Class no.	I	II	III	IV	V
Average stand-up time	20 yr for 15 m span	1 yr for 10 m span	1 wk for 5 m span	10 h for 2.5 m span	30 min for 1 m span
Cohesion of the rock mass (kPa)	>400	300 - 400	200 - 300	100 - 200	<100
Friction angle of the rock mass (degree)	>45	35 - 45	25 - 35	15 - 25	>15

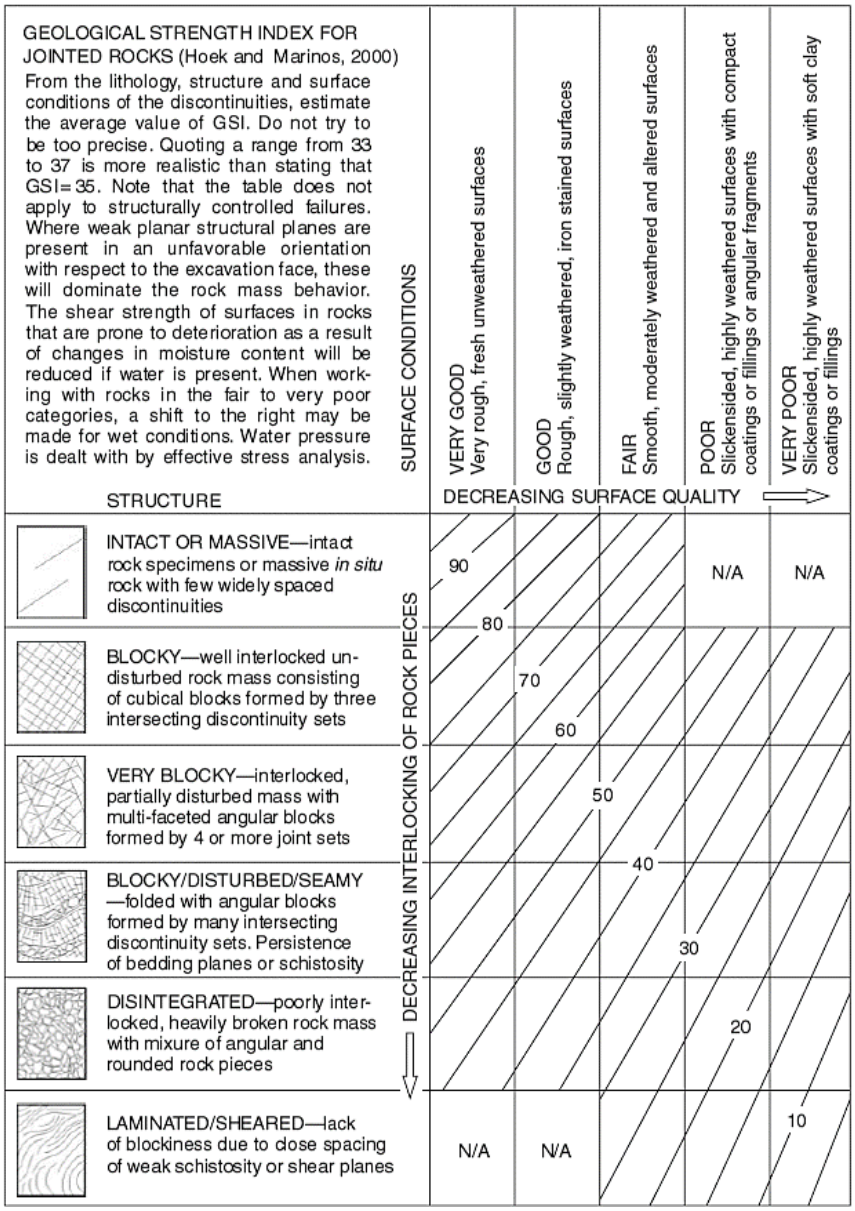

Figure 1. Geological strength index for blocky jointed rock masses (Hoek and Marinos, 2000).

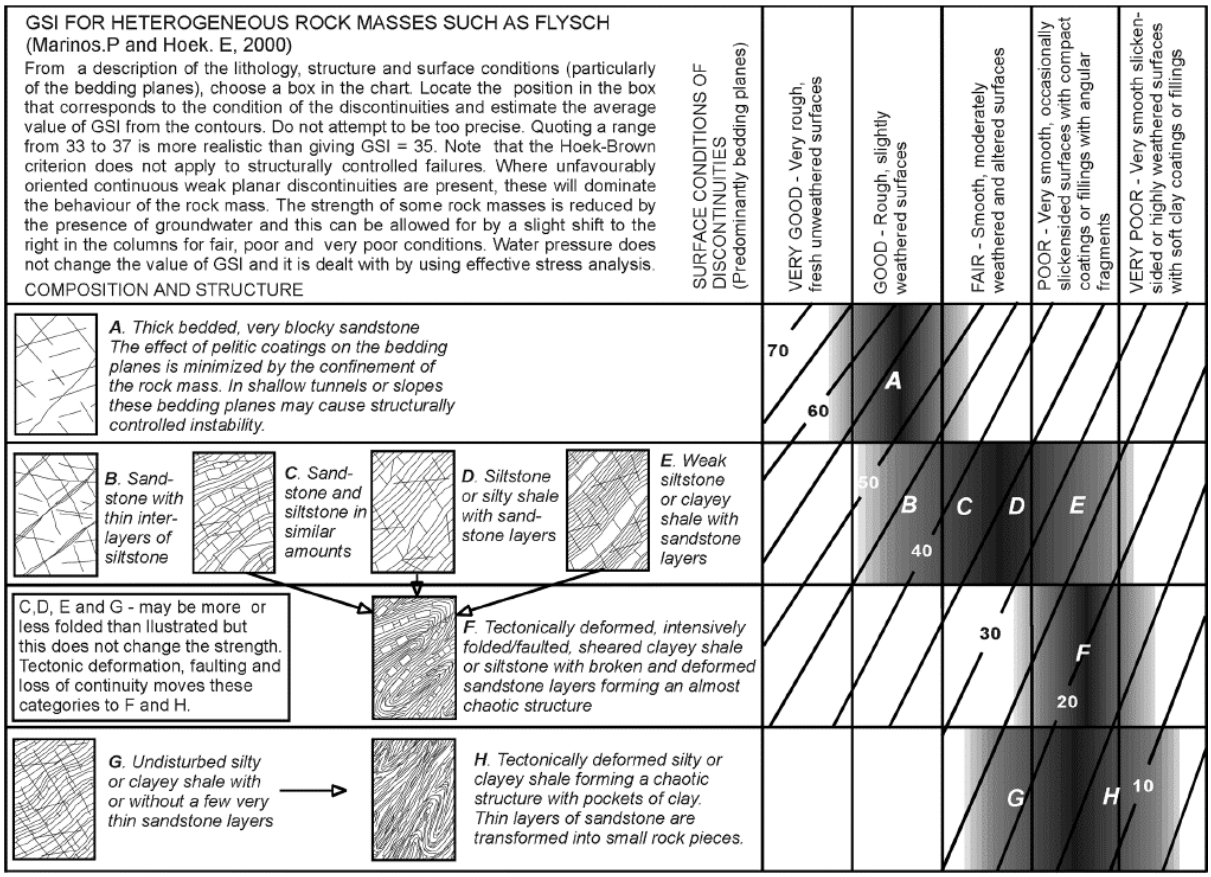

Figure 2. Geological Strength Index estimates for heterogeneous rock masses such as flysch (Marinos and Hoek, 2000)

APPENDIX B – STRENGTH PROPERIES

Table 1. Triaxial test results for metagabbro samples (Consultants A, 1996 and B, 2006).

σ_3 (MPa)	σ_1 (MPa)	Rock type	Reference
0	138.8	Metagabbro	2005
10	431.2	Metagabbro	2005
20	332.1	Metagabbro	2005
30	413.4	Metagabbro	2005
0	274.8	Metagabbro	1996
0	351.1	Metagabbro	1996
0	297.5	Metagabbro	1996
5	379.2	Metagabbro	1996
5	344.9	Metagabbro	1996
5	361.2	Metagabbro	1996
10	341.7	Metagabbro	1996
10	347.3	Metagabbro	1996
10	394.8	Metagabbro	1996
15	425.3	Metagabbro	1996
15	417.3	Metagabbro	1996
15	425.1	Metagabbro	1996
0	217	Tonalite	1996
10	385	Tonalite	1996
20	507	Tonalite	1996
30	576	Tonalite	1996
0	249.5	Tonalite	2005
0	243.6	Tonalite	2005
0	200.3	Tonalite	2005
10	244.8	Tonalite	2005
10	279	Tonalite	2005

Barton Shear Failure Criterion

Input parameters

Basic friction angle (PHIB): 37.1°

Joint roughness coefficient (JRC): 9.4

Joint compressive strength (JCS): 200

Minimum normal stress (SIGNMIN): 0.336 MPa

Table 2. Barton Shear Failure Criterion (Consultant D, 2011).

Normal stress (SIGN) MPa	Shear strength (TAU) MPa	dTAU/dSIGN (DTDS)	Friction angle (PHI) °	Cohesive strength (COH) MPa
0.27	0.555	1.684	59.30	0.101
0.42	0.799	1.573	57.56	0.138
1.68	2.549	1.282	52.04	0.395
2.52	3.593	1.210	50.42	0.545
3	4.166	1.180	49.72	0.626
4	5.322	1.133	48.57	0.789
5	6.437	1.098	47.67	0.947
6	7.520	1.070	46.94	1.099

Cell formulae:

SIGNMIN = 10^(LOG(JCS)-((70-PHIB)/JRC))
TAU = SIGN*TAN((PHIB+JRC*LOG(JCS/SIGN))*PI()/180)
DTDS = TAN((JRC*LOG(JCS/SIGN)+PHIB)*PI()/180)-(JRC/LN(10))
*(TAN((JRC*LOG(JCS/SIGN)+PHIB)*PI()/180)^2+1)*PI()/180
PHI = ATAN(DTDS)*180/PI()
COH = TAU-SIGN